Stimuli-Responsive Polymer-Based Devices for Surface Plasmon Resonance Spectrometer
Sensing

by

Menglian Wei

A thesis submitted in partial fulfillment of the requirements for the degree of

Doctor of Philosophy

Department of Chemistry
University of Alberta

Abstract

Surface plasmon resonance (SPR) has emerged as a powerful tool in sensing and biosensing for decades due to its label free and real-time data collection characteristics. In the first part of this thesis, a custom-built high performance SPR spectrometer with broad range of scanning angle, high resolution of 0.001° and multi operation mode is described in Chapter 2. The second part of the thesis (Chapters 3-5) focuses on development of a novel SPR sensor substrate that is able to detect small molecules (< 400 Da) in low concentration with high sensitivity. Stimuli-responsive polymers, especially poly(N-isopropylacrylamide) (pNIPAm)-based microgels, were used in the assay development for SPR signal enhancement (Chapters 3-4). In addition, a cost effective method was developed to fabricate hexagonal close packed Au nano arrays by directly painting the Au@pNIPAm hybridized core shell particles on the substrate and plasma etching after deposition; this can potentially be used in SPR sensor substrate and surface-enhanced Raman spectroscopy. Due to the thermoresponsivity of the pNIPAm shell, the interparticle Au nanoarray distance can be dynamically tuned and controlled by varying the painting temperature. In Chapter 6, a temperature-light dual responsive photonic device composed of Au@pNIPAm core-shell microgels is reported and its optical properties were investigated under the stimuli of temperature and light. In addition, the dependence of AuNPs distribution in microgel composites on light responsive performance was compared in terms of optical heterogeneity and responsive kinetics. In Chapter 7, a pNIPAm-brush based optical device with multi-responsiveness was reported, which can potentially be used for sensing and biosensing, drug delivery or other applications that require light manipulation and wavelength filtration.

Preface

This thesis is the original work from Menglian Wei under the supervision of Dr. Serpe at the University of Alberta.

Chapter 7 of this thesis has been published as M. Wei, Y. Gao, M.J. Serpe, "Polymer Brush-based Optical Device with Multiple Responsivities", J. Mater. Chem. B., 2015, 3, 744-747. Yongfeng Gao and I contributed equally to this communication. I was responsible for experiment conduction, data collection and manuscript composition. Yongfeng Gao assisted in experiment design, Figure preparation and results discussion. M.J. Serpe was the supervisory author and was involved with concept formation and manuscript composition.

An active life serves the purpose of giving man the opportunity to realize values in creative work, while a passive life of enjoyment affords him the opportunity to obtain fulfillment in experiencing beauty, art, or nature. But there is also purpose in that life which is almost barren of creation and enjoyment and which admits of but one possibility of high moral behavior: namely, in man's attitude to his existence, an existence restricted by external forces. A creative life and a life of enjoyment are banned to him. But not only creativeness and enjoyment are meaningful. If there is a meaning in life at all, then there must be a meaning in suffering. Suffering is an ineradicable part of life, even as fate and death. Without suffering and death human life cannot be complete.

The way in which a man accepts his fate and all the suffering it entails, the way in which he takes up his cross, gives him ample opportunity–even under the most difficult circumstances– to add a deeper meaning to his life. It may remain brave, dignified and unselfish. Or in the bitter fight for self-preservation he may forget his human dignity and become no more than an animal. Here lies the chance for a man either to make use of or to forgo the opportunities of attaining the moral values that a difficult situation may afford him. And this decides whether he is worthy of his suffering or not.

<div align="right">

Man's Search for Meaning

Frankl, Viktor E.

</div>

Acknowledgments

I would like to give the thanks to our Almighty God for everything.

I would like to express my gratitude to my supervisor Dr. Serpe for offering me the opportunity to come to Canada and allowing me to work in his lab. Under his patient guidance and enthusiastic inspiration, I have gained quite a lot of knowledge in the field of polymer science and optical technologies and have grown to be a professional researcher during the past five years. The outcome of this research would never be possible without his support.

I would like to express my appreciation to my supervisory committee members Dr. McCreery, Dr. Le, Dr. Yu, Dr. Zeng and Dr. McDermott for their valuable discussions, suggestions and comments. Thank you all for your guidance during the past five years.

I would like to thank the staff in the Machine shop and Electronic shop of the Department of Chemistry, who did a great job in helping me in the design and fabrication of instrument parts. I would like to thank my past and current labmates for their help and company, especially Xue, Wenwen, Yongfeng and Andrews. Without you guys, the color of the lab would only be white and black. I would like to give my deepest gratitude to Dr. Anna Jordan who helped me revising and editing this thesis.

Finally, I would like to thank my parents, grandparents and brothers who provided me with unconditional love and emotional support. I will never be who I am and walk this far without you.

Table of Contents

List of Table

List of Figures

Chapter 1

Introduction to Surface Plasmon Resonance

In this Chapter, surface plasmon resonance (SPR) is introduced. The first section focuses on the history of SPR and an overview of available commercial instrumentation. The second section focuses on propagating-based SPR techniques with different excitation setups. The physical mechanisms involved will be included in detail. The third section focuses on localized SPR (LSPR) that exists on metallic nanostructures, whose theory and synthesis will be covered. This Chapter will be the foundation for better understanding of the chapters which follow.

1.1 Background and History of SPR

Surface plasmons (SPs) are the collective oscillation of electrons along the interface of a free electron metal (e.g. gold, silver, aluminum and copper) and a dielectric medium (e.g. gas, liquid and solid).[1] The first observation of this physical phenomenon was recognized originally more than 100 years ago by R. W. Wood, when he observed diffraction anomalies as polychromatic light illuminations on metallic diffraction gratings.[2] In 1941, Fano[3] was the first to give an explanation of these anomalies that related to the electromagnetic waves excited on gratings. Eventually, the theory of SPR was fully developed and proved by Ritchie,[1] Stern and Ferrell[4] and Kanazawa[5] in the late 1950s. They explained the associated energy loss as the electron beam passing through thin metallic foils in contact with a dielectric medium. Until the 1960s, the optical excitation of SPR was demonstrated by Otto[6] and Kretschmann and Raether[7]

on the basis of attenuated total reflection (ATR) in a prism, which showed the versatility and great potential of this optical technique. The Kretschmann configuration, especially, is used in most SPR instrumentation today. The application of the SPR technique in biomolecular interaction studies was first demonstrated by Lundstrom in 1983 as an alternative approach to label-free, real time detection of biomolecules.[8] The first commercial SPR product (Biacore) was launched by Pharmacia Biosensor AB in 1990. Biacore became the most advanced, sensitive, accurate, reliable and reproducible direct biosensor technique.[9] These features, including versatility, label-free and real-time monitoring of SPR techniques, make it of widespread use in physical, chemical and biological areas.[10]

1.2 Propagating SPR

Plasmons are a coherent fluctuation of conducting electrons in a metal. When the electrons are displaced, an attractive force between the positive charge and the electrons will pull the electrons back to their original position.[11] Such Coulomb-like interactions are the driving force of electron oscillation when they are excited. Unlike in bulk materials where electrons oscillate through the metal volume, SPs are confined to the interface of a metal and a dielectric medium with characteristic 2D waves. An illustration of surface plasmons is shown in Figure 1-1.
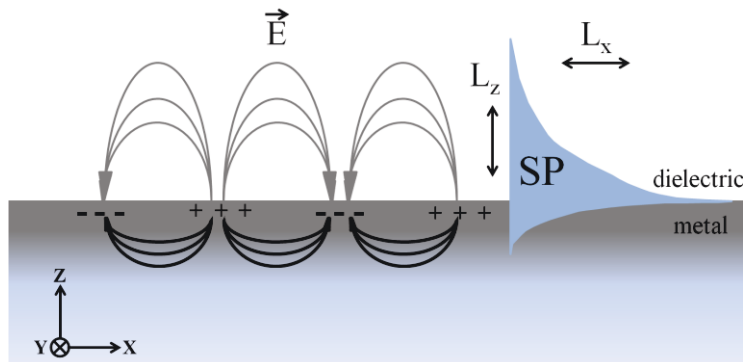
Figure 1-1. SPs propagation on the metal/dielectric medium interface (along X axis at Z=0) and penetration through both sides with exponential decay (maximum field intensity at Z=0). The local charge produces an evanescent field in the X and Z directions with an electric field strength of $\vec{E}$. The L_x is the generated SPs evanescent wave propagation length along the metal/dielectric medium interface. The L_z is the generated SPs evanescent wave penetration depth in metal/dielectric medium.

1.2.1 Optical Properties of Metals

The frequency of collective free electron oscillation at the metal/dielectric interface, which is also called plasmon frequency, can be defined by Eq. (1),[11]

$$\omega_p = \sqrt{\frac{Ne^2}{\varepsilon_0 m}} \tag{1}$$

where N is the free electron density, e is the electron charge, m is the electron mass and ε_0 is the permittivity of the free space. In the Drude model, which treats the electrons as a gas of free particles, the dielectric constant of a metal can be described as a function of the applied electric field with angular frequency of ω, as defined in Eq. (2),[12]

$$\epsilon(\omega) = 1 - \frac{\omega_p^2}{\omega^2 + i\omega\gamma} \tag{2}$$

where ω_p is the plasmon frequency and γ is the collision frequency with an amplitude of $\sim 10^{14}$ Hz at room temperature. The electron–nuclei collision dampens the electron oscillation in the presence of an external electromagnetic field. Drude's model is adequate enough to describe many aspects of optical properties of metals even with the electrons/electrons and electrons/positive-core interaction omission. The dielectric constant of a metal can also be defined as a complex number by Eq. (3),

$$\epsilon\,(\omega) = \,\epsilon_1(\omega) + i\epsilon_2(\omega) \tag{3}$$

where $\epsilon_1(\omega)$ is the real part and $\epsilon_2(\omega)$ is the imaginary part. Both of these terms are associated with the refractive index n and the extinction coefficient K, given by the following expressions:

$$\epsilon_1 = \, n^2 - K^2 \tag{4}$$

$$\epsilon_2 = \, 2nK \tag{5}$$

By measuring the reflection and transmission of a vacuum-evaporated thin film at room temperature, Johnson and Christy have investigated the optical properties of noble metals (gold, silver and copper) in the spectral range of 0.5–6.5 eV.[13] The results were shown in Figure 1-2. Such experimental measurements are useful in distinguishing the contribution from free electrons and interband transitions.

1.2.2 SPR on a Smooth Surface

As shown in Figure 1-1, the SPs are excited on the interface of two semi-infinite media, which represent a dielectric material (Z>0) and a metal (Z<0). The dielectric constant of these materials is given by,

$$\epsilon_d\,(\omega) = \epsilon_{d1}(\omega) + i\epsilon_{d2}(\omega) = \epsilon_{d1}(\omega) \tag{6}$$

$$\epsilon_m\,(\omega) = \epsilon_{m1}(\omega) + i\epsilon_{m2}(\omega) \tag{7}$$
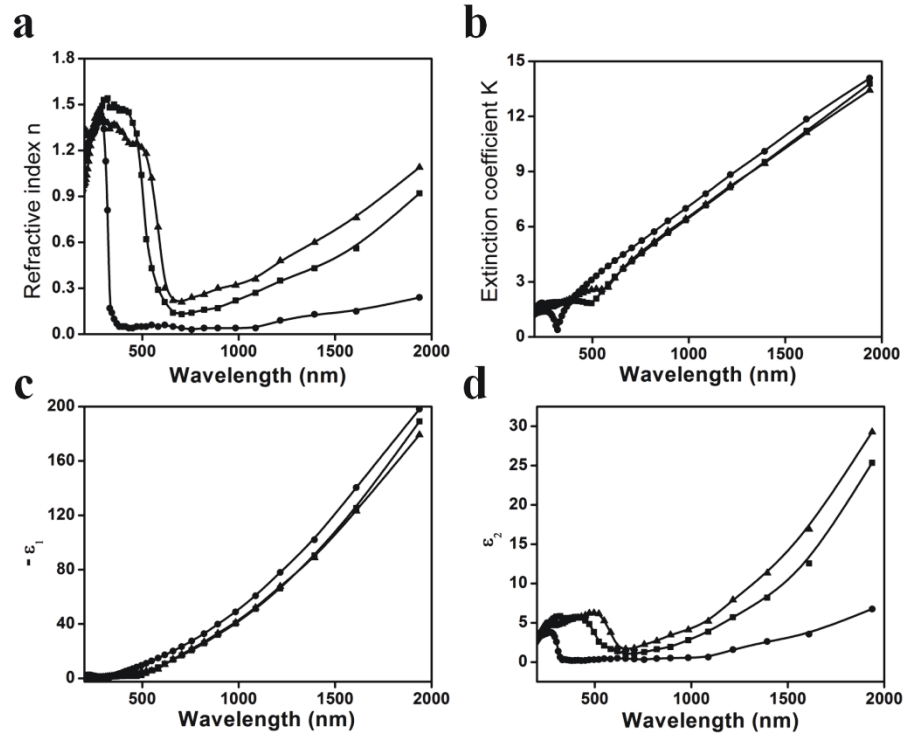
Figure 1-2. Optical properties of noble metals gold(■), silver(●), copper(▲) in the spectral range of 0.5 to 6.5 eV. a) Refractive index n; b) extinction coefficient K; c) negative real part of permittivity $-\epsilon_1$; d) imaginary part of permittivity ϵ_2. Reprinted with permission from Ref. 13. Copyright 1972, Physical Review B.

where $\epsilon_d(\omega)$ is for a dielectric material and $\epsilon_m(\omega)$ is for a metal. When an incident electromagnetic wave is shone through a dielectric onto a metal, the SPs are generated in transverse magnetic (TM) modes (also known as p-polarized electromagnetic waves, with the electric field lying in the XZ plane) and propagate in the XZ plane. By solving Maxwell's equations with proper boundary conditions, the requirements of excitation of SPs at the planar metal–dielectric interface can be obtained. The derivation details can be found elsewhere.[11, 14] The conclusion is that there is no solution for a transverse electric (TE) mode electromagnetic

wave as it only has a component along the Y axis. In addition, the propagation of SPs along the X axis can exist only when the dielectric constant of these two media satisfy both Eq. (8) and (9),

$$\frac{k_{zd}}{\epsilon_d} + \frac{k_{zm}}{\epsilon_m} = 0 \tag{8}$$

$$k_{xd} = k_{xm} = k_{sp} = \frac{\omega}{c}\sqrt{\frac{\epsilon_d \epsilon_m}{\epsilon_d + \epsilon_m}} \tag{9}$$

where k_{zd} is the component of the wavevector in the Z direction in the dielectric medium, k_{zm} is the component of the wavevector in the Z direction in the metal, k_{xd} is the component of the wavevector in the X direction in the dielectric medium, k_{xm} is the component of the wavevector in the X direction in the metal, ω is the frequency of the applied electromagnetic wave, c is the speed of light in vacuum and ϵ_d and ϵ_m are the dielectric constant of the dielectric medium and metal, respectively. There is a solution for Eq. (8) and (9) only when the dielectric constants of these two materials have opposite signs with $\epsilon_m < 0$, $\epsilon_d > 0$ and $|\epsilon_m| > \epsilon_d$, which also yields:

$$k_{zd} = \frac{\omega}{c}\sqrt{\frac{\epsilon_d{}^2}{\epsilon_d + \epsilon_m}} \tag{10}$$

$$k_{zm} = \frac{\omega}{c}\sqrt{\frac{\epsilon_m{}^2}{\epsilon_d + \epsilon_m}} \tag{11}$$

1.2.3 Penetration Depth L_z

The evanescent characteristics of SPs can be seen from the expression for the electric field in Eq. (12),[15]

$$E_j(x, z, t) = (E_{x,j}, 0, E_{z,j})e^{ik_{z,j}z}e^{i(k_{sp}x - \omega t)} \tag{12}$$

where $j = m$ for the electric field intensity E_m in the metal and $j = d$ for the electric field intensity E_d in the dielectric medium. It can be seen that the electric field decreases exponentially in both the X and Z directions. However, as the wavevector in the Z direction (k_{zd}

and k_{zm}) is still imaginary, this means that it is non-propagative and evanescent in the Z direction. The penetration depth or the skin depth, the distance where the electric field decreases to $1/e$, can be defined by Eq. (13),

$$L_{zj} = \frac{c}{\omega} \sqrt{\frac{\epsilon_d + \epsilon_m}{\epsilon_j^2}} \qquad (13)$$

where $j = m$ for the penetration depth L_{zm} in the metal and $j = d$ for the penetration depth L_{zd} in the dielectric medium. It is apparent from equation (13) that the penetration depth strongly depends on the frequency ω. For example, when exciting surface plasmons on a gold/water interface with 630 nm wavelength light, the penetration depth in Au was around 29 nm; while it is ~162 nm in water.[10b] As the excitation wavelength changed to 850 nm, the penetration depth became 25 nm and 400 nm in gold and water, respectively.[10b] The wavelength dependence of the SPs penetration depth at the interface of a Au/dielectric medium (n =1.32)[14a] is shown in Figure 1-3. The penetration depth in the dielectric medium increases as the excitation wavelength increased, while it decreases in the metal. The expression of the penetration depth also explains why the SPs are only sensitive to refractive index changes in the vicinity of the metal/dielectric medium interface (normally in the hundred nm range in the dielectric material). For biomolecules with a size a_{bio}, which is normally smaller than L_{zd}, this means that they can always "feel" the SPs' field once the biomolecule is captured on the metal surface. The effective refractive index n_{eff} under the evanescent field can be defined by averaging a Z-dependent dielectric refractive index $n(z)$ by a weighting factor $W(z) = e^{-z/L_z}$, as shown in Eq. (14):[16]

$$n_{eff} = \frac{\int_0^{+\infty} n(z)W(z)dz}{\int_0^{+\infty} W(z)dz} = \frac{1}{L_z}\int_0^{+\infty} n(z)e^{-z/L_z}dz \qquad (14)$$

Such an expression can be simplified to yield Eq. (15) when a single biolayer with a refractive index n_{bio} adsorbs on the interface,

$$n_{eff} = n_d + (n_{bio} - n_d)(1 - e^{-a_{bio}/L_z})$$ (15)

where n_{bio} and n_d are the refractive index of the biomolecule and the dielectric medium, respectively, a_{bio} is the size of the biomolecule and L_z is the penetration depth in the dielectric medium.
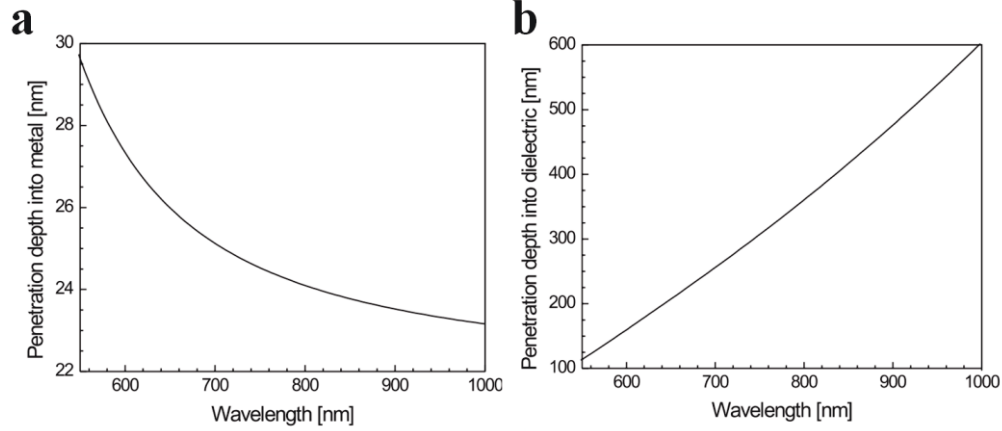
Figure 1-3. The penetration depth of surface plasmon resonance at the interface of Au and the dielectric medium with a refractive index of 1.32 in the metal (a) and in the dielectric medium (b).[14a] Reprinted with permission from Ref. 14a. Copyright 2006, Springer.

1.2.4 Propagation Length L_x along the Semi-infinite Interface

In the X axis, the wavevector (k_{sp}) is complex, with a positive value for both the real $(k_{sp}{}')$ and the imaginary $(k_{sp}{}'')$ parts, given by the following expressions:

$$k_{sp}{}' = \frac{\omega}{c}\sqrt{\frac{\epsilon_{m1}\epsilon_d}{\epsilon_{m1}+\epsilon_d}}$$ (16)

$$k_{sp}{}'' = \frac{\omega}{c}\left(\frac{\epsilon_{m1}\epsilon_d}{\epsilon_{m1}+\epsilon_d}\right)^{3/2}\frac{\epsilon_{m2}}{2\epsilon_{m1}{}^2}$$ (17)

They indicate how the SPs are able to propagate along the X axis and exponentially decay with a propagation length of L_x, which can be defined by Eq. (18):[15]

$$L_x = \frac{1}{2k_{sp}''} = \frac{c}{\omega} \left(\frac{\epsilon_{m1}+\epsilon_d}{\epsilon_{m1}\epsilon_d}\right)^{2/3} \frac{\epsilon_{m1}^2}{\epsilon_{m2}} \tag{18}$$

Note that the distance that surface plasmons propagate along the interface of a given metal/dielectric depends on the frequency ω. Typically, the propagation length of SPs at the gold/water interface can be up to 3.8 µm under the excitation at 632 nm.[17] The spectral dependence of the propagation length of the SPs' supported by different metals (gold, silver and aluminum) is shown in Figure 1-4. From the Figure, it can be predicted that the SPs propagates longer at the interface of semi-infinite media as the wavelength increases.
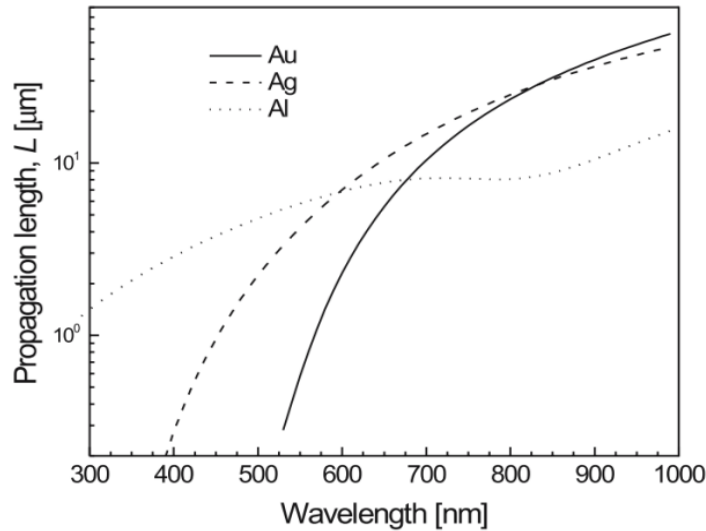
Figure 1-4. The propagation length of SPs at the interface of the metal and the dielectric medium (n =1.32) as a function of wavelength.[14a] Reprinted with permission from Ref. 14a. Copyright 2006, Springer.

1.2.5 Optical Excitation of SPs

To excite the SPs at the metal/dielectric medium interface, an external energy source is needed, which can be fast electrons or light. Electronic excitation of SPs can only be achieved under vacuum conditions,[15] which will not be discussed here. In the case of light illumination,

the SPs can be excited only when the horizontal component (X axis) of the wavevector of the photon ($k_{ph,x}$) matches the real part of the k_{sp}. The wavevector of the component in the X direction of a photon traveling in a dielectric medium can be defined by Eq. (19),

$$k_{ph,x} = \frac{\omega}{c}\sqrt{\epsilon_d}\sin\theta \tag{19}$$

where θ is the incident angle, ϵ_d is the dielectric constant of the dielectric medium, ω is the angular frequency of the photon and c is the speed of light in vacuum. As described in the previous section, the real part of k_{sp} can be defined by Eq. (20),

$$k_{sp}{'} = \frac{\omega}{c}\sqrt{\frac{\epsilon_{m1}\epsilon_d}{\epsilon_{m1}+\epsilon_d}} \tag{20}$$

where ϵ_{m1} is the real part of the dielectric constant of the metal, ϵ_d is the dielectric constant of the dielectric medium, ω is the angular frequency of the photon and c is the speed of light in vacuum. Obviously, it is impossible to satisfy the condition of the SPs excitation by directly shining light onto a smooth metal surface because $k_{ph,x} < k_{sp}{'}$ even at $\theta = 90°$. As a consequence, the wavevector of the incident light should be increased to match the real part of the k_{sp} in order to excite the SPs at the metal/dielectric medium. Generally, two methods can be applied to gain additional wavevector to transform the photon to the SPs. The first one utilizes the diffraction gratings,[18] the second one employs the attenuated total reflectance coupler.[19] These two mechanisms will be discussed below in detail.

1.2.5.1 Grating Coupler

As illustrated in Figure 1-5a, when a beam of light impinges on the interface of a dielectric medium and a metal grating, the wavevector in the horizontal component will be enhanced by the diffraction so that the SPs are excited at the interface. The additional

wavevector gained by shining light on a diffraction grating coupler with a periodicity of Λ can be defined by Eq. (21),[10b]

$$\Delta k_x = m\frac{2\pi}{\Lambda} \tag{21}$$

where m is the diffraction order (integer) and Λ is the grating constant. The total wavevector that is able to generate SPs becomes:

$$k_{ph,x}' = k_{ph,x} + \Delta k_x = \frac{\omega}{c}\sqrt{\epsilon_d}\sin\theta + m\frac{2\pi}{\Lambda} = \frac{\omega}{c}\sqrt{\frac{\epsilon_{m1}\epsilon_d}{\epsilon_{m1}+\epsilon_d}} = k_{sp}' \tag{22}$$

The diffraction occurs only when the illumination length is larger than the periodicity Λ. By tuning the parameters of the incident angle θ, the grating constant Λ and the incident light frequency ω, Eq. (22) can be satisfied and results in the excitation of SPs.
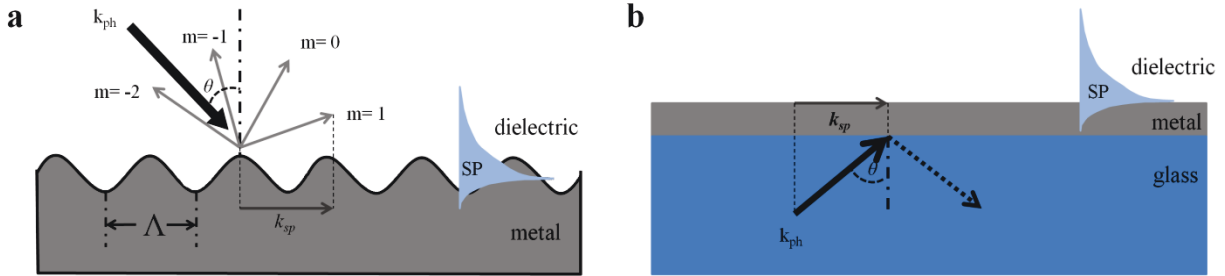
Figure 1-5. Optical excitation of SPs based on (a) grating coupling and (b) ATR coupling.

1.2.5.2 ATR Coupler

The second method of increasing the excitation wavevector is ATR-coupling, shown in Figure 1-5b, which was used in the Kretschmann configuration. Separately, Otto also discovered the ATR-coupling excitation of SPs, by which a thin layer (subwavelength) of air was used to separate the metal and glass and worked as an evanescent tunnel barrier.[6a] Since the Kretschmann configuration is more common in modern instrumentation and also is applied in

our instrument building, this setup will be the focus of our discussion. When light shines through a glass (dielectric constant $\epsilon_g > \epsilon_d$) and is reflected at the glass/metal interface , the wavevector at this interface can be defined by Eq. (23),[15]

$$k_{ph,x} = \frac{\omega}{c}\sqrt{\epsilon_g}\sin\theta \tag{23}$$

where ϵ_g is the dielectric constant of the glass and θ is the incident angle. Under these conditions, it is possible to meet the requirement of $k_{ph,x} = k_{sp}{'}$ by choosing the proper glass (ϵ_g), incident angle (θ) and frequency (ω) to excite SPs since $\epsilon_g > \epsilon_d$. As a result, Eq. (24) is obtained:

$$\frac{\omega}{c}\sqrt{\epsilon_g}\sin\theta = \frac{\omega}{c}\sqrt{\frac{\epsilon_{m1}\epsilon_d}{\epsilon_{m1}+\epsilon_d}} \tag{24}$$

Since the metal in this case is no longer treated as a semi-infinite material, the incident wave is able to penetrate through this thin metal layer ($d_m \ll L_z$) and reach the interface of the metal/dielectric to generate SPs, which finally decay exponentially in the dielectric medium. For a metal layer thickness d_m greater than L_z, the electric field of the incident wave will decrease to almost zero when reaching the metal/dielectric interface; this will not have a coupling effect and will not be able to generate SPs at the metal/dielectric interface. Therefore, the thickness of the metal also plays an important role in the excitation of SPs. Generally, 50 nm Au or 47 nm Ag were used in the experimental setup to achieve the best sensitivity.[9] From Eq. (24), one is able to derive the angle (θ_{RA}) at which SPs were excited at a given glass/metal/dielectric medium,

$$\theta_{RA} = \arcsin\sqrt{\frac{\epsilon_{m1}\epsilon_d}{\epsilon_g(\epsilon_{m1}+\epsilon_d)}} \tag{25}$$

where ϵ_{m1} is the real part of the frequency-dependent dielectric constant of the metal and ϵ_d and ϵ_g are the frequency-dependent dielectric constant of the dielectric media and the glass,

respectively. This angle is known as the resonance angle (RA). The critical angle (θ_C) can be expressed as:

$$\theta_C = \arcsin \sqrt{\frac{\epsilon_d}{\epsilon_g}} \tag{26}$$

Since $\epsilon_{m1} < 0$, $\epsilon_d > 0$ and $\epsilon_g > 0$, RA will always larger than θ_C at the glass/dielectric interface. Therefore, this setup was called an ATR-coupling as the SPs can only be excited above the critical angle. It is obvious that one is unable to excite the SPs by directly shining light from the bottom of the metal coated glass as the internal incident angle (θ_{int}) will always be smaller than critical angle ($\theta_{int} \leq \arcsin \sqrt{\frac{\epsilon_{air}}{\epsilon_g}} < \arcsin \sqrt{\frac{\epsilon_d}{\epsilon_g}}$), as shown in Figure 1-6.
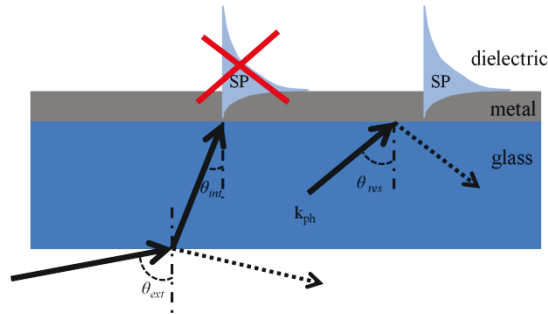
Figure 1-6. A schematic illustration of the disability of exciting the SPs by directly shining light from the bottom of a metal coated glass substrate. In this case, the angle of incidence will always be smaller than the critical angle even when the excitation angle (θ_{ext}) is at a gazing degree.

Different approaches can be deployed to solve these issues.[20] The first is applying a prism-based ATR setup (Kretschmann configuration), as shown in Figure 1-7a. A hemicylindrical prism is coupled to the back of a metal-coated glass substrate with refractive index matching oil, or a thin metal film is directly deposited on the disposable prism. In this case, θ_{int} is equal to θ_{ext} with a broad scanning angle that is able to excite the SPs at the θ_{RA}. For a

particular refractive index of the surrounding material (dielectric medium in contact with the metal) and specific wavelength of incident light traveling through the prism, there is only one resonance angle, θ_{RA}, able to meet the requirement of wavevector matching shown in Eq. (25). By scanning the angle at which the light impinges the prism, one is able to tune the horizontal component of the photon wavevector so that it matches the real part of the k_{sp} to generate SPs at the metal/dielectric interface. The parameters of incident light, such as the intensity, phase, spectral distribution and polarization, will change significantly once the light is coupled to the metal and the excited SPs. With a different detector, multiple operation modes were available in prism-based SPR instrumentation. For example, if the light intensity is recorded by a photodiode, the reflected intensity can be plotted as a function of the scanning angle (θ_{int}). Due to the light absorption by SPs, one will observe diminished reflected light intensity. The angle at which the minimum reflected intensity is observed is called the resonance angle. As demonstrated in Eq. (25), such an angle is very sensitive to the refractive index change ($\sqrt{\epsilon_d}$) at the vicinity of the metal surface. A typical SPR spectrum is shown in Figure 1-8a. As can be seen, a significant resonance angle shift can be observed when the dielectric medium changes from air ($\sqrt{\epsilon_{air}} \approx 1$) to water ($\sqrt{\epsilon_{water}} \approx 1.33$). Alternatively, instead of an angular based interrogation, the resonance condition can be fulfilled by shining a white light with multi-wavelengths at a fixed angle so that one of the specific wavelengths excites the SPs. A traditional wavelength module based SPR spectrum is shown in Figure 1-8b. As can be seen, the resonance wavelength revealed a red shift as the refractive index increased due to more protein-binding on the sensor surface. For a prism based SPR sensor, the documented refractive index resolution is around 10^{-6}–10^{-8} refractive index units (RIU).[21]

Generally, in the Kretschmann configuration, bulk optical parts were involved in the instrumentation such as the light source, detector and prism as well as in the liquid handling system for sensing. Other options to excite SPs with a compact setup and a remote detection capability can be fulfilled by an optical fiber based SPR platform.[22] The structure of an optical fiber based SPR sensor is shown in Figure 1-7b; it is composed of a core in the center and is surrounded by a cladding layer with a refractive index gradient. By removing a chunk of cladding, the fiber core was exposed for a further thin metal film coating. The sensor area was composed of a thin metal film at the core/cladding interface with an overlayer potentially exposed to the sample of interest. The principle of the excitation of SPs is similar to that of a prism based Kretschmann setup. As shown in Figure 1-7b, the light propagates in the fiber core with total internal reflection due to the refractive index difference between the core and the cladding (lower refractive index). By tuning the angle of light emitted to the core layer, the evanescent field was generated with a wavevector matching condition that satisfied the one coupled to the SPs; this finally resulted in a reflectance change. In addition, the evanescent field can penetrate the cladding layer at around 100 nm.[23] The optical fiber based SPR sensor normally has a lower minimal detectable refractive index resolution than the prism based one, in the range of 10^{-4}–10^{-6} RIU.[24] Other disadvantages of optical fiber based SPR sensors include the multimode combination in the operation with uncontrolled fields so that the SPR spectra were broad and ill-defined, with an overall under performance.[25] The non-standard optical fiber modification normally faced the challenge of fragility, suffering from a high cost compared to unmodified standard fibers.[26]
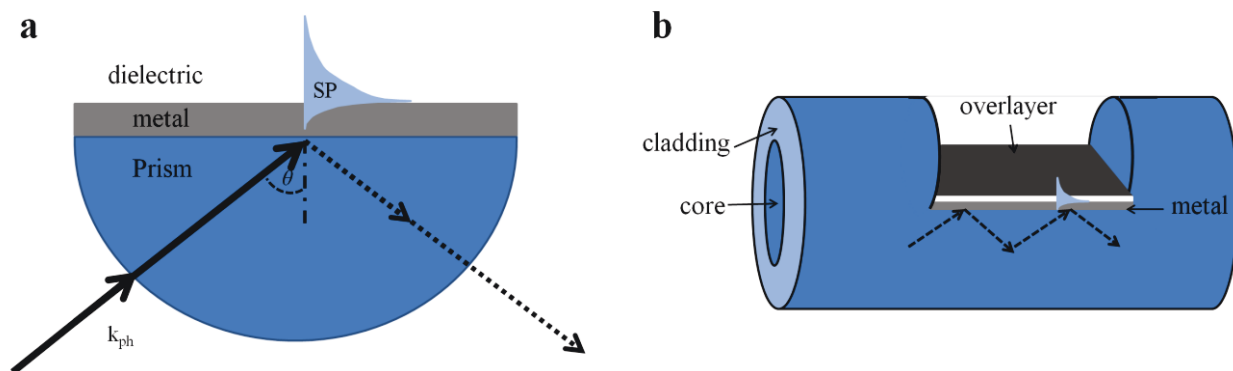
Figure 1-7. a) A prism based ATR setup for the excitation of the SPs. The excitation angle is equal to the internal incident angle, which can range from 0 to 90°. b) An optical fiber based ATR setup for the excitation of the SPs.
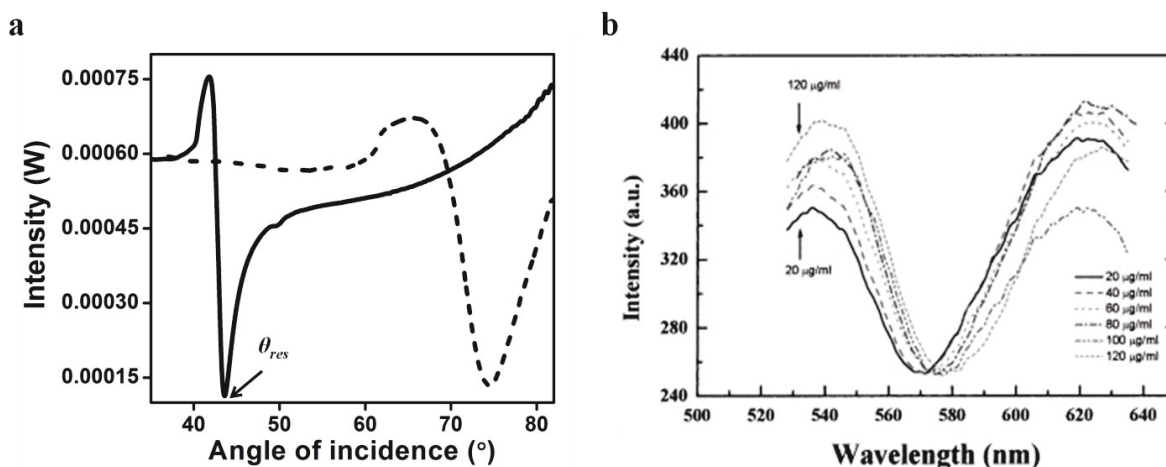
Figure 1-8. (a) A typical angular module SPR spectrum of a 50 nm Au coated glass substrate coupled to a BK7 hemicylindrical prism in air (solid) and water (dash) with a 632.8 nm HeNe laser excitation; (b) A typical wavelength module SPR spectrum of a 42 nm Au coated glass substrate coupled to a BK7 triangular prism in different concentrations of tissue transglutaminase with a quartz tungsten halogen lamp as a multi-wavelength light source.[27] (b) Reprinted with permission from Ref. 27. Copyright 2003, Elsevier.

1.2.6 SPR for Sensing and Biosensing

A sensor/biosensor generally is composed of four elements: the target (molecule of interest), the probe (specifically interacts with the target), the transducer (converts the target/probe interaction into a measurable quantity) and the signal (detected by the instrument and finally displayed as readable information).[28] The SPR as a sensing and biosensing platform was able to modify probe molecules on the Au sensor surface and detect the refractive index change near the sensor surface upon the target approaching, which finally yielded a resonance angle shift or reflected light intensity change. The characteristics of SPR, including real-time detection, label-free, high detection sensitivity and a wide dynamic range, make them perfect optical tools in sensing and biosensing applications.[29] The following section will cover the challenges of a SPR platform in sensing and biosensing that this thesis aims to address.

1.2.6.1 Challenges of SPR in Sensing and Biosensing

As shown in the theoretical description in section 1.2.3, the penetration depth of SPs in the dielectric medium (normally an aqueous solution) is in the range of a hundred nanometers, which means that the SPs will only be sensitive to changes in the vicinity of the sensor surface (from the metal/dielectric medium interface extended to hundreds of nanometers in the dielectric). Much research has been conducted into examining relatively large molecules, like proteins and their interaction with other biomolecules-proteins/aptamer/nucleotides[29b] due to their comparable size with the evanescent field. However, the dimensions of some other biomolecules of interest normally fall in the range of microns such as microbes, pathogens, viruses and cells, which is beyond the limit of the sensing field. Therefore, it is extremely difficult to detect these biomolecules of interest via a SPR platform. Another extreme case is the detection of small molecules with molecular weights below 400 Da, like organic molecules and carbohydrates. Generally, the presence of these molecules also has clinical significance that

indicates specific stages of illness or disease. However, the cumulative refractive index change from the small molecules in low concentration is normally too small to result in a detectable resonance angle shift or a reflected light intensity change. The two aspects mentioned above are the main challenges researchers were facing in SPR sensing and biosensing. The detection of small molecules in low concentrations via a SPR platform is the aim that thesis wants to address.

1.2.6.2 Approaches of SPR Signal Amplification

Some great reviews[30] have been published describing strategies that can be used to enhance SPR signals. In principle, these approaches involve additional mass introduction to the metal/aqueous interface to increase the total refractive index change that finally yields an observable signal change. The additional mass can come from biomolecules like the sandwich based enzyme-linked immunosorbent assay (ELISA) or from nanomaterials (they exhibit a great contrast in refractive index) such as a carbon nanotube,[31] Au nanoparticles,[32] latex particles,[33] etc. One of the first SPR signal amplifications reported by the Keating group was that when the oilgonucleotides were modified with colloidal Au nanoparticles (AuNPs), a 10-fold angular shift took place, which corresponded to a ~1000-fold sensitivity improvement.[34] The illustration of this assay is shown in Figure 1-9. A probe of short oilgonucleotide S1 was immobilized on the Au sensor surface by thiol chemistry. Upon binding a complimentary oilgonucleotide S2 with more base pair than S1, the resonance angle showed a ~0.1° shift (Figure 1-9b). The oilgonucleotide S2 here also played a role as an anchor for a secondary amplification tag attachment. Subsequently, another oilgonucleotide S3 (complimentary to the extended based pair of S2) modified with AuNPs was introduced to the system and yielded a ~2° angular shift of SPR spectra. The authors claimed that the SPR signal amplification is due to several reasons: 1) absolute mass loading increase by AuNPs as the secondary binding events happened; 2) great

refractive index contrast of AuNPs to biomolecules like DNA; 3) plasmon coupling between AuNPs and the planner Au sensor surface.
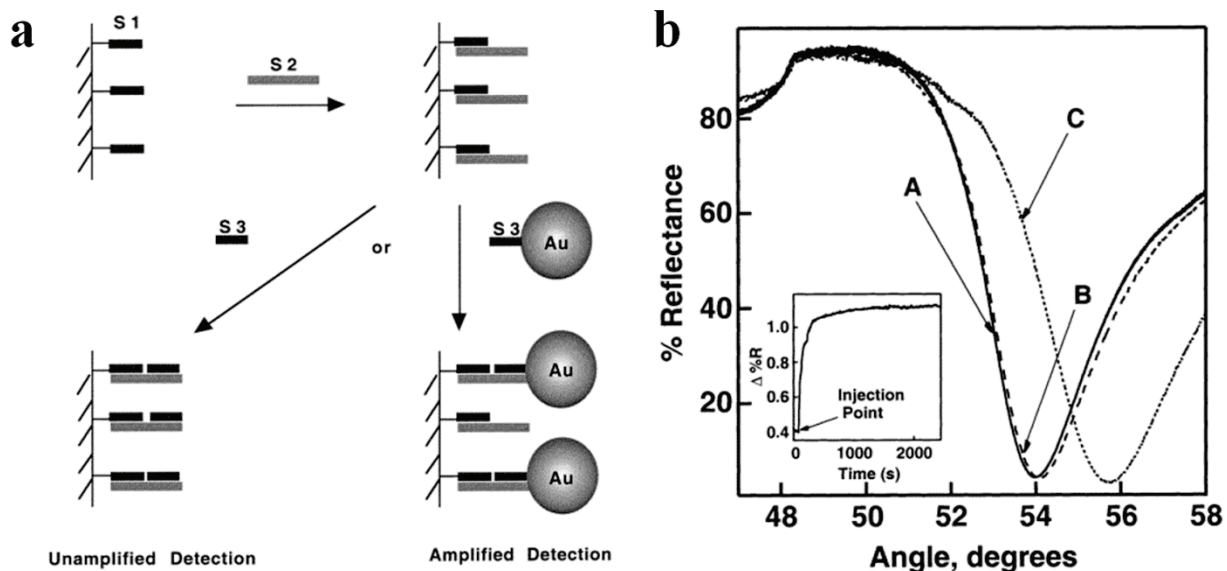
Figure 1-9. a) A schematic illustration of oilgonucleotide detection based on colloidal Au nanoparticle amplification; b) a SPR spectrum of (A) a Au surface modified with the S1 oilgonucleotides, (B) upon binding of the S2 to the S1 oilgonucleotide modified Au sensor surface and (C) after binding of Au nanoparticles attached S3 oilgonucleotides to the S2/S1 oilgonucleotide modified Au sensor surface.[34] Reprinted with permission from Ref. 34. Copyright 2000, American Chemical Society.

Other examples of molecules of interest are antibodies, antigens, metabolites, etc. In these cases, the surface functionalization can use Au-S coupling or carboxylic group/amine chemistry for sensor surface and amplification tag modifications due to the richness of amines in biomolecules. Moreover, the amplification tag can use materials other than AuNPs such as liposome particles, silver nanoparticles, quantum dots and latex particles. To sum up, such a sandwich based amplification assay is so versatile that it can be applied in the detection of

different analytes. However, there are some disadvantages, such as the expensive cost of additional precious bio-reagents, the complexity of surface/tag modification and multiple injection/wash steps.

In this thesis, the principle strategies for amplifying SPR signals is the utilization of smart polymers that were able to convert the biomolecule interactions into a polymer conformation change, which results in a higher refractive index change compared to sole biomolecule binding. The smart polymers are macromolecules that are able to change their chemical or physical properties under exposure to external stimuli, such as temperature, pH, ionic strength and analyte concentration.[35] One of the most well studied thermoresponsive polymers is poly(N-isopropylacrylamide) (pNIPAm), which exhibits a linear to globular conformation change at temperatures above the low critical solution temperature (LCST) ~32 °C.[36] Like the linear chain, the crosslinked pNIPAm (such as a microgel/hydrogel classified in terms of size) network exhibits a volume phase transition at the critical temperature (~32 °C as well), which remains swollen below this temperature and shrinks above this temperature. A smart polymer can be designed in such a way that it responds to multiple stimuli in addition to temperature by copolymerizing with other monomers; examples can be found in the literature.[37] In addition, there are numerous good reviews[35, 38] a reader can refer to concerning stimuli-responsive polymers with respect to their properties and applications, which will not discussed in detailed here. Furthermore, the introduction about the smart polymer used is included in the individual Chapters as well.

1.2.6.3 Kinetics Measurement in Real-time Mode[39]

In addition to merely obtaining the quantitative information of an analyte in a sample with a SPR spectrum, one also is able to derive the binding affinity by examining the SPR sensorgram. A typical SPR sensorgram for antibody–antigen interaction can be seen in Figure 1-10. As the injection of analyte flows through the sensor surface, the response signal increases, indicating the association phase of target binding to the probe (immobilized on the sensor surface). The response reaches a plateau once all the binding sites are occupied. Subsequently, introducing a buffer will result in target/probe complex dissociation and a concomitant response decrease. Fitting the sensorgram data to a binding model (e.g. Langmuir Isotherm) allows for the prediction of the association (k_a) and dissociation (k_d) rate constant and, finally, a determination of the binding affinity. To measure the kinetics, sequential injections of a sample with a concentration gradient are required to flow through the same SPR sensor chip. This means that surface regeneration is needed to remove the entire binding target between each injection. Ideally, a successful surface regeneration can be confirmed by observing from the SPR sensorgram that the signal has dropped back to the original baseline. Regeneration can be performed by injecting a complex solution with a combination of surfactants, salts, and acids or bases. To avoid denaturing or damaging the SPR sensor chip, the regeneration process should be carried out very carefully.

The Langmuir Isotherm model describes the 1:1 target/probe interactions with the assumption that all the binding sites are equivalent and there is no interaction between targets of adjacent binding sites.[40] Pseudo-first-order kinetic was applied to association and dissociation rate constant calculations without considering the limitation of mass transport,

$$A + B \underset{k_d}{\overset{k_a}{\rightleftharpoons}} AB$$
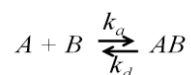
where A represents the immobilized probe molecules on the SPR sensor surface and B represents the target in the analyte, k_a (mol^{-1}s^{-1}) and k_d (s^{-1}) represent the association and dissociation rate constant for the formation and decomposition of complex AB, respectively. In the associated phase,

$$\frac{d[AB]}{dt} = k_a[A]_t[B]_t - k_d[AB]_t \tag{27}$$

where $[A]_t = constant$ and $[B]_t = [B]_{max} - [AB]_t$. The SPR signal (RU) is proportional to the amount of bound complex on the sensor chip. Therefore, the formation of AB complex can further be expressed by Eq. (28),

$$\frac{dR_t}{dt} = k_a[A](R_{max} - R_t) - k_d R_t \tag{28}$$

where R_t is the SPR signal at time t and R_{max} is the maximum SPR signal after all the binding sites are occupied. Upon integration,

$$R_t = \frac{R_{max}[A]}{K_D + [A]}(1 - e^{-(k_a[A]+k_d)t}) \tag{29}$$

where K_D is the binding affinity, given by the following expression:

$$K_D = \frac{k_d}{k_a} \tag{30}$$

and $(1 - e^{-(k_a[A]+k_d)t})$ defines the amount of time needed to reach equilibrium. At the equilibrium phase Eq. (29) becomes:

$$R_t = R_{eq} = \frac{R_{max}[A]}{K_D + [A]} \tag{31}$$

In the dissociated phase, the solution changes to a buffer with the *AB* complex dissociating with time. In this case, the concentration of the target in the solution becomes zero ($[B]_t = 0$). Therefore,

$$\frac{d[AB]}{dt} = -k_a[AB]_t \tag{32}$$

and

$$\frac{dR_t}{dt} = -k_d R_t \tag{33}$$

$$R_t = R_0 e^{-k_d t} \tag{34}$$

where R_0 is the SPR signal at the end of association. This model is the most common one in SPR sensorgram data analysis. Other methods are also available for specific biological interactions.
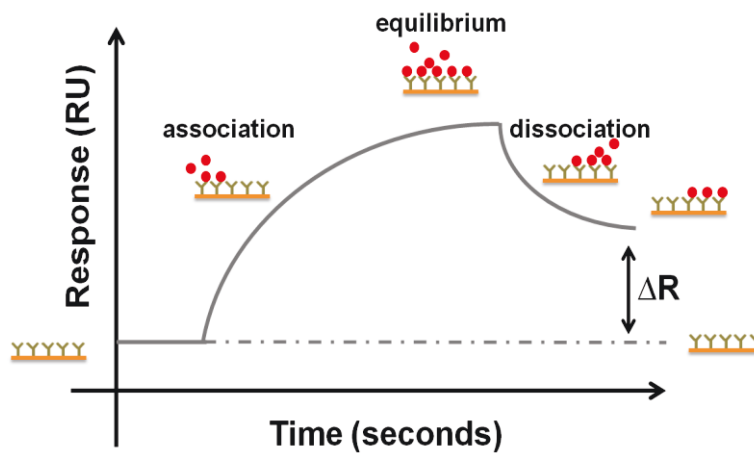
Figure 1-10. A SPR sensorgram in real-time mode whose recording response (resonance angle, reflected light intensity or resonance wavelength shift) changes as a function of time. Included in this sensorgram are the association/equilibrium/dissociation phases that can be used to derive the interaction kinetics.

1.3 Localized SPR

When the size of the metal decreases down to 1–100 nm, and therefore much smaller than the wavelength of light, the SPs can be excited by direct illumination on the metal by a multi-wavelength light source.[41] The collective fluctuation of free electrons in the metal nanoparticles confined to the surface of nanostructures, which is different from the case of thin film SPs that

propagate along the interface of the metal/dielectric medium, is shown in Figure 1-11. This phenomenon is known as localized surface plasmon resonance (LSPR). In this process, as the wave front of the light passes, the electron density in the metallic particle is polarized to one end of the surface and oscillates collectively with the light frequency.[42] Generally, the light–matter interaction involves scattering and absorption, where scattering is related to the incident light re-radiated to a different direction with the same frequency and absorption is associated with light transfer to heat.[43] However, when the particle size is below its free electron mean free path, the scattering effect is not expected. As the size of the metal nanoparticles approaches the de Broglie wavelength of its charge carrier, the excitation of the electron/hole pairs will be confined by the boundary of the particles. The energy level is no longer continuous and will split into discrete quantized states, as shown in Figure 1-12.[44] In addition, the spacing between the electronic energy levels increased with a decrease in particle size.[44] The LSPR properties (spectrum distribution, peak position, scattering/absorption ratio) of metal nanostructures are strongly dependent on the chemical composition, size, shape, geometry, structure as well as the surrounding environment.[43] For example, as shown in Figure 1-13, the resonance peak of the LSPR spectrum of Au nanoparticles shifted from ~520 nm to the near-infrared field, ~820 nm, as the shape evolved from spherical to rod-shape.[45] In addition, the red shift in the spectrum can be observed as the nanorod aspect ratio further increases. In Figure 1-14, broad plasmonic tunability was demonstrated by the variation of the hybridized nanoparticle components. The spectrum resolved a blue shift from ~1020 nm to ~740 nm as the Au shell thickness increased from 5 nm to 20 nm on the 60 nm silica core.[46]
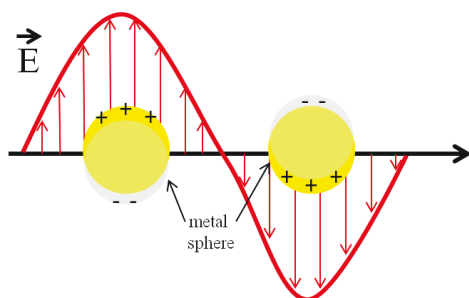
Figure 1-11. A schematic illustration of the collective oscillation of free electrons confined in metal nanoparticles, which is responsible for localized surface plasmon resonance.
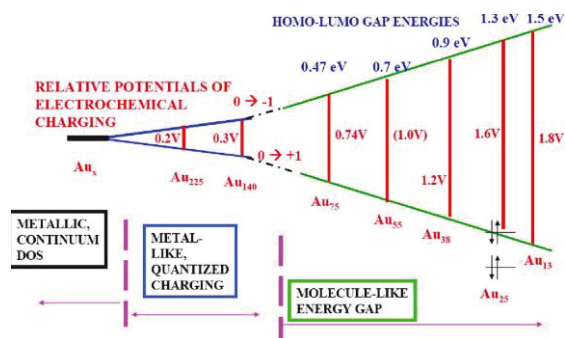
Figure 1-12. A summary of the energy gap (between the highest occupied molecular orbital and the lowest unoccupied molecular orbital) and the electrochemical energy gap (the spacing between the first oxidation and the first reduction peaks) as a function of the core size of Au nanoparticles.[44] Reprinted with permission from Ref. 44. Copyright 2008, American Chemical Society.
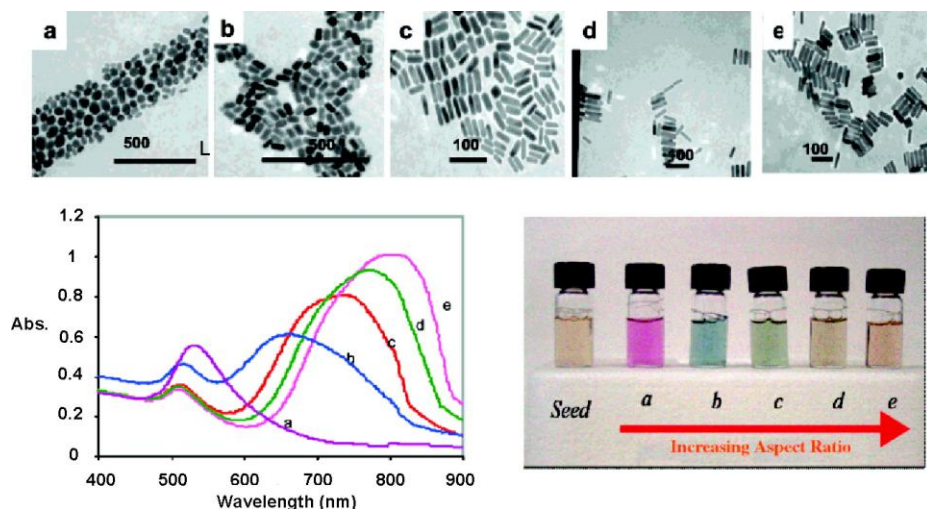
Figure 1-13. Transmission electron micrographs (top), optical spectra (left) and photographs (right) of aqueous solutions of Au nanorods of various aspect ratios. The seed sample has an aspect ratio of 1. Samples a, b, c, d and e have aspect ratios of 1.35 ± 0.32, 1.95 ± 0.34, 3.06 ± 0.28, 3.50 ± 0.29 and 4.42 ± 0.23, respectively. Scale bars: 500 nm for a and b and 100 nm for c−e.[45] Reprinted with permission from Ref. 45. Copyright 2005, American Chemical Society.
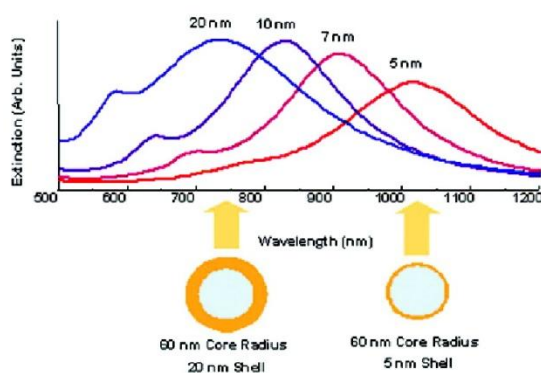
Figure 1-14. Photographs of tunability of metal nanoshells (top) and optical spectra of Au shell−silica core nanoshells (the labels indicate the corresponding Au shell thickness).[46] Reprinted with permission from Ref. 46. Copyright 2004, SAGE Publications Inc.

LSPR spectroscopy using nanomaterials offered similar advantages as the planar metal film based analogue with label-free and real-time measurement characteristics, both of which were able to provide thermodynamic and real-time kinetic information of the binding process.[47] The LSPR platform has other benefits along with those mentioned above such as less sample volume for measurements and simplified optical parts involving instrumentation.[48] The only disadvantage is that it is not as sensitive as planar based SPR spectroscopy. In the next section, the theory governing the optical properties of metal nanoparticles will be given in terms of key equations. The major synthetic method of nanostructures also will be covered.

1.3.1 Theory of LSPR

The plasmon resonance of metallic nanoparticles can be treated with the Drude model, which assumes that the positive metal ion is fixed in place and the valence electrons are dispersed around the core. When the incident light shines on the spherical metal nanoparticle, whose size a is much smaller than the incident light wavelength λ, the electric field intensity around the metallic nanoparticles can be considered as static. The electric field can be expressed by Eq. (35) by solving Maxwell's equations with a quasi-static approximation,[49]

$$E(x,y,z) = E_0\hat{z} - \left(\frac{\epsilon_m - \epsilon_d}{\epsilon_m + 2\epsilon_d}\right) a^3 E_0 \left[\frac{\hat{z}}{r^3} - \frac{3z}{r^5}(x\hat{x} + y\hat{y} + z\hat{z})\right] \tag{35}$$

where ϵ_m and ϵ_d are the frequency-dependent dielectric constant of the metal and dielectric medium, respectively, a is the size of the nanoparticles and E_0 is the incident field intensity. The

equation shows that the electric field can be greatly enhanced in comparison to the incident field when $\epsilon_m = -2\epsilon_d$, which is a condition fulfilled for surface plasmons resonance in metallic nanoparticles. In addition, It can be concluded from Eq. (35) that both the size of the nanoparticles (a) and the dielectric constant of the surrounding environment (ϵ_d) have a significant impact on the magnitude of the electric field around the nanoparticle; this is consistent with the experimental results.

The extinction spectrum of spherical nanoparticles, combining the scattering and absorption effects, exhibits a peak at the LSPR frequency. By solving Maxwell's equations, Mie showed that the wavelength dependent extinction (sum of absorption and scattering) can be expressed by Eq. (36),[50]

$$E(\lambda) = \frac{24\pi^2 N a^3 \epsilon_d^{3/2}}{\lambda \ln(10)} \left[\frac{\epsilon_{m2}(\lambda)}{(\epsilon_{m1}(\lambda) + \chi \epsilon_d)^2 + \epsilon_{m2}(\lambda)^2} \right] \tag{36}$$

where N is number of finite polarisable elements that are able to interact with the applied electric field individually, ϵ_{m1} and ϵ_{m2} are the real and imaginary part of the frequency dependent dielectric constant of the metal, respectively, ϵ_d is the frequency dependent dielectric constant of the surrounding dielectric medium, a is the size of the nanoparticle and χ is a factor correlated to the particle shape. The value of χ is 2 in the case of a spherical nanoparticle, and approximations were needed for other geometries.[49] Eq. (35) demonstrated that the LSPR peak can be manipulated by multiple parameters, such as the size, shape and chemical component. In the case of LSPR in biosensing, the extinction peak of the spectrum shifted to a higher value as the biomolecules binding to the nanoparticle surfaces due to dielectric media refractive index $\left(n = \sqrt{\epsilon_d} \right)$ increased. The maximum wavelength shift can be characterized by Eq. (37),[16, 51]

$$\Delta\lambda_{max} = m\Delta n(1 - e^{-2d/l_d}) \tag{37}$$

where m is the refractive index sensitivity, Δn is the refractive index difference between the biomolecules and the bulk solvent, d is the effective thickness of the absorbed biomolecule layer and l_d is the characteristic electromagnetic field decay length. Thus, quantitative information about the biomolecule coverage on the nanoparticle can be obtained by monitoring the LSPR peak shift ($\Delta\lambda \propto d$). In addition, the binding constant and rate constant can be derived from the plot of $\Delta\lambda_{max}$ as a function of concentration and time, respectively.

1.3.2 Nanoparticle Synthesis

The synthesis of nanoparticles has continuously been an active topic of research because of the difficultly in generating the desired size, shape and monodispersity of nanoparticles.[45, 52] Generally, two different strategies can be applied in nanoparticle synthesis: "bottom up" and "top down" techniques.[53] The bottom up method involves the assembly of atoms into nanostructures whose atoms were normally formed by ion reduction using wet chemistry, whereas the top down technique employs different lithographic techniques, which result in removing the bulk materials and leaving the desired nanostructures.[50, 54]

In the bottom up approaches, solution phase synthesis is a versatile method of generating monodispersed nanoparticles with a controlled size, shape, component and structure.[55] Generally, the reduction of metal salts was involved in this process with the addition of a capping agent, which is used as a stabilizer that controls the growth of nanoparticles as well as prevents them from particle aggregation. The capping agent can be small molecules (thiol ligands) or macromolecules (polymers) that are able to absorb on the metal surface and prevent aggregation by electrostatic interactions. Some commonly used reducing agents are citrate,[56] hydrides,[57] alcohols[58] and hydroxylamine.[59] In addition to carrying out a reduction chemically, other

approaches are also available such as electrochemical,[60] photochemical,[61] sonochemical,[62] etc, approaches. Good reviews[63] are available that refer to the nanoparticle synthetic details based of the wet chemistry.

In the top down techniques, conventional lithography techniques, including electron beam lithography (EBL)[64] and focused ion beam lithography (FIB),[65] are applied to remove large amounts of metal material to control the size, shape and interparticle distance of nanostructures. In EBL, the resist film was scanned over by a densely focused electron beam for pattern generation. This pattern then serves as a sacrificial mask for metallic nanostructure formation either by milling or depositing depending on the desired geometry. FIB is similar in approach by applying a beam of ions instead of electrons to generate both additive and subtractive patterning. Both of these techniques can generate a well-defined nanostructure with a precisely controlled size, shape, interparticle distance and structure, with a resolution down to 10 nm. However, these techniques suffered from a low throughput and a high cost for industrial scale production. Alternatively, some unconventional lithography techniques have been developed recently for nanostructure synthesis, such as nanosphere lithography (NSL),[66] colloidal lithography (CLL)[67] and soft lithography.[68] Generally, the pattern in these techniques was created by self-assembling either a hard sphere (silica nanoparticle,[69] polystyrene beads[70] or latex particles[71]) or a soft material (polymer colloidal particles)[72] on the substrate. A void will be created between these particles for further metal layer deposition. The metallic structure can be formed after removing these assembled particles by either thermal treatment or solvent removal. Obviously, the periodicity and size of the nanostructure can be tuned dynamically by the assembled process of sacrificial particles. In addition, the shape of the nanostructures could be tuned by thermal annealing. The difference between NSL and CLL is that a hexagonally closed packed structure

was formed in NSL, while a random assembly was formed in CLL. Soft lithography involves a set of microfabrications utilizing an elastomer stamp (normally poly(dimethylsiloxane)(PDMS)),[73] conformable photomasks or mold to pattern the material of interest. In conclusion, these unconventional lithography methods have the benefit of low cost, versatility and ability to produce a well-defined structure; these will be promising approaches for industrial production. There are several reviews[50, 74] covering the top down approaches the reader can refer to.

Chapter 2

Building of a Surface Plasmon Resonance

Spectrometer

2.1 Introduction

Surface–surface interactions between at the interface between two surfaces play a major role in many processes that are important in our everyday lives,[75] such as the moving machine parts in engines and the various joints found in the human body. The strength of these interactions dictates the surface and/or interfaces of tribological and rheological properties, such as adhesion, friction and lubrication.[76] Unlike conservative forces, such as those resulting from surface charges, van der Waals interactions or steric effects, the forces between surfaces due to their relative motion lead to energy dissipation while they disappear in the absence of such motion.[77] As two surfaces approach each other in a liquid, lubricating forces arise to prevent a solid contact between the approaching machine parts or between the particles in the concentrated colloidal dispersions. However, as the two surfaces get close enough (5–10 molecular layers), the liquid starts to lose its function and behaves like a solid; this is known as liquid-to-solid transition (manifested as an increase of many orders of magnitude in the effective viscosity).[78] Clearly, the efficiency of liquids to act as low-viscosity lubricants between the moving solid surfaces is limited by the onset of this solid-like behavior as the liquids are being squeezed out

under compression, especially, at low sliding velocities. The attachment of polymer brushes (a dense array of polymer chains whose one end is anchored to a surface) onto surfaces will change the equilibrium surface forces and the form of the motion-dependent interactions dramatically. The dynamic properties of the polymer chains and the polymer–solvent interactions will effect primarily on the surface–surface interactions.[79]

In the case of equilibrium properties of the uncompressed polymer brush layers, the polymer brush conformations can be predicted by self-consistent field theory and molecular dynamic simulations and have been investigated primarily utilizing scattering techniques.[80] Leckband and other groups have demonstrated that the conformation of pNIPAm brushes on a surface is greatly dependent on the grafting density and the molecular weight of the chain.[81] It has been shown that the low grating density and molecular weight pNIPAm chain does not collapse above its LCST.[81a] A vertical phase separation of the pNIPAm brushes was observed below its LCST in the distance–force profile with a dilute outer layer and dense surface proximal layer. However, there is much less understanding about the structure/conformation of the polymer chain on the surfaces under compression and confinement. Although the direct interaction forces between polymer layers can be quantified by force spectroscopy, such as surface force apparatus (SFA)[82] and atomic force microscopy (AFM),[83] less physical structure information of the brushes can be extracted from these direct measurements. As a result, most of our understanding of the polymer structures and the behavior of brushes under confinement have evolved from modeling approaches, including scaling theories, analytical and numerical statistical models and Monte Carlo simulations.[84] By applying the theoretical approaches mentioned above, the polymer behavior on surfaces in a restricted space can be predicted, and the impact of several factors can be investigated such as the solvent quality, grafting density,

chemistry of monomers, brush charges, affinity to substrate, etc. Experimentally, several unique techniques have been developed to investigate these issues by combining optical spectroscopy and a force type apparatus.[85] For example, the Prescott[76] and Cosgrove[86] groups, among others,[87] have applied neutron reflection to study the structure of confined thin films because of the advantages of this technique: 1) sensitive to the composition and concentration variation close to an interface; 2) a high spatial resolution (a few Å) to the reflective interface; 3) a high penetration depth allowing probing of the structures at the buried interface; 4) non-invasive to sample after long time neutron exposure; 5) the ability to probe a single component in a mixed system by replacing the hydrogen atoms with deuterium. However, a drawback of this technique is that a large beam-footprint (500–2500 mm^2) was required to perform the reflection experiments on an acceptable experimental time scale.[76]

To probe the polymer chain conformations in a restricted geometry, it is essential to create an aqueous environment with a controllable and uniform confinement over the course of the measurements; this probably involves a long incubation time for sample stabilization before testing. There were some challenges involved in implementing all the functions mentioned above into the instrumentation design. One of the challenges is the alignment of these two surfaces. In the well-established SFA techniques, such issues can be avoided by applying one flat and one curved mica surface. The flat–curved surface–surface interactions can be approximated to flat–flat surface–surface interactions by the Derjaguin approximation when the distance between the two surfaces changes. Furthermore, the distances between these two surfaces were measured and monitored by an interference spectrometer. In the Prescott group,[76, 85] instead of using two solid substrates, one of these surfaces was substituted by a flexible polymer membrane (Melinex). The contact or separation of the two surfaces over a large surface area can be achieved by inflating or

deflating the membrane film. The distance between these two surfaces can be controlled by adjusting the inflation strength. Another challenge is that it is difficult to maintain a surface uniformity over a large surface area under confinement.

I have built a surface plasmon resonance (SPR) spectrometer that was developed for polymer–polymer interaction studies under confinement, and is described in the current Chapter. SPR is a technique that can probe the events taking place at the metal/dielectric medium interface, and it is very sensitive to refractive index changes near the interface.[88] The refractive index of polymer brushes on the surface is correlated with the polymer chain conformation, therefore, the SPR technique will be a very useful tool for polymer chain conformation investigations. The surface confinement can be achieved by applying a piezo stage controlled probe surface under the sensor surface with the distance monitored by three capacitive sensors synchronically. The parallel and absolute distances between two surfaces were further calibrated by a reflectance probe, which works on the same principle as an interferometer.

In this Chapter, I will first explain the principle and design of this instrument and will follow with the software that was developed to control the motion of the SPR rotation stages and the piezo stages. The detailed procedure of the optics alignment and calibration are also given. This Chapter finishes with the calibration results, conclusions and outlook.

2.2 Materials and Method

The components used to build this surface plasmon resonance spectrometer are listed in the Table 2-1.

Table 2-1. Components of the assembled surface plasmon resonance instrument.

Item	Description	Merchandise
Vibration isolation table	Smart Station UT2 48-12 OST-UT2-48-12-I	Newport, California
IQ damper	IQ-200-UG-12	Newport, California
IsoStation accessory	8FT hip guard, OTS-HG-8	Newport, California
Bottom shelf	8FT shelf below, OTS-BSH-8	Newport, California
Side mount shelf	8FT side shelf, OTS-SH-8	Newport, California
Bracket	Right angle bracket for RV stage, EQ180	Newport, California
Rotation stage	RV240PE, High torque, full step drive	Newport, California
Structural rail	X95-OPT, 63 mm square pattern, 600mm and 400mm	Newport, California
Rail carrier	M-CXL48-50	Newport, California
Clamp post holder	Q-TMS-4	Newport, California
Poster extender	PS-4E	Newport, California
HeNe laser	1.5 mW, R-32734	Newport, California
Laser mount	Cylindrical, 1-1.75 inch, ULM-TILT	Newport, California
Attenuator	LBP-NG4	Newport, California
Detector	Silicon photodiode, 918D-SL-OD3	Newport, California
Polarizer	Glan-Thompson Calcite Polarizer, 10GT04AR.14	Newport, California
Rotation stage (polarizer)	360°, coarse and fine adjustment, RSP-1T	Newport, California
Power meter	High performance optical power/energy meter, 2963C	Newport, California
Iris diaphragm	Aperture, M-DI47.28	Newport, California

Piezo stage	2mrad*2mrad*16µm, PSM2-D	Newport, California
XPS drive module	Drive model for piezo-stack based nanopositioning, XPS-DRVP1, *3	Newport, California
Lens	Plano-convex, BK7, 12.7 mm Dia.,19.0 mm EFL, 430-700nm, KPX040AR.14, *2	Newport, California
Lens	Plano-convex, BK7, 25.4 mm Dia., 150 mm EFL, 430-700nm, KPX100AR.14	Newport, California
Laser line filter	25.4 mm Dia, 632.8±2 nm center, 10±2nm FWHM,10LF10-633	Newport, California
Mirror mount	1.0 in. Dia., 2 knob adjustment, front load, SS100-F2KN	Newport, California
Lens	Cylindrical plano-convex, BK7, 50.8 mm*25.4 mm, 38.1 mm EFL, 430-700nm,CKX038AR.14, *2	Newport, California
Cylindrical lens mount	50.8mm max optic, ± 5 degree, 2arc sec, CYM-2R	Newport, California
Lens cradle	Cylindrical lens adapter, CYM-2R-A12.7	Newport, California
Lens	Plano-convex, BK7, 25.4 mm Dia., 250 mm EFL, 430-700nm, KPX109AR.14	Newport, California
XPS controller	8-axis universal controller, ethernet, XPS-C8	Newport, California
PWM drive module	For brush and stepper motors, 3A/48V max, XPS-DRV01, *2	Newport, California
Digital multimeter	34401A, $6\frac{1}{2}$ digit, *3	Agilent, California
Capacitive sensor	Model 8810,+/- 5µm range, bandwidth 1 KHz, output +/- 10V, *3	MicroSense, Massachusetts
Lens	Objective, 60x, 0.85NA, 2.9 mm focal length, 5.4 mm clear, MV-60X	Newport, California

Lens positioner	3-axis lens positioner, 0.5 in. Dia., 2.0 in. height, LP-05A-XYZ	Newport, California
Lens (Prism)	BK7, VIS AR coated, TIR wild field angles, hemicylindrical toroid, EFLY 25.4, EFLX infinity, Y25.4, X 50.8, Radius 12.7	Newport, California
Damped post	1.5 in. Dia., 14 in. length, DP14-A	Thorlabs, New Jersey
XYZ manual stage	460A-XYZ, SM-13 micrometer, sensitivity 1μm, 13mm travel range, prism motion control	Newport, California
Z stage	PT-1, 0.001 inch resolution, 1 inch travel range, control probe surface	Thorlabs, New Jersey
Y stage	422-1S, linear stage, 1 inch travel range	Newport, Canifornia
Tilt Stage	GN1, rotation ± 10°, accuracy 0.167°	Thorlabs, New Jersey
Mount Plate	For rotation stage	Machine shop in University of Alberta
Bracket Base	Mount the bracket to the vibration isolation table	Machine shop in University of Alberta
Prism holder		Machine shop in University of Alberta

2.2.1 Design of the SPR Instrument

To study polymer–polymer interactions with respect to confinement conformation changes, the instrument design was divided into two major parts based on the two functions: optical spectroscopy and confinement control. The optical spectroscopy involves a SPR spectrometer that can probe the polymer conformational information on the sensor surfaces. The function of confinement control is to create stable and uniform surface–surface approaches/separations with fine control in a workable range. These two parts are described in detail in the following section. A schematic illustration of the instrumentation is shown in Figure

2-1a. The photographs of the SPR spectrometer from a top and side view are shown in Figure 2-1 b and Figure 2-1 c, respectively.
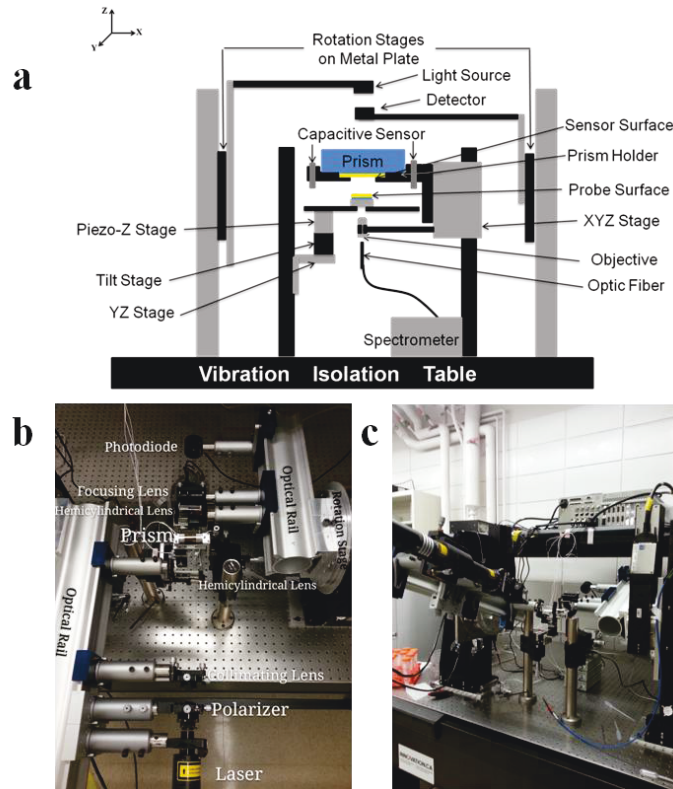
Figure 2-1. a) A schematic illustration of the surface plasmon resonance spectrometer. b) A top view of the surface plasmon resonance spectrometer. c) A side view of the surface plasmon resonance spectrometer.

The SPR spectrometer in this design is based on the Kretschmann configuration (Figure 1-7a), where the SPs are generated by scanning a monochromatic light at varying angles and collecting the reflected light intensity at each angle. Thus, the instrument can be divided into three main parts: an ATR coupler; the excitation light source; the detector.

An ATR coupler normally is made of a high refractive index material with low absorption in a specific wavelength range. In the current SPR spectrometer, a hemicylindrical

BK7 prism was used with a dimension of Y 25.4 mm, X 50.8 mm, Radius 12.7 mm. The prism was mounted on a prism holder (customized by the machine shop in the University of Alberta) and subsequently attached to a XYZ manual transition stage for relocation. The XYZ stage was clamped to a damper stand that was locked on the isolation vibration table. The 50 nm Au coated glass substrate (BK7) was coupled to the back side of the prism (in the XY plane) by a refractive index-matching oil with the Au layer facing downward. The hemicylindrical prism was stationary when rotating the light source and the detectors because it was able to collect light from different angles with the light beam being focused on the same spot.

The excitation light source is expected to generate collimated light when it travels in the prism so that the incident beam has a uniform incident angle. In addition, the collimated light should be scanned from different angles with a wide range. To fulfill these purposes, a monochromatic HeNe laser and a series of optical lenses were secured to an optical rail (X95-OPT) and subsequently attached to a high precision rotation stage (RV240PE) with 0.001° resolution. The rotation stage was mounted to a bracket (EQ180) that was fixed on the isolation vibration table. On the optical rail, the HeNe laser was mounted to the end and was followed by a series of optics in the following order: an iris; a polarizer; a plano-convex lens; another plano-convex lens; a cylindrical lens (50.8 mm*25.4 mm). Each optic lens was mounted in a lens holder and further attached to a post, which finally was secured to the rail by clamps. The positions of the individual optics can be adjusted by tuning the post height and moving the clamps on the rails, where they will be fixed and locked after calibrating.

The detector should be able to collect the reflected light and record the light intensity at individual incident angles to generate the SPR spectrum. This means that the detector and the

light source beam should be scanned simultaneously, and the angle of the light source and the detector should be the same in order to collect the reflected light. In this SPR spectrometer, a silicon photodiode was used as the detector (918D-SL-OD3). It was mounted to another optical rail (X95-OPT) that further was attached to another high precision rotation stage (RV240PE). The rotation stage also was mounted to a bracket (EQ180) that was fixed on the isolation vibration table. First, the reflected light emitted from the prism was focused by a second cylindrical lens (50.8 mm*25.4 mm) and a plano-convex lens before hitting the silicon photodiode detector. Each of these was attached to a post and subsequently secured to the optical rails by clamps.

The two rotation stages were mounted in such a way that their rotation center and the center of the prism in the XY plane are on the same line along the X axis. In addition, the motion of these two rotation stages was controlled by the computer via a XPS-C8 controller, which was controlled in a Laboratory Virtual Instrument Engineering Workbench (LabVIEW) programming environment. The data acquisition was complemented by the power meter also worked under LabVIEW control.

The confinement was achieved by setting another probe surface below the sensor surface (a 50 nm Au coated glass substrate). The material of the probe surface can be varied according to the experimental requirements. The principles of controlling the confinement of the two surfaces are simple. That is, one of the surfaces (sensor surface, the upper one) is rigidly coupled to the back of the prism, and the other surface (probe surface, the lower one) is set below and secured onto a metal plate by vacuum suction. The metal plate was directly mounted to a piezo stage. The probe surfaces can be moved toward or away from the sensor surface using a four-stage

control system with a different accuracy (resolution). First, a coarse control micrometer drive allows for traveling in the Z direction over a range of 2.5 cm with a resolution of 25 μm. The second control employs a micrometer-driven differential spring with a travel range of 2.5 cm in the Y axis. The third control involves a tilt stage for surface parallel alignment with an accuracy of 0.167° in a ± 10° rotation range along the X or Y axis. The fourth control involves a voltage controlled piezo stage that allows (vibration-free) accurate positioning with a resolution of 0.3 Å over a linear range of 16 μm in the Z direction and a 2 mrad rotating range along the X/Y axis. A capacitance technique is used to monitor and measure the separation between the surfaces up to ± 0.1 nm. Three capacitive sensors were set through the holes at the ends of the prism holder in a triangular shape; they can sense the metal plate simultaneously. After the two surfaces are aligned (parallel to each other), the refractive index of a polymer layer on a sensor surface is monitored by the SPR as the two surfaces are moving toward or away from each other by applying one of the four-stage controls. For example, by applying a voltage to the piezoelectric crystal, the distance between the two surfaces will change and be predicted by the capacitive sensor. In the mean time, the reflected light intensity will be recorded simultaneously. This yields the refractive index information of the polymer layer on the sensor surface at a particular surface separation, which can further be used to predict the polymer conformation under confinement. As mentioned above, the principles used to create the surface confinement are usually very simple; the main challenge has always been in designing a mechanical device that will successfully apply these principles at the nanometer level. In addition, a temperature control and feedback system was inserted in the metal stage of the probe surface that was attached to the piezo stage. The heat isolation was achieved by separating the metal stage from the piezo stage with a piece of ceramic disc.

The setup of this instrument is easy to modify by adding other accessories for different measurement purposes. For example, by replacing the probe surface with a fluidic cell, one was able to use the SPR spectrometer to implement all the functions of a commercial SPR instrument. In addition, an objective can be set under the probe surface to collect all the light scattered back and send it to a spectrometer through an optical fiber for further analysis.

2.2.2 Software

The motion of two rotation stages and a piezo stage were controlled by a PC through the XPS-C8 controller. The read out of the photodiode detector (in Watts) and output of three capacitive sensors (in Volts) were collected by a PC. A program was developed that can control and record the movement of the two rotation stages and collect the reflected light intensity synchronically, finally yielded a SPR spectrum with the reflected light intensity change as a function of incident angle. In addition, another program was developed that can record the data from all three capacitive sensors simultaneously. All the programs developed are running under a LabVIEW environment.

2.2.2.1 Introduction of LabVIEW

LabVIEW, also called a visual instrument (VI), is a graphic program platform, which contains a front panel and a block diagram. The front panel is the user interface imitating the appearance and operation of the physical instrument. The block diagram is the program behind the user interface with graphic codes to control the front panel objects. In contrast to text-based programming languages, LabVIEW uses icons instead of lines of text to build an application. In text based programming, the order of execution was determined by instruction, but in LabVIEW,

it was determined by the order of graphic icons and the data flow through the nodes in the block diagram.

2.2.2.2 LabVIEW of the SPR Spectrometer

The application developed for controlling the SPR instrument is shown in Figure 2-2 and 2-3 with a front panel and a block diagram, respectively. The program can be executed by pressing the arrow in the red circle. All parameters in the green rectangle should be exactly the same except for **target position 1** and **target position 2**. The IP address is **192.168.254.254**, which is used to build the connection between the XPS-C8 controller and the PC. The **Group name** is the name of rotation stages, where the one controlling the light source is **Group 1** and the other one controlling the detector is **Group 2**. The **Positioner** name for each of them is **Group1.Pos** and **Group2.Pos**, respectively. The **Target Position** and **Target Position 2** represent the final location of the rotation stages, both of which can rotate from 0.000° to 180.000°. However, for safety and space limitation, the angle normally was set between 0.000° to 65.000°. The relation between the angle of incidence and the target position is that their sum equals 90.000°. For example, the target position of 0.000° means that the incident angle is 90.000°. The **SGamma Parameters** denotes the parameters controlling the rotation stages. For example, the column with **Velocity** represents the motion speed of the rotation stage, and the **Acceleration** describes the acceleration for the velocity, changing from 0°/s to 0.4°/s. The maximum velocity for scanning the rotation stages is 2°/s, and the maximum acceleration is 8°/s². Once the stages start moving, two plots will be generated, as shown in Figure 2-2 in 1 and 2. Chart 1 shows the moving track of rotation stage 1(with the light source). Chart 2 (the XY

Graph) shows the SPR spectrum with the reflected light intensity as a function of incident angle. The data can be exported to an Excel sheet (left click on the graph and select "export to excel").
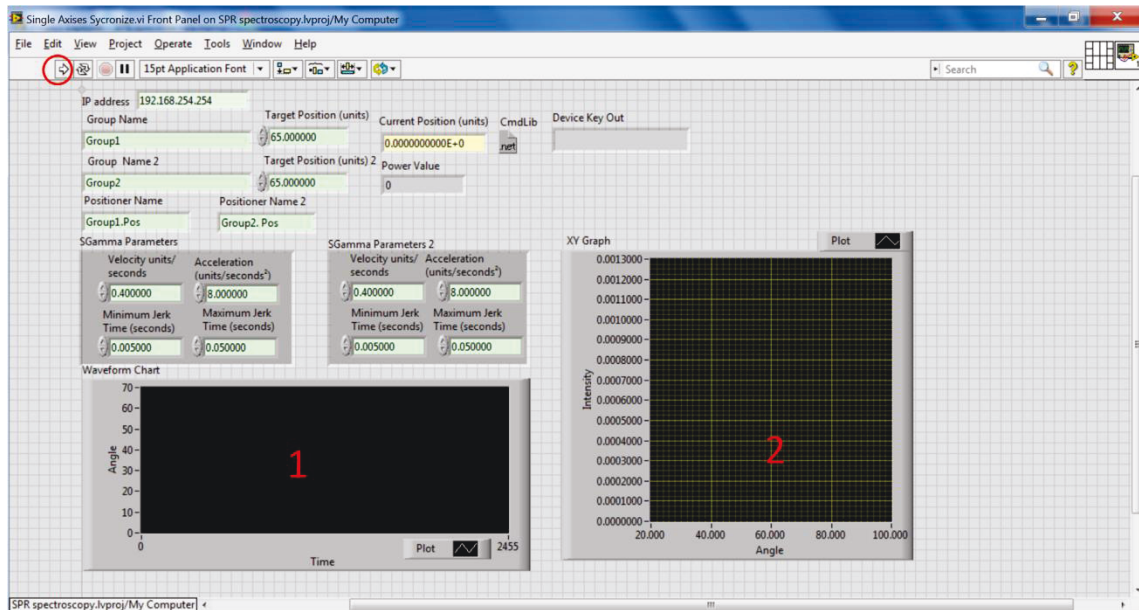
Figure 2-2. Front panel of the LabVIEW program for controlling the SPR instrument.

The block diagram with the functional icon code is shown in Figure 2-3. Each of the icons is correlated to the front panel with same title. For example, the icon with the "IP address" title is associated with the green box of the "IP address" in front panel. The first two gray boxes (called "while" loop in LabVIEW) and the entire icons in the boxes are associated with the rotation stages. The last gray box and the icons inside are associated with data collection of the power meter (photodiode detector) and the position of the incident beam of the rotation stages. For further details of the function of each icon, one can refer to the online LabVIEW tutorial (YouTube is the best source of self-learning).
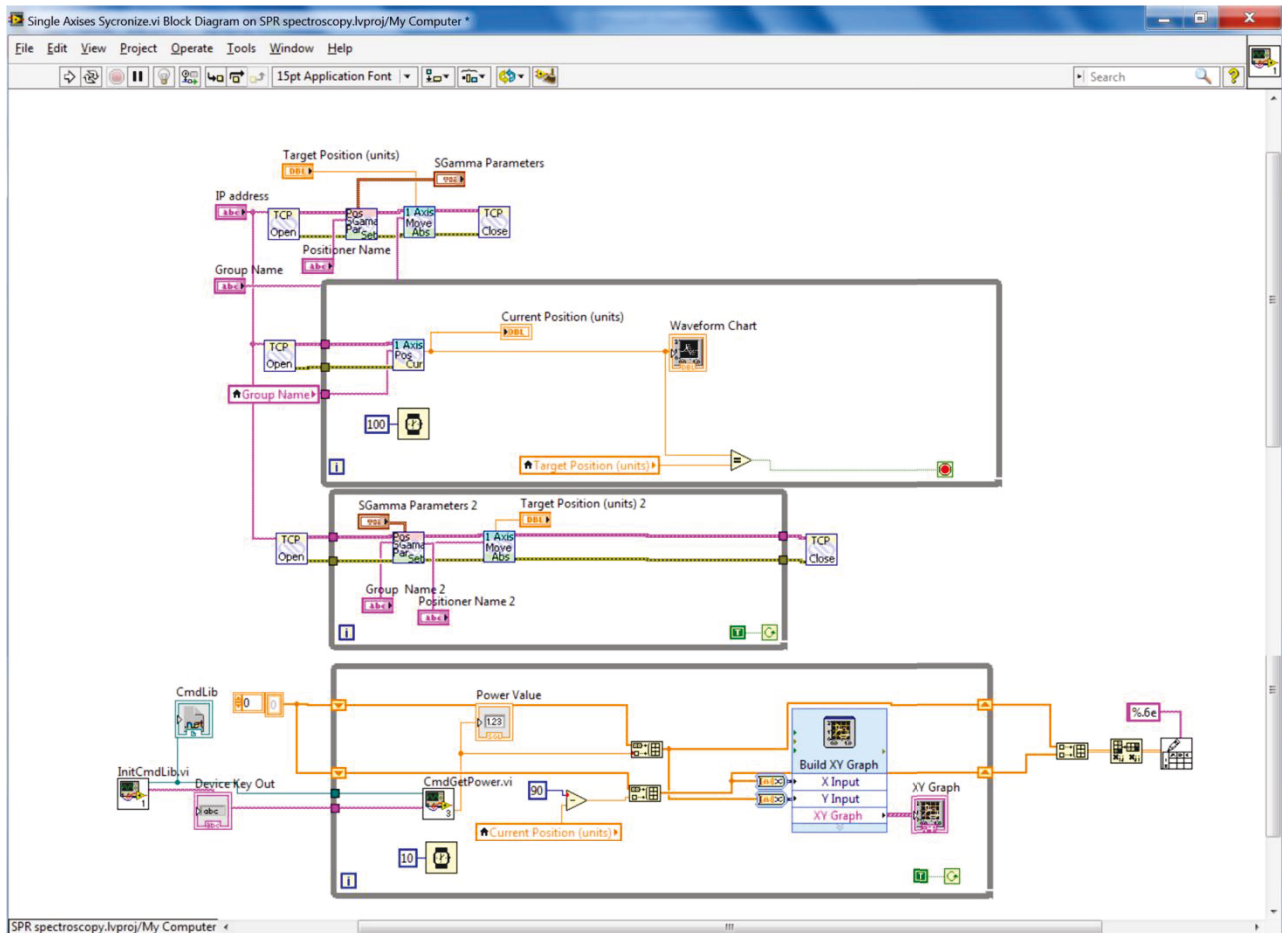
Figure 2-3. Block diagram of the LabVIEW program for controlling the SPR instrument.

2.2.2.3 LabVIEW for Capacitive Sensors

The surface separation can be monitored by capacitive sensors and the outputs of three capacitive sensors are acquired simultaneously. The LabVIEW program of data acquisition is shown in Figure 2-4 and 2-5 with a front panel and a block diagram, respectively. The **VISA resource name**, which is the interface of the instrument and a PC, can be selected from different sources by clicking the triangle button. Each of these VISA resources is associated with one of the capacitive sensors. Each of the waveform charts represents the data collected from individual

capacitive sensors. The serial configuration in the front panel is the default setting. It must not be changed.
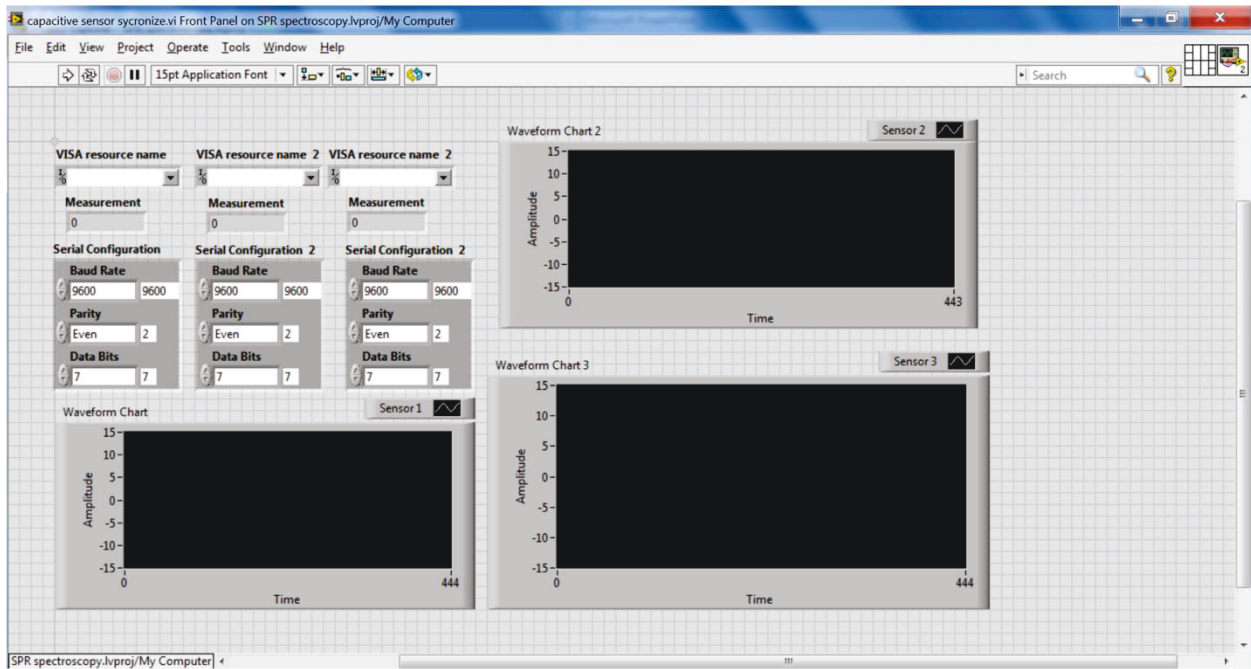
Figure 2-4. Front panel of the LabVIEW program for capacitive sensors.

The block diagram with the functional icon codes is shown in Figure 2-5. Each of the icons is correlated to the front panel with the same title. Each of the gray boxes and the code connected through wires are controlling one of the capacitive sensors. The number 100 in a blue square connected to a watch icon represents the data acquisition frequency. It can be changed according to the requirements. The three while loops are supposed to work in parallel, however, there is a slightly delay of execution in between.
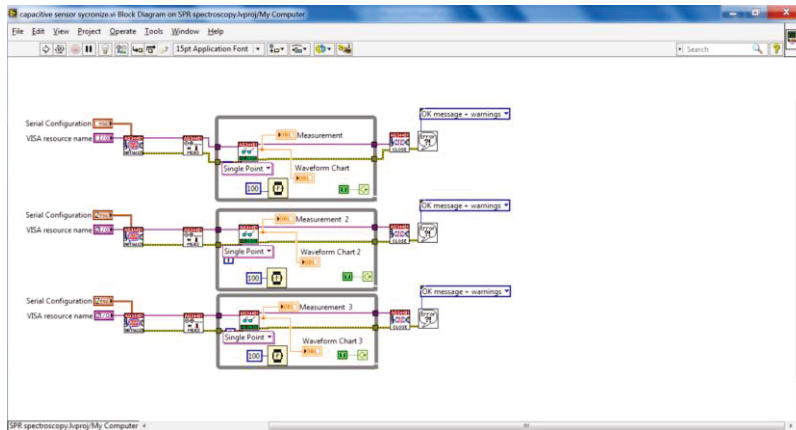
Figure 2-5. Block diagram of the LabVIEW program for capacitive sensors.

2.2.2.4 LabVIEW for Power Meter

The output of the photodiode detector was collected by the power meter, which further sends data to a PC. In the SPR real time mode (the light source and detector are both fixed at a certain angle), the reflected light intensity was collected as a function of time. A separate LabVIEW program (called power meter) was used to acquire data. The front panel and the block diagram of the power meter are shown in Figure 2-6a and 2-6b, respectively. Data can be collected by clicking the arrow button in the front panel. As motioned previously, the icon in the block diagram is associated with the each button having the same title in the front panel. The number 300 in the blue square connected to the icon like a ship represents the data acquisition frequency in units of ms; this can be changed according to the requirements. By clicking the stop button or red filled circle, the data collection execution can be ended. To export the data, left click on the graph and select "export to excel".
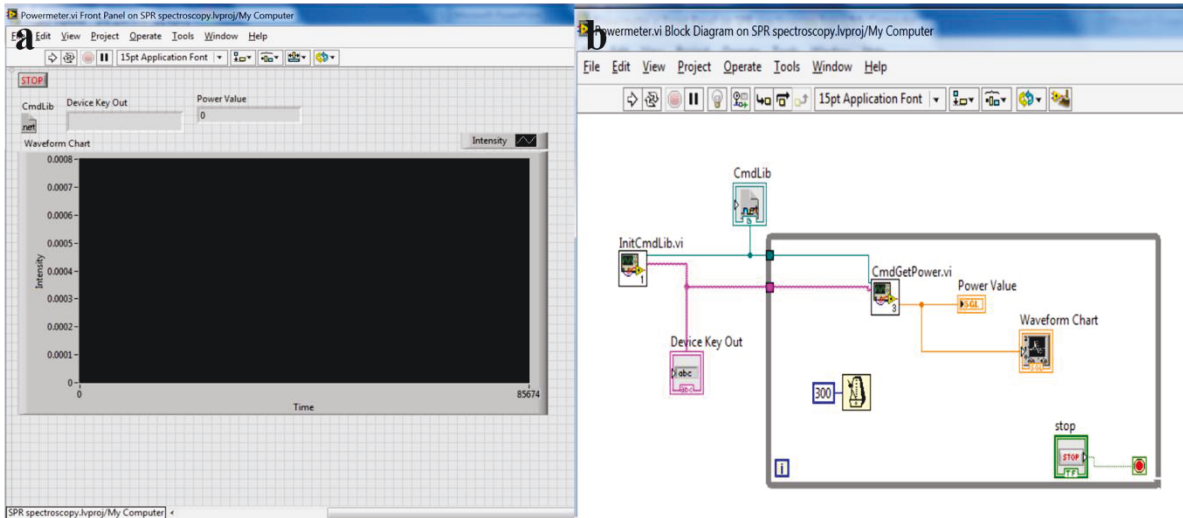
Figure 2-6. a) Front panel of the power meter. b) Block diagram of the power meter.

2.2.2.5 Other Platforms for Controlling SPR Rotation Stages

The motion of two rotation stages also can be controlled by another webpage based application (developed by Newport). This application can aid to diagnose, control and monitor the movement of rotation stages. However, it cannot deploy the synchronic movement of two rotation stages. The link to access the application is http://192.168.254.254/. The screen shot of this webpage is shown in Figure 2-7. Both the user name and password is **Administrator**. After login in, go to front panel>motion>initiation>go to control the motion of individual rotation stages.
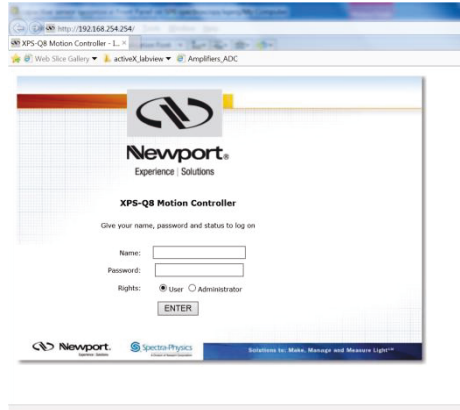
Figure 2-7. Screen shot of a webpage based program for SPR rotation stage controlling.

2.2.3 Alignment

In SPR spectrometer building, alignment involves two major parts: the first is an optical instrument for SPR excitation; the second is the surface confinement. The details for implementing these functions are described below.

2.2.3.1 Optical Elements Alignment

The SPR was excited based on the Kretschmann configuration. A close view of a light beam is shown in Figure 2-8. Two rotation stages are applied to control the movement of the light source and the detector. The first step is to align the center of the two rotation stages and the center of the prism on the same axis (X) such that the reflected light can hit the detector when the two stages move to the same angle. This alignment process was accomplished with the help of staff from machine shop in the University of Alberta. Basically, the rotation center of these two stages was confirmed individually. To do so, first a post was attached to the optical rail with clamps and located it to the center of this rail. By rotating the optical rail from 0.000° to 180.000°, the dial indicator that pinpointed the body of the post could be monitored all the time.

Once the dial indicator stopped moving as the stage rotated, it meant that the rotation center was located. After the rotation centers were confirmed, they were aligned with the prism center onto the same axis.
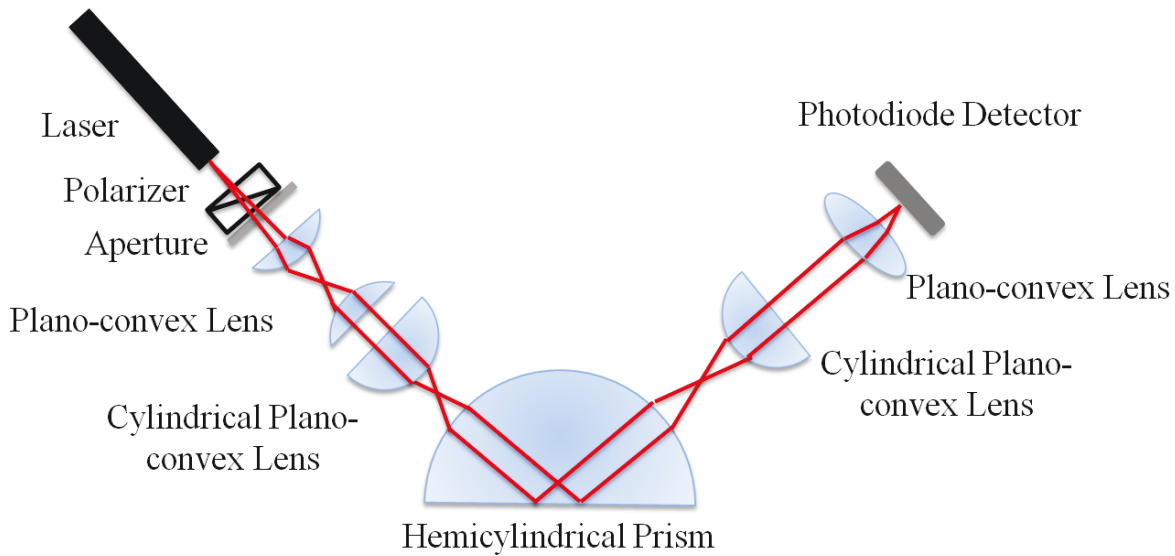
Figure 2-8. A schematic illustration of optical parts in the SPR spectrometer. The red line represents the HeNe laser light beam.

The next step is to align the optical elements in the light source beam. First, the laser light should always be parallel to the optical rail so that the incident angle is equal to the rotation angle of this stage. This was achieved by moving a post with a graph paper back and forth along the optical rail with the laser light on. When the laser light hits the same spot, it means that the laser light is parallel to the optical rail and perpendicular to the axis that has both rotation centers. However, if the light spot on the graph paper moves to the negative side of the X axis as the graph paper is approaching, it means that the laser head is tilted toward the positive side of the X axis, as shown in Figure 2-9. Furthermore, if the light spot is moving toward the negative side of the Z axis as the graph paper is approaching, it means that the laser head is tilted out of

the paper plane. (The positive Z axis is pointing out of the paper plane). Once the alignment was confirmed, this stage was rotated to 90.000° with the laser light on. Then, the spot where the laser light hit the vibration isolation table was marked for further checking. Secondly, a polarizer was clamped to the optical rail once the laser light was aligned. To generate a P-polarized incident light (in our case it should point toward the Z axis when the incident angle is 90.000°), a polarizer was added beside the laser with the polarization axis parallel to the X axis (it should be on the left side of the laser seen from Figure 2-9). Then, the laser head was rotated until the light intensity emitted from the polarizer reached a minimum. Next, the laser head was locked and rotated the polarizer 90° so that the polarization axis is parallel to the Z axis. After the polarizer rotation, the emitted light intensity should reach a maximum. Then, the rotation stage was moved to 90.000° in order to check that the laser spot was hitting the target that had been marked on the vibration isolation table. Thirdly, a plano-convex lens was locked right beside the polarizer with no gap between the two clamps. Another plano-convex lens was further attached to the optical rail, moved back and forth along the rails and locked until it gave out a collimated light. After each addition of a lens to the optical rail, the rotation stage was moved to 90.000° to check whether the laser light is hitting the same spot marked on the vibration isolation table (the hemicylindrical prism was not in the prism hold). Fourthly, a cylindrical plano-convex lens was attached to the optical rail with rotation stages at 90.000°. The lens was moved along the rails and locked once the light emitted from the backside of the prism is collimated.
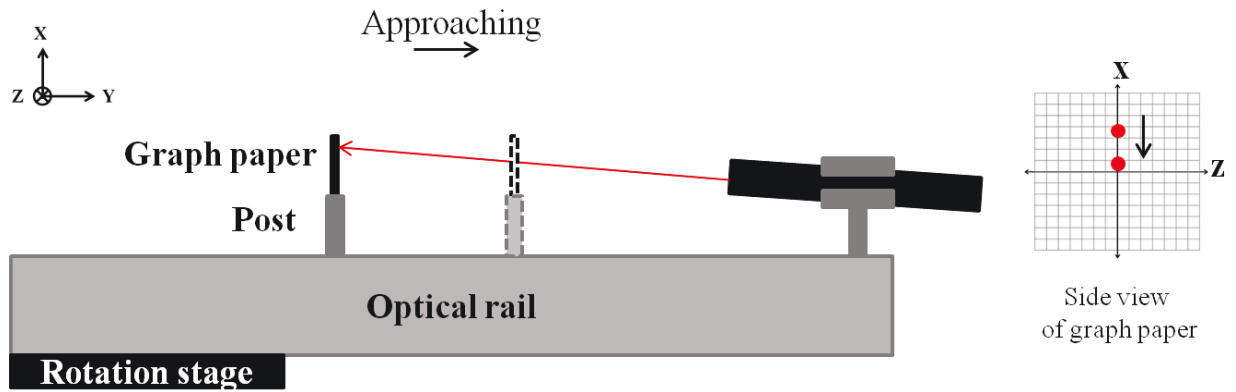
Figure 2-9. Top view of a laser light beam with a laser head tilted toward the X axis. The Z axis is in the direction out of the paper plane. In this case, one is supposed to observe the laser spot moving downward along the X axis as the graph paper is approaching.

The detector beam was aligned by first defining the target. Both rotation stages were moved to 45.000° and a mark was put on the spot that the laser light was hitting on the walls of the top shelf of the vibration isolation table. In this case, the mark was observed as a line instead of a dot. The next step was to find the center of the line. Another cylindrical plano-convex lens was attached to the second optical rail, moved along the rails and locked until a collimated light was emitted. Fine tuning of the lens holder was carried out until the collimated light hit the center that was marked in the previous step. (Both of the rotation stages should be at 45.000° at this point). Next, a plano-convex lens was locked to the optical rails with no gap between the two clamps. The center of the lens was located by fine tuning the lens holder such that the laser light hit the same spot marked on the wall of the shelf. Lastly, the photodiode detector was attached to the optical rail, moved back and forth and locked until the laser light was focused on the detector. Then, both of the rotation stages were moved back to 0.000°.

2.2.3.2 Capacitive Sensor Alignment

As mentioned in the introduction, a uniform confinement over a large surface area is required for surface–surface interaction studies using our system. The confinement was achieved by setting a probe surface below the SPR sensor surface and ensuring that these two surfaces are parallel over the sampling area. In addition, the surface separation was measured by three capacitive sensors simultaneously, ensuring that the surface defined by the bottom of three sensor probes is parallel to the SPR sensor surface, as shown in Figure 2-10. The alignment of these three capacitive sensor probes was accomplished as described below. First, a 50 nm Au coated glass substrate was secured to the probe surface and moved to fully contact with the SPR sensor surface, and a reflectance spectrometer was set under the probe surface to measure the separation between them. The reflectance spectrum can be characterized by Eq. (38),[89]

$$m\,\lambda \;=\; 2\,n\,d\,\cos\theta \tag{38}$$

where λ is the wavelength peak position, *m* is the peak order, *n* is the refractive index of air, *θ* is the incident angle, equal to 0° in this case, and *d* is the distance between the probe and sensor surfaces. By defining each peak from the reflectance spectrum, the absolute distance between them can be calculated. Afterwards, the capacitive sensors were tuned individually until the readout reached the closest limit (-10V). In addition, one can also monitor the reflected HeNe laser light to check that one sensor surface and probe surface are parallel by rotating the light source beam to 90.000°. Once these two surfaces are parallel, the laser light should be reflected back to the light source.
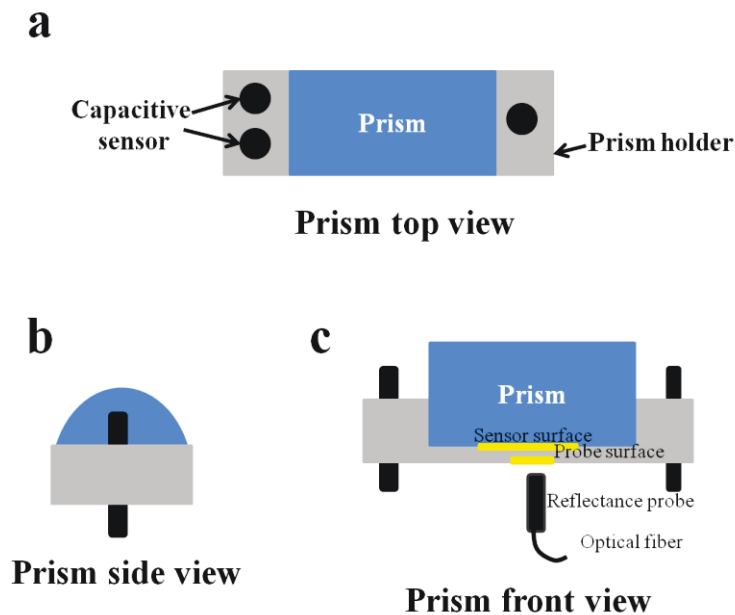
Figure 2-10. A schematic illustration of a prism setup with surface confinement alignment.

2.2.4 Calibration

The SPR spectrometer was calibrated after assembly, which involved the calibration of the optical elements and the surface separation. For the optical elements, the laser light source signal to noise ratio and the offset (error) of the angle of incidence were determined. For the surface separation, the output of the capacitive sensor was calibrated with the reflectance spectrometer, which yields information of the voltage as a function of distance change.

2.2.4.1 Signal to Noise Ratio of the HeNe Laser

The signal to noise ratio of the HeNe laser was determined by monitoring the reflected light intensity as a function of time at a certain fixed angle. The angle at which the reflectance was collected is 80.000°; the laser light was totally reflected at this angle.

2.2.4.2 The Offset of the Angle of Incidence

The error of the incident angle was calculated based on the difference between the experimental and theoretical results of the total internal reflectance angle (TIR). The SPR spectrum of the prism (without a 50 nm Au coated sensor surface) was scanned with the developed LabVIEW program. The TIR is the angle where the reflectance has a significant change. In addition, the SPR spectrum of a 50 nm Au coated sensor surface was scanned in air and water at room temperature.

2.2.4.3 Resonance Angle *v.* Refractive Index Unit

The resonance angle is the angle of the minimum reflected light intensity in the SPR spectrum. It is the angle at which the derivative wave vector of the incident light in the X axis matches that of the free electrons in the Au film and results in surface plasmon excitation. In addition, the resonance angle is very sensitive to the refractive index change of the dielectric medium immediately in contact with it. Hence, the resonance angle shift can be used to derive the refractive index units' change, which further correlates with the polymer layer conformational change.

The relation between the resonance angle and the refractive index unit can be obtained by scanning the SPR spectrum of a series of standard sucrose solutions with known refractive index. Then, the resonance angle of each solution is plotted as a function of refractive index.

2.2.4.4 Capacitive Sensor

The output of the capacitive sensor is a voltage, which cannot directly yield the distance of surface–surface separation. To do so, the reflectance spectrometer was applied as an internal calibration method. The principle is that as two surfaces are approaching or moving away, the data from capacitive sensors and the reflectance spectrum shift are recorded simultaneously, and the distance can be calculated from the reflectance spectrum. Therefore, the voltage at different surface separations can be correlated by a calibration curve of the distance as a function of voltage. The signal to noise ratio of the capacitive sensor was detected by monitoring the voltage as a function of time as the two surfaces are in full contact.

2.3 Results and Discussion

In general, the SPR instrument built for surface–surface interaction studies exhibits a broad dynamic range (25.000°–90.000°) with a resolution of 0.001°. The HeNe laser is relatively stable with a signal to noise ratio of 0.8μW/s over 10 min. The results are shown in Figure 2-11a. This instrument can work in two modes: scanning mode and real-time mode. In the scanning mode, both rotation stages move from a position of 0.000° to 65.000° (correlated to an incident angle of 90.000°–25.000°) at the speed of 0.4°/s to generate a SPR spectrum. From the spectrum, the resonance angle can be obtained and used to derive the refractive index units, which can potentially be used to correlate with the polymer layer conformation. In the real-time mode, the reflected light intensity is monitored as a function of time instead of angular information. A SPR sensorgram can be generated in this mode. In this case, the angle of incidence is fixed at a certain value that is the inflection point where the maximum of reflected light intensity can be achieved when the SPR spectrum shifts. The inflection point can be calculated by the first derivatives of the SPR spectrum. In this mode, dynamic information of events occurring at the Au/dielectric

medium interface can be obtained. For example, the dissociation and association kinetics of biomolecular binding can be derived from the SPR sensorgram by Langmuir Isotherm fitting.

The offset of the angle of incidence was checked by comparing the TIR angle of the experimental result to the theoretical one. Experimentally, the TIR of the prism (41.227°) is obtained by scanning the SPR spectrum without sensor surface loading, as shown in Figure 2-11b. Theoretically, the TIR of the prism should be 41.316° based on Snell's law,

$$\frac{\sin \theta_1}{\sin \theta_2} = \frac{n_2}{n_1} \tag{39}$$

where the refractive index of prism (BK7) is 1.51508 and that of air is 1.00027635. The offset of the angle of incidence is $41.227° - 41.316° = -0.089°$ with an error of 0.215%. Furthermore, the SPR spectrum of a standard surface (a 50 nm Au coated glass substrate) was scanned in air and water. As can be seen from Figure 2-11c, the resonance angle shifted form 43.597° to 74.412° as the dielectric medium switched from air to water. Furthermore, the SPR instrument was calibrated in terms of the resonance angle as a function of refractive index by scanning a series of standard sucrose solutions with different concentrations. The result is shown in Figure 2-11d.
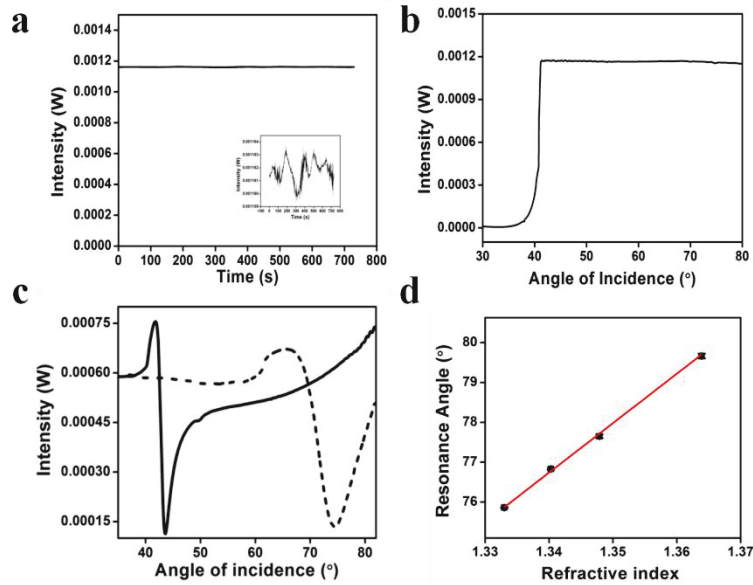
Figure 2-11. a) The reflected light intensity was collected for approximately 10 min at an angle of incidence of 80.000°. The graph insert is a zoom-in picture. b) The SPR spectrum of the prism without a 50 nm Au coated sensor surface. The TIR is the angle where the reflected intensity begins to reach a plateau as the angle increases. c) The SPR spectrum of a 50 nm Au coated sensor surface in air (solid) and water (dash). d) A plot of the resonance angle as a function of refractive index calibrated with a series of sucrose solutions.
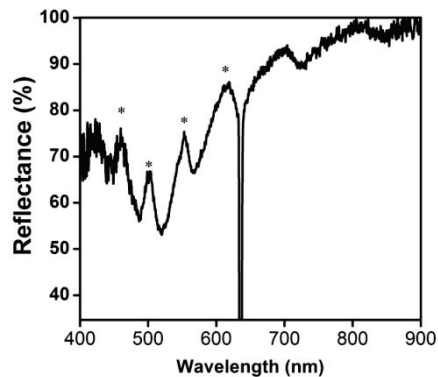
Figure 2-12. The reflectance spectrum when the probe surface and sensor surface are in full contact.

The surface confinement was monitored by capacitive sensors, which were further calibrated with a reflectance spectrometer. From the calibration, the minimum surface separation achieved is ~2.7 μm when the probe surface is full in contact with the sensor surface. It is calculated based on Eq. (38) from the reflectance spectrum shown in Figure 2-12. The asterisk in the spectrum indicates the position of each peak with wavelengths of 462 nm, 502 nm, 554 nm and 615 nm, respectively. The peak order m for each is 12, 11, 10 and 9. The signal to noise ratio of each capacitive sensor was detected by monitoring the output voltage as a function of time without moving the probe surface. The result was 0.172 mV, 0.168 mV, and 0.137 mV for sensor 1, 2, and 3 respectively, while it was claimed to be 0.149 mV by the manufacturer. To determine the distance change from the readout of the capacitive sensor, the calibration curve was obtained by monitoring the readout as the probe surface was separated from the sensor surface manually, as shown in Figure 2-13a. As one can see, the voltage readout was stable for each of the sensors when the probe surface was fixed. However, as the probe surface moved far away, the voltage decreased immediately with a noticeable change. At the same time, the surface separation was recorded from the micrometer. Once the readout stabilized for a period of time, the probe surface was moved away. This process was repeated until the probe surface was out of sensing range. The calibration curve for individual capacitive sensors is shown in Figure 2-13b. The sensitivity for each of the sensors is 8.48674 V/μm, 8.63379 V/μm, and 7.90954 V/μm.
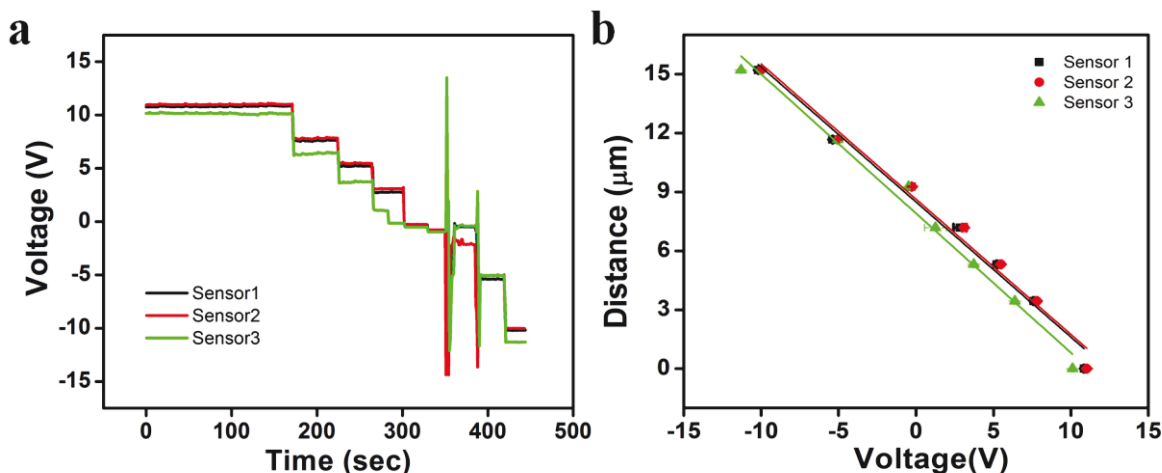
Figure 2-13. a) Capacitive sensors readout collected as the probe surface moved away from the sensor surface. b) Calibration curve of the capacitive sensor readout as a function of distance between the probe and the sensor surface.

Obviously, the surface confinement does not meet the nanometer level requirements. The minimum surface separation is ~ 2.7 μm, which was assumed to be a result of the two surfaces being slightly non-parallel as they are brought together. When they are full in contact, there is a gap at the spot being monitored while they are in contact at other spots. It is a challenge to align two flat surfaces over a large surface area. Since the movement of the probe surface is controlled manually, it is necessary to calibrate with the control of the piezo stage.

2.4 Conclusions and Outlook

A high performance SPR spectrometer was built with an angular resolution of 0.001° and under two modes for surface–surface interaction studies. Compared to currently available commercial SPR instruments, the one we've built here exhibits several benefits: 1. Can be operated in both scanning mode and real-time mode; 2. Has superior angular resolution; 3. An

addition probe surface can be installed to probe surface-surface interactions; 4. Additional objective/optical fibers and spectrometer can be used with the setup to gain real-time information at the sensor/environment interface even in scanning mode, which will potentially be used to analyze light/dielectric medium interactions. In addition, the general function as a commercial SPR instrument can be deployed by attaching other accessories like a fluidic cell. However, improvements are still needed in terms of surface confinement control, which is intended to work at the nanometer level. Once the instrument meets all the requirements mentioned in the introduction, polymer–polymer interactions under confinement can be studied. First, the thickness and graft density of the controllable polymer brushes will be varied on the sensor and probe surfaces via living polymerization, such as atom transfer radical polymerization. By tuning parameters such as polymer chemistry, polymer chain length, grafting density and solvent, one can get much information about the impact of these factors on the conformation change of the brushes (sensor surface) as a function of distance to other brush layers (probe surface). Based on these fundamental studies, surface coatings can be designed with desired tribology under confinement.

Chapter 3

Polymer Film/Au Assembly Enhanced Surface Plasmon Resonance for Sensing

This Chapter deals with the development of an Au film and stimuli-responsive polymer assembly-enhanced sensor by integrating both the planar film plasmon coupling and anaylte induced polymer conformation change into an angular interrogation surface plasmon resonance (SPR) system for small molecules detection. The optical properties of the poly(N-isopropylacrylamide-*co*-acrylic acid) (pNIPAm-*co*-AAc) microgel coated sensor device were investigated as a function of temperature. For the first time the distance dependence of the plasmon coupling behavior in two planar Au films with controlled thickness was studied as a function of temperature in a quantitative manner in terms of the SPR signal. As a proof of concept, dopamine was detected, and the optimized assay with additional 5 nm Au overlayer showed 10-fold and 30-fold sensitivity enhancement over the SPR sensor surface modified only with polymer layer at different concentrations.

3.1 Introduction

Since Wood's first observation of the surface plasmon resonance (SPR) phenomenon in 1902,[90] significant advances have been made to understand[3, 6a, 91] and utilize the phenomenon

further.[8, 92] Surface plasmons (SPs) are the collective oscillation of electrons along the boundary of a "free-electron" metal and a dielectric medium,[1] which can be excited at specific resonance conditions according to the composition of the metal and the refractive index of the dielectric medium that it is contacting.[93] SPs are sensitive to changes in the RI and/or thickness of the dielectric medium in the immediate vicinity ($\sim\lambda/2$) of the metal surface, which makes SPs very useful for label-free plasmonic sensing and biosensing. Most commercial SPR instruments currently available use surface plasmon polaritons (SPPs) that are excited on thin Au or Ag films in attenuated total internal reflection geometry. The SPP-based approach allows for an extremely low detection limit below 10^{-5} refractive index units (RIU).[94] However, it is still a challenge to detect small molecules (< 400 Da) at low concentrations using this phenomenon,[30b] as these small molecules have a small influence on the overall RI/thickness at the metal/dielectric interface.

Generally, SPR spectroscopy detects RI/thickness changes of the dielectric medium within the penetration depth of the evanescent field, with maximum sensitivity on the surface and exponentially decaying sensitivity with increasing distance from the surface. Therefore, the SPRs performance could be improved via several approaches, such as utilizing secondary amplification tags (metal nanoparticles,[95] liposomes,[96] antibodies,[97] etc.) or applying 3D immobilization matrices[98] on the SPR sensor surface that allows multiple binding sites for the analyte within the matrix. In one example, Lee et al.[31] applied polyclonal antibody conjugated carbon-nanotubes as amplification tags in a sandwich immunoassay for human erythropoietin (EPO) and human granulocyte marcrophage colony-stimulating factor (GM-CSF). Using this approach, a detection limit in the picogram range could be achieved. In another example, Lyon et al.[32] utilized Au colloids combined with SPR to detect human immunoglobulin (h-IgG). By

exposing an antibody derivatized surface to free antigens and then secondary antibody-Au conjugates, the signal increased ~25-fold compared to a sensor surface not exposed to AuNPs. By applying this method, they could detect a concentration of h-IgG down to 6.7 pM. The signal enhancement was attributed to the plasmon coupling between the AuNPs and the planar Au film as well as the RI increase caused by the secondary antibody binding to the surface. However, such sandwich-based immunoassays require multiple steps that can introduce error into the measurement and can hinder their use as point-of-care diagnostics.

We developed a SPP-based sensor platform that is able to detect low molecular weight analytes at low concentrations with high sensitivity without using an additional amplification tag. To achieve this, smart polymers were immobilized on the SPR sensor surface that could convert the probe–target interactions into a change in the polymer conformation, which can lead to a significant RI change. In addition, the polymer network provides a three dimensional scaffold for multiple probe immobilization, which can lead to additional improvement in sensitivity.[99]

Smart polymers, also called stimuli-responsive polymers, can undergo reversible chemical and/or physical property changes in response to external stimuli, such as pH, temperature and electric field.[35] Poly(N-isopropylacrylamide) (pNIPAm) is one of the most well-known and well-studied temperature responsive polymers that exhibits a lower critical solution temperature (LCST) of ~32 °C.[36b] Above this temperature, the conformation of pNIPAm switches from an extended/random coil conformation to a compact globular state; this conformational change is reversible over many cycles. Like linear pNIPAm, pNIPAm-based networks (hydrogel, microgel, nanogel) also exhibit an LCST and undergo a volume phase transition from swollen to collapsed as the solution temperature exceeds ~32 °C. It has been shown that the temperature

induced polymer conformation change results in a ~0.1 RIU increase (1.36 to 1.46).[100] Furthermore, pNIPAm-based polymers can be rendered sensitive to other stimuli, in addition to temperature, through post-polymerization modification or copolymerization with other functional groups/monomers.[101] This will allow the polymer conformation to be altered, at constant temperature by exposure to various stimuli and/or the addition of specific analytes.

Our group previously showed that microgels sandwiched between two thin Au layers could yield an optical device with visible color. These devices (referred to as etalons) are able to reflect specific wavelengths of light via constructive/destructive interference of light in the microgel-based cavity of the device. In previous studies, we demonstrated that these devices could be used for a variety of applications, e.g., for sensing and biosensing[37b, 102] and environmental monitoring.[37c, 103] In this Chapter, we utilize the etalon as a sensor in an SPR instrument, and show that signal amplification can be achieved. The configuration of the sensor, shown schematically in Figure 3-1c, contains a monolayer of microgels sandwiched between the SPR Au film and an additional Au layer coated on the microgels. It was hypothesized that the pNIPAm-based polymer film can switch between swollen and deswollen states upon a temperature change or in the presence of a specific analyte. Hence, the changes in refractive index near the surface as well as the distance between these two Au layers can be tuned dynamically, leading to a higher coupling efficiency between the plasmon carrying surface and the etalon's Au layer. Therefore, the SPR performance can be greatly enhanced by molecular binding (or thermal input) induced polymer conformational change and the plasmon coupling effect. In comparison to other groups' strategies mentioned above, our approach requires relatively simple device fabrication processes, not requiring complex equipment that may be

needed for micro/nanofabrication. Furthermore, the devices are extremely inexpensive, and do not required additional reagents to be added to the sensors for enhanced sensitivity.

In the current investigation, the sensor performance was evaluated by exploring how the pNIPAm-based microgel packing density on the sensor surface affected the sensor performance. We also systematically studied the sensitivity of the pNIPAm-based polymer-modified SPR sensor as a function of temperature, as well as its reversibility. Next, the dependence of the Au overlayer thickness on the plasmon coupling efficiency was explored. Lastly, the device with 5 nm additional Au overlayer has been shown to be used to detect dopamine, with enhanced sensitivity over the SPR sensor surface with only microgel modification.
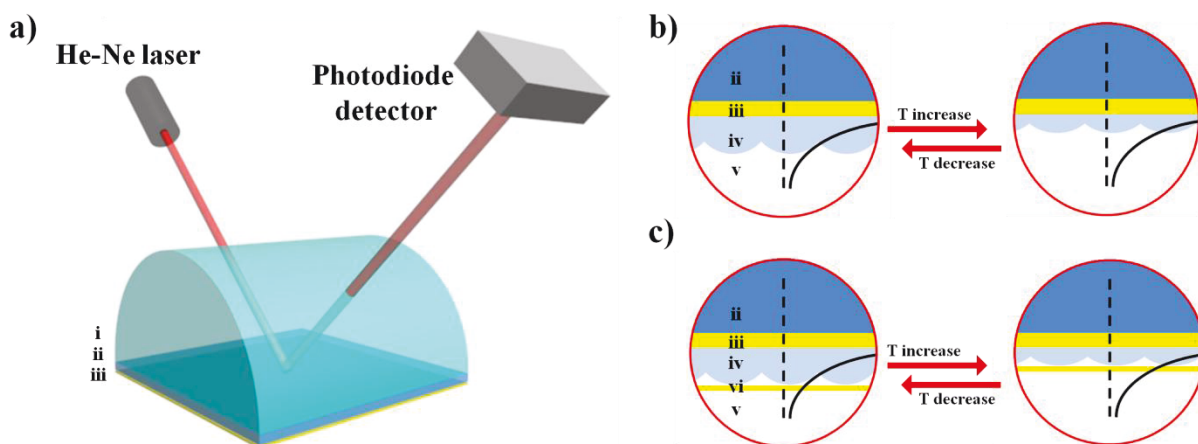
Figure 3-1. a) A schematic of the SPR spectrometer setup equipped with a 632.8 nm HeNe laser, photodiode detector and BK7 hemicylindrical prism (i) and 50 nm Au (iii) coated glass slide (ii). b) A cross section of the SPR sensor surface modified with pNIPAm-based microgel's reversible volume phase transition upon temperature change; ii) glass substrate; iii) 50 nm Au; iv) microgel layer; v) dielectric medium (solvent or air). The black curve represents the exponential decay of the surface plasmons. c) A cross section of the SPR sensor surface modified with pNIPAm-based microgel-Au assembly's reversible volume phase transition upon temperature change; ii) glass

substrate; iii) 50 nm Au; iv) microgel layer; v) dielectric medium (solvent or air); vi) additional Au layer (with variable thickness 1 nm, 5 nm, 10 nm, 15 nm).

3.2 Experimental Section

3.2.1 Materials

Unless stated otherwise, all reagents and chemicals were purchased from commercial sources and used without further purification. N-isopropylacrylamide (NIPAm) was purchased from TCI (Portland, Oregon) and purified by recrystallization from hexanes (ACS reagent grade, EMD, Gibbstown, NJ) before use. N, N'-methylenebisacrylamide (BIS) (99%), acrylic acid (AAc) (99%) and ammonium persulfate (APS) (98+%) were purchased from Sigma Aldrich (St. Louis, MO). Anhydrous ethanol (Brampton, Ontario) was processed by adding the 3 Å molecular sieves. Milli-Q deionized water (DI H_2O) with a resistivity of 18 MΩ·cm was used. Glass microscope slides were purchased from Fisher. Chromium (99.999%) was purchased from ESPI (Ashland, OR) and Gold (99.99%) from MRCS Canada (Edmonton, AB, Canada).

3.2.2 Microgel Synthesis

Two different sizes of poly (N-isopropylacrylamide-*co*-acrylic acid) (p(NIPAm-*co*-AAc)) microgels were synthesized via free radical precipitation polymerization, as described previously.[89] Briefly, for p(NIPAm-*co*-10%AAc)-1 (large) (denoted as MG-1 with 10% mole/mole of AAc), NIPAm (11.9 mmol) and BIS (0.703 mmol) were dissolved in 99 mL of DI H_2O and filtered through a 0.2 μm filter into a 250 mL, 3-neck round-bottom flask. The flask was equipped with a reflux condenser, a temperature probe and a needle for introducing N_2 gas into the reaction mixture. The reaction mixture was heated to 70 °C for about 1 h, then AAc (1.43

mmol) was added to the solution in one aliquot and allowed to stabilize for 5 min before adding the APS (0.2 mmol in 1 mL of DI H_2O) solution. The polymerization was allowed to proceed at 70 ℃ for 4 h under a N_2 environment. The clear solution became turbid within the first few minutes after initiating the reaction. The dispersions were allowed to cool down to room temperature and filtered through glass wool to remove any large aggregates. The microgel solution was cleaned by repeated centrifugations at ~10,000 rpm for 30 min, followed by redispersion in DI H_2O. This process was repeated at least 6 times. The p(NIPAm-*co*-10%AAc)-2, (small) (denoted as MG-2, with a 10% mole/mole of AAc) was synthesized by mixing NIPAm (11.1 mmol), BIS (0.652 mmol), and sodium dodecyl sulfate (SDS, 0.2 mmol) in 190 mL DI H_2O and filtering through a 0.2 μm filter before transferring to a 3-neck round-bottom flask. The flask was equipped with a reflux condenser, a temperature probe and a needle for introducing N_2 gas into the reaction mixture. AAc (1.30 mmol) was added to the solution after the solution was heated to 70 °C for about 1 h. The reaction was then initiated with a solution of APS (0.3 mmol in 10 mL of DI H_2O). The resulting suspension was allowed to cool down to room temperature after reacting at 70 °C for an additional 4 h. Large aggregates were removed by vacuum filtration through a Whatman #1 paper. The microgel solution was then distributed into rehydrated dialysis tubing (12-14k nominal MWCO, 25 mm flat width, Fisherbrand Regenerated Cellulose, Nepan, ON) for purification. The tubes were placed into a 2-L beaker, filled with DI H_2O and stirred for two weeks; the DI H_2O was replaced twice daily.

3.2.3 SPR Sensor Surface Fabrication

Glass coverslips were washed copiously with DI H_2O and anhydrous ethanol, followed by drying with N_2 gas. The glass slide was coated first with 2 nm of Cr and then with 50 nm of

Au using a Torr International Inc. (New Windsor, NY) thermal evaporation system Model THEUPG at a pressure of 10^{-6} torr. Microgels were deposited on the freshly prepared Au coated glass substrate using a previously described "paint-on" technique.[104] Briefly, an aliquot of 40 µL resultant microgel solution was dropped onto the Au coated substrate and spread toward each edge using the side of a micropipet tip. The film was rotated 90° to spread the microgel solution to fully cover the slides. The painting procedure was done on a hot plate set to 30 °C. Then the temperature was increased to 35 ℃ and the microgel solution on the Au coated glass substrate was allowed to dry for 2 h. The excess amount of microgels was removed by washing the surface with a large amount of DI H_2O and further soaking in DI H_2O overnight. Slides with lower microgel packing densities were achieved by depositing a 40 µL aliquot of a diluted microgel solution (three-fold diluted DI water compared to the concentrated samples) on Au coated glass substrates and washing away the extra amount of microgel before the solution dried on the Au.

Additional layers of 2 nm Cr and different thicknesses of Au (1 nm, 5 nm, 10 nm, 15 nm) were subsequently added on top of the microgel layer by thermal evaporation. The sensor devices were soaked in DI H_2O and dried by N_2 prior to use.

3.2.4 Instrumentation

MG-1 and MG-2 particles were imaged with an Olympus IX71 inverted microscope (Markham, Ontario) fitted with a 100 × oil-immersion objective, a 10 × eyepiece, a 1.6 × magnification enhancer, differential interference contrast (DIC) optics and an Andor Technology iXon+ camera (Belfast, Ireland). The hydrodynamic diameter of MG-1 and MG-2 particles was measured by photon correlation spectroscopy (PCS) (Brookhaven Instruments ZetaPlus zeta potential analyzer, Holtsville, NY) as a function of temperature starting at 20 ℃

with 5 increments up to 60 ℃. Measurements were taken in DI H_2O and a pH 3 solution with an average of eleven 30 s acquisitions, and an average of three measurements per sample at each temperature. Atomic force microscopy (AFM) (Digital Instrument, Dimension 3100) was used to characterize the surface topology of the SPR sensor surface. The images were obtained with an Al-coated Silicon SPM tip (Arrow-NCR-50, nanoworld) in tapping mode with a resonance frequency of ~285 Hz and a 0.5 Hz scanning rate. The overlayer thickness of Au was further confirmed by an imaging ellipsometer (Nano film ep4, Accurion, Germany). The SPR instrument is described in detail in Chapter 2.

3.3 Results and Discussion

3.3.1 Microgels Characterization

P(NIPAm-*co*-AAc) microgels (MG-1 and MG-2) were synthesized via free radical precipitation polymerization and imaged using optical microscopy. The images in Figure 3-2 revealed that both sets of microgels were spherical, and exhibited a larger diameter in DI H_2O compared to their diameter in pH 3 solution. The large diameter in DI H_2O was a result of the negative charges on the deprotonated carboxylic acid group leading to Coulombic repulsion and network swelling. The carboxylate groups are protonated at pH 3.0, which neutralizes the charged carboxylate groups and allows the network to contract. The uniformity of synthesized microgel particles (MG-1 and MG-2) were characterized by measuring the particles size distribution in pH 3 solution at 25 ℃ via PCS. The result is shown in Figure 3-3. Both single and narrow peaks were observed for sample MG-1 and MG-2 solutions, which proved the homogenous of resultant microgel particles in an aqueous solution. The apparent hydrodynamic diameter was also investigated via PCS as a function of temperature, as shown in Figure 3-4. At

25 °C, MG-1 exhibits a hydrodynamic radius of 586 nm (DI H_2O) and 422 nm (pH 3), which is consistent with the microscopy data. Likewise, the diameter of MG-2 is larger in DI H_2O (329 nm) compared to pH 3 solution (175 nm). From the temperature-dependent measurement of the PCS-measured diameter, a well-defined volume phase transition can be observed at 32 °C in a pH 3 solution for both MG-1 and MG-2 in Figure 3-4. However, the LCST of p(NIPAM-*co*-AAc) was shifted to a higher value ~ 42 °C in DI H_2O as the inner osmotic pressure of deprotonated polymer networks increased.
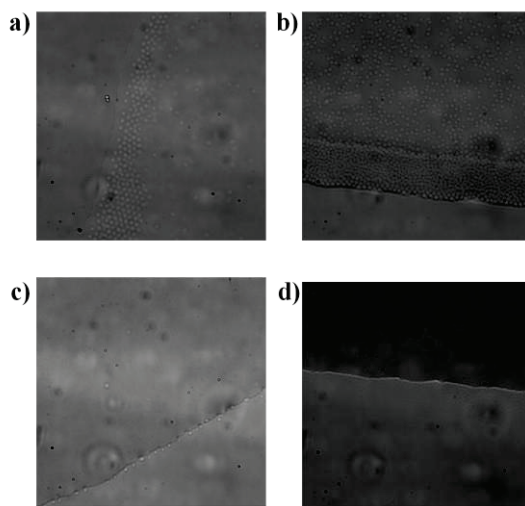
Figure 3-2. The DIC microscopy images of MG-1 particles in DI H_2O (a) and in a pH 3 solution (b), and of MG-2 particles in DI H_2O (c) and in a pH 3 solution (d). All of the images are 80×80 μm.
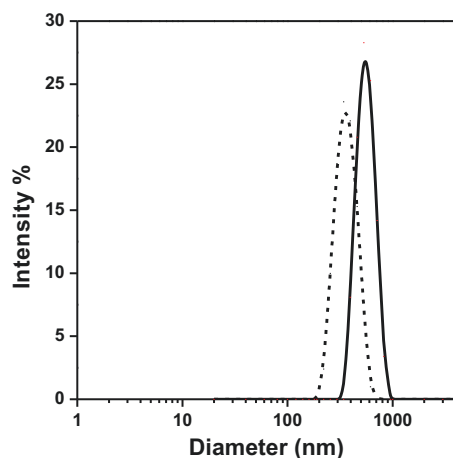
Figure 3-3. MG-1 (solid) and MG-2 (dash) microgels size distributions measured by PCS in a pH 3 solution at 25 °C.
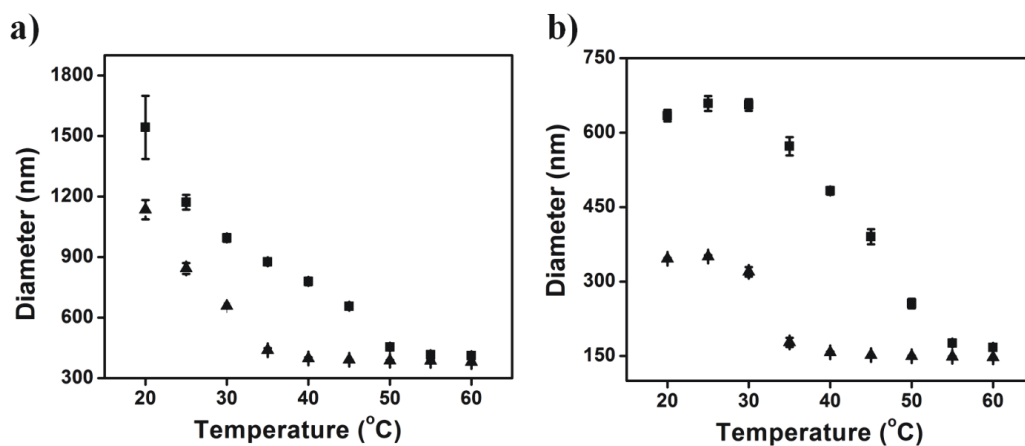
Figure 3-4. The hydrodynamic diameter of MG-1 (a) and MG-2 (b) particles were measured by PCS as a function of temperature in DI H_2O (squares) and a pH 3 solution (triangles).

3.3.2 Influence of Microgel Packing Density on the SPR Performance

SPR sensor surfaces composed of different packing densities of MG-1 microgels were generated by following our previously published "paint-on" protocol.[104] This procedure has been

shown to yield a single microgel layer on the Au surface via a self-assembly process.[104] To determine the packing density of the resultant films, the surface topography of the assemblies was imaged via AFM operated in tapping mode. The images are shown in Figure 3-5a and Figure 3-5c. From the results, we can see that the particle packing density depends on the concentration of the microgel deposition solution and the drying time. That is, when a dilute microgel solution is deposited on the Au surface and washed off the surface before the layer could dry, the microgels formed an incomplete layer and the microgels were spaced far apart from one another (film 1 in Figure 3-5a), with a packing density of ~1.28 particle/μm^2. However, as the concentration of the microgel solution and drying time increased, the microgels became more closely packed on the Au (film 2 in Figure 3-5c), with a packing density of ~5.52 particle/μm^2.

Next, we investigated how the packing density of the resultant film (film 1 and film 2) affected the SPR sensor performance in response to solution temperature variations. To accomplish this, the microgel coated Au sensor surfaces were attached to the SPR prism and incubated in a pH 3 solution, as illustrated in Figure 3-1b. The SPR spectra were collected at 25 ℃ and 40 ℃ respectively, as shown in Figure 3-5b (film 1) and Figure 3-5d (film 2). As is apparent in both cases, the RA and the minimum reflectance increased as the solution temperature increased. However, in the case of film 1 with the lower packing density, only a ~0.3° RA red shift with a ~25 μW intensity increase was observed as the solution temperature increased. In comparison, a higher initial RA was observed for film 2 in pH 3 solution at 25 ℃. In addition, a more noticeable SPR spectrum deformation can be observed in film 2 with a RA red shift of ~2.8° and a minimum reflected light intensity of ~500 μW. The increase in the minimum reflectance was attributed to more light scattering from collapsed microgels as they shrink at temperatures above the LCST; this can be explained by the Mie theory.[105] The red shift

in RA was attributed to the RI increase of the microgels upon collapsing at elevated temperature. Again, SPR is very sensitive to the RI change on the sensor surface, whose overall RI can be characterized by Eq. (40),

$$n = n_p \partial + n_w(1 - \partial) \tag{40}$$

where n_w is the RI of water, n_p is the RI of the polymer and ∂ is volume ratio of the polymer in a unit volume. As can be seen, the overall RI is dominated by the component that has the higher volume ratio. In the case of the high packing density film 2, the surface was fully covered by microgels, whose collapse led to a ~0.1 RIU change (1.36–1.46) as the phase transited from fully swollen to collapsed when the temperature increased from 25 °C to 40 °C.[106] However, as fewer particles were attached on film 1, less RI changes were expected when the solution temperature changes were the same. In addition, less microgel particles will have less of a collective scattering effect on the sensor surface under the same thermal input.
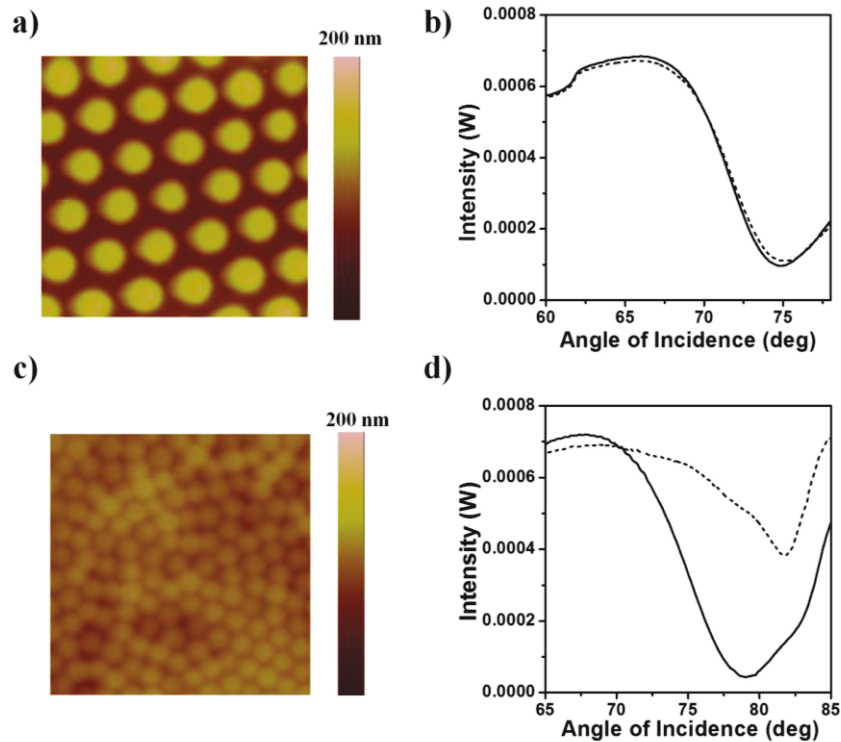
Figure 3-5. a) An AFM image of a MG-1 fabricated film 1 on a 50 nm Au coated glass sensor surface. The scan area is 5 μm × 5 μm. b) The SPR curve of film 1 in a pH 3 solution at 25 ℃ (solid) and 40 ℃ (dash). c) An AFM images of a MG-1 fabricated film 2 on a 50 nm Au coated glass sensor surface. The scan area is 5 μm × 5 μm. d) The SPR curves of film 2 in a pH 3 solution at 25 ℃ (solid) and 40 ℃ (dash).

3.3.3 Temperature Sensitivity of the Dense Microgel Film

Since the effect of particle packing density had been identified, we subsequently evaluated the sensitivity of the densely packed MG-2 microgel modified film to temperature, as well as its reversibility. The MG-2 microgels were chosen because of their comparable particle size to the penetration depth of the SPs. After being loaded on the SPR spectrometer, as shown in Figure 3-1b, the MG-2 microgels modified SPR sensor surface was incubated in a pH 3 solution and the SPR curves were scanned at different solution temperatures. The results are shown in Figure 3-6a. The SPR spectrum became broader and shallower as the temperature increased, which can be attributed to microgel collapse resulting in RI and light scattering changes. Specifically, the polymer density near the SPR Au surface increased gradually as the microgels shrunk. As a result, the penetration of the evanescent wave was disturbed and ultimately yielded a broadened SPR curve. We also noticed that the RA increased and reached a maximum at the LCST, while it decreased as the temperature further increased, as shown in Figure 3-6b. This result can be explained by the distribution of the electric field on the Au film. It is known that the SPs decay exponentially as the distance from the sensor surface increases. The region close to the sensor surface is the point where the electric field is strongest; therefore, the SPR is more sensitive to the increase in polymer density close to the Au film than to its decrease far from the

surface. The polymer collapse is associated with a decreasing film thickness and an increasing polymer density (or RI); these two factors result in a SPR spectrum shift in opposite directions. As the temperature further increased above the LCST, the polymer collapse induced RI changes were limited while the thicknesses still decreased, which resulted in a spectrum shift to lower angle. In Figure 3-6c, the reflected light intensity at each RA was plotted as a function of temperature; it exhibited an inverse trend to the volume phase transition of pNIPAm-based microgels in PCS. The reflected light intensity increased gradually as the temperature increased and reached a plateau at LCST. As before, the intensity increases were mainly due to microgel collapse induced light scattering. It is noteworthy that the thermoresponsivities of a microgel film were completely reversible over a number of cycles without obvious loss in function, as can be seen in Figure 3-6d.
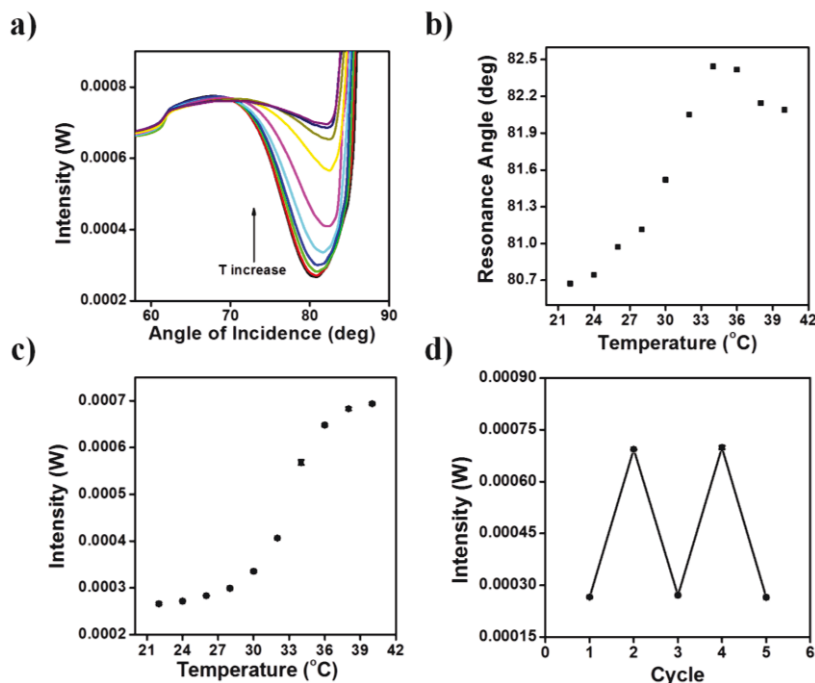
Figure 3-6. a) The SPR spectrum of a MG-2 constructed sensor device in a pH 3 solution at different temperatures from 22 °C to 40 °C in 2 °C increments. b) The RA of a MG-2 constructed film plotted as a function of temperature in a pH 3 solution. c) The reflected light intensity at the

RA of the MG-2 constructed film plotted as a function of temperature in a pH 3 solution. d) The MG-2 microgel film thermal-response reversibility as the temperatures cycle from 22 ℃ to 40 ℃, in terms of the reflected light intensity. The odd numbers represent the intensity at 22 ℃, and the even numbers represent the intensity at 40 ℃.

3.3.4 Au Film Plasmon Coupling Effect

To further enhance the SPR performance, an additional Au film was deposited on top of the MG-2 microgel modified SPR sensor surface by thermal evaporation, which finally yielded Au-MG2-Au assemblies, as shown in Figure 3-1c. We hypothesized that the SPR signal could be amplified by plasmon coupling between the plasmon carrying Au film and the outer Au layer of the device, and that the amplification efficiency would be greatly dependent on the outer Au layer thickness. To confirm our hypothesis, different thicknesses of Au overlayer (1 nm, 5 nm, 10 nm, 15 nm) were deposited on MG-2 microgels modified sensor surfaces, and their SPR sensing performance was compared in terms of the thermoresponsivities. The Au overlayer thicknesses were confirmed by ellipsometry, as shown in Figure 3-7. For simplicity, the resultant SPR sensor devices were denoted as Au_x-MG2-Au_{50}, where x represents the thickness of the Au overlayer on the microgels and 50 is the thickness of the SPR Au sensor surface in units of nm. For example, the Au_1-MG2-Au_{50} indicates that a 1 nm Au film was evaporated on a MG-2 microgels modified 50 nm Au coated glass substrate.
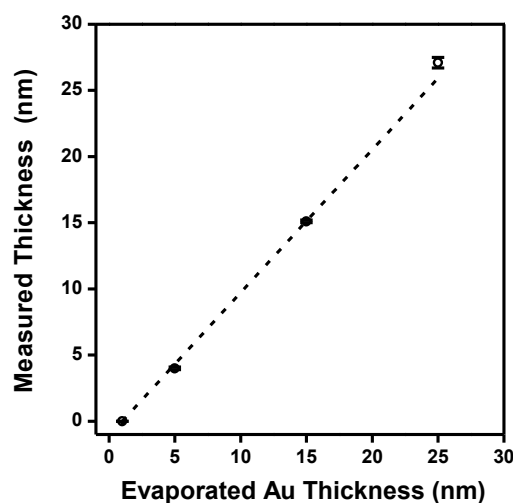
Figure 3-7. The overlayer Au thicknesses, measured by ellipsometry, as a function of the Au thickness recorded from the thermal evaporation instrument. The fitted dash line has a slope of 1.08 with R^2 of 0.999.

The influence of the Au overlayer thicknesses on the SPR performance was investigated by comparing the reflected light intensity change for the devices at various temperatures. The results are shown in Figure 3-8. The reflected light intensity of all the sandwiched assemblies showed a similar trend as the sample of the Au_0-MG2-Au_{50} film (as shown in Figure 3-6c) as the temperature changed. That is, the reflected light intensity increased dramatically as the temperature approached LCST and reached a plateau with further temperature increases. As mentioned above, this effect can be attributed to a temperature induced polymer collapse, which finally led to an increase of RI and light scattering. In addition, some degree of enhancement can be observed with different thicknesses of Au overlayer deposition on the MG-2 microgels. However, such enhancement is not proportional to the increase in the Au overlayer thickness, since the MG-2 microgels with a 5 nm Au overlayer shows the maximum amplification as the temperature increases from 22 ℃ to 40 ℃. Less reflected intensity changes can be observed

when the additional Au layer thickness either increases or decreases under the same amount of thermal input. The reason for signal enhancement can be explained by plasmon coupling between the Au sensor surface and the outer layer Au film coating on the microgels. It is known that the SPs are very sensitive to changes in the vicinity of the sensor surface within a distance of $\lambda/2$, which is estimated to be ~316 nm from the SPR sensor surface in our case. The thickness of Au_x-MG2-Au_{50} assemblies in the solvated state is approximately equal to the hydrodynamic radius of the building block (MG-2 colloidal particles),[89] which is ~175 nm as measured by PCS (Figure 3-4). That is to say, the additional Au film will always be within the surface plasmon probing range. With thermal induced microgel collapse, the two Au films approached each other and resulted in plasmon coupling. The best coupling efficiency was achieved while the thickness of the outer layer Au film is 5 nm. We ascribed this to the fact that the Au surface roughness resulted in a scattering effect. We hypothesized that the Au film was deposited by thermal evaporation, an island structure would likely appear in the initial state instead of a film due to the nucleation of the Au atoms.[107] With more Au atoms being deposited, a film started to form and the roughness decreased. This can be proved by AFM images of Au films with variable thicknesses; this has been published by our group previously.[108] The critical thickness is close to 5 nm. The island structure with the most roughness was supposed to scatter more light, which finally led to an increase in the reflected light intensity. Hence, as the Au film thickness further increased above 5 nm, the enhancement effect became weaker due to the disappearance of the island structures.
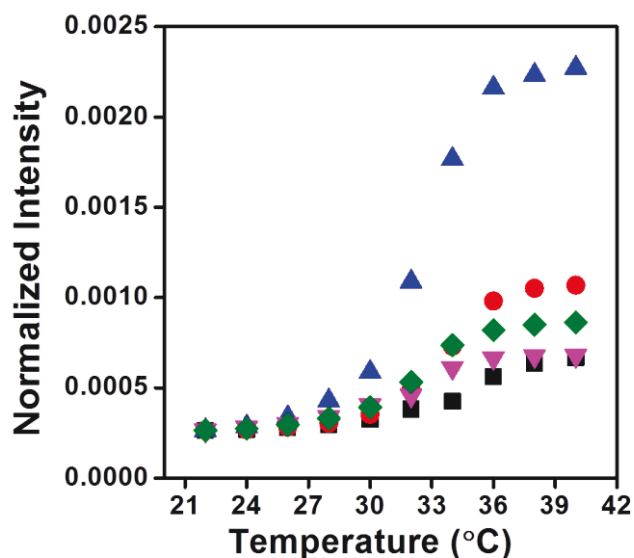
Figure 3-8. Normalized reflected light intensity of Au_x-MG2-Au_{50} assemblies plotted as a function of temperature and dependence of the Au overlayer thicknesses in a pH 3 solution. (X=0 black square, X=1 red circle, X=5 blue triangle, X=10 pink invert triangle, X=15 green diamond, where X represents the thickness of overlayer Au thicknesses.) The Au_x-MG2-Au_{50} assembly was loaded to the SPR spectrometer and incubated in a pH 3 solution at 22 ℃. The temperature was increased to 40 ℃ in 2 ℃ increments after stabilization at each temperature for 5 min. The reflected light intensity at the RA was plotted as a function of temperature for each Au_x-MG2-Au_{50} sample. The intensity was normalized via the function of "Normalize to Point Pick from Graph" in OriginPro 8.5. The point we chose is the reflected intensity of sample Au_0-MG2-Au_{50} at the RA at 22 ℃.

3.3.5 Dopamine Detection

The sandwich structured polymer/Au film assemblies were optimized and showed better sensitivity than polymer film modified SPR sensor surface in terms of thermal responsiveness. Further, we would like to showcase the potential of this unique structure as biosensors together

with thermal sensors. It has been known that pNIPAm-based polymers can respond to other species isothermally with the molecular recognition sites being engineered into networks. Specifically, the equilibrium between the polymer and solvent can be broken by analyte–polymer interactions, and hence the polymer conformation changes. In this investigation, we detected different concentrations of dopamine with SPR sensors based on Au_0-MG2-Au_{50} and Au_5-MG2-Au_{50} and compared their performance. Dopamine is a neurotransmitter that sends a signal to nerve cells in the brain. The dysfunction of dopamine in the nervous system is associated with many diseases, such as schizophrenia and Parkinson's disease.[109] The detection of dopamine down to the nanomolar range has clinical significance. Dopamine can bind to the carboxylic group in p(NIPAm-*co*-AAc) polymer networks, resulting in polymer swelling.[110] Therefore, we expected that the SPR spectra would show a blue shift upon introducing dopamine. Experimentally, the Au_5-MG2-Au_{50} assemblies were first loaded into the SPR spectrometer after incubating in DI H_2O at room temperature, and the spectrum was scanned, as shown in Figure 3-9a (solid line). Then, the incident angle was fixed at the inflection point where maximum reflected intensity changes would be achieved as the SPR spectrum shifts. The reflected intensity was monitored in real-time fashion at this inflection point with a series of dopamine additions. The SPR spectrum was collected again after the last addition, as shown in Figure 3-9a (dashed line). The SPR spectrum showed an obvious blue shift and a minimum reflected intensity decrease in the presence of 5.8 mM dopamine in solution. This result means that the RI decreases near the Au sensor surface, which further indicates the swelling of the Au_5-MG2-Au_{50} assemblies in the presence of dopamine. For quantification, the reflected intensity changes before and after each dopamine addition were calculated and plotted as a function of dopamine solution concentration. The same procedure was performed with the SPR sensor based on Au_0-MG2-Au_{50}

assemblies. The results are shown in Figure 3-9b. The reflected light intensity decreases with more dopamine in the solution for both types of sensors. This can be attributed to the swelling of the p(NIPAm-*co*-AAc) microgels film upon exposure to dopamine, which finally led to a RI decrease and less light scattering. Moreover, the enhancing effect of an additional 5 nm Au film on SPR sensors was obviously demonstrated by the 10-fold and 30-fold sensitivity improvement in different concentrations of dopamine solutions.
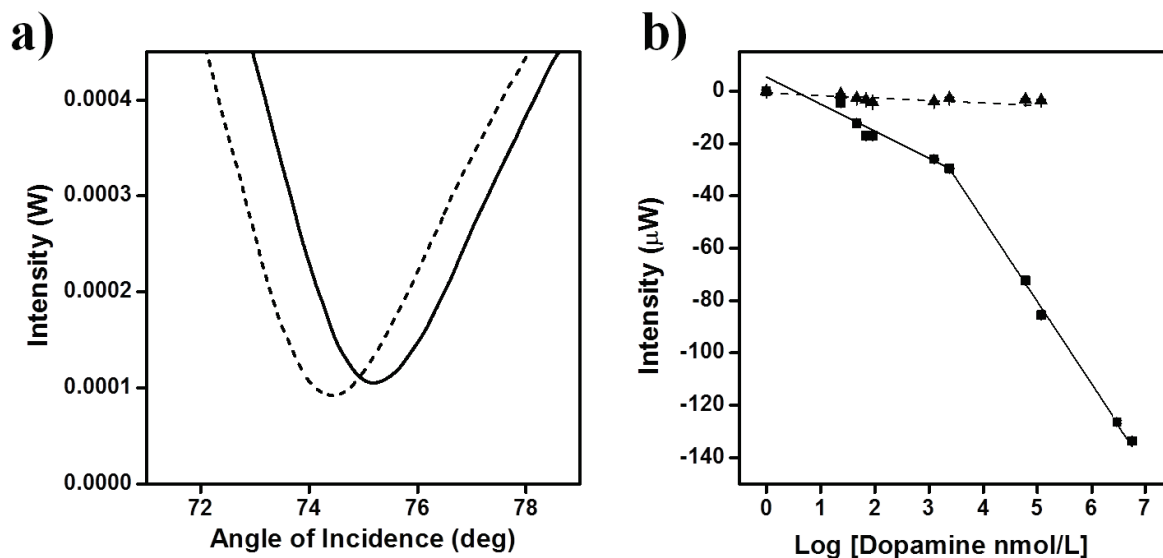
Figure 3-9. a) The SPR curves of the Au_5-MG2-Au_{50} assemblies in DI H_2O (solid line) and in 5.8 mM dopamine (dashed line); b) The reflected intensity change of the Au_0-MG2-Au_{50} (triangles) and the Au_5-MG2-Au_{50} (squares) sensor device at the inflection point as a function of dopamine concentration. Each point represents three individual measurements of different samples. The error bars represent the standard deviations. The dashed line is the linear fit of Au_0-MG2-Au_{50} sensor device reflective intensity changes against logarithm of dopamine concentrations with slope of -0.950 µW/log(nmol/L), intercept of -0.633 µW and R^2 of 0.6535. The solid lines are the linear fit of Au_5-MG2-Au_{50} sensor device reflective intensity changes against logarithm of

dopamine concentrations in two ranges: from 0-2.370μM with slope of -10.358 μW/log(nmol/L), intercept of 5.476 μW and R^2 of 0.9184; from 2.370 μM and above with slope of -31.359 μW/log(nmol/L), intercept of 76.307 μW and R^2 of 0.996.

3.4 Conclusions

Microgel-based thin films deposited on SPR sensor surfaces lead to enhanced SPR signals in response to microgel solvation state changes. This can be related to the concentration of small biomolecules of interest in solution, and to a greater sensitivity than unmodified SPR sensor surfaces. Furthermore, microgel film/Au assemblies have a reproducible response to temperature by showing both a shift in the SPR angle and the reflected light intensity. We also studied how the response depends on the thickness of the Au coating on the microgels. Finally, we showed as a proof of concept that dopamine responsive pNIPAm-based microgels deposited on the SPR sensor surface could be used to detect a range of dopamine concentrations with good sensitivity. These devices could be developed further to detect protein/DNA-based biomolecules of interest.

Chapter 4

Stimuli-Responsive Microgel-Based SPR Transducer for Glucose Detection Using a Competitive Assay with Concanavalin A

In this Chapter, a poly (*N*-isopropylacrylamide-*co*-glycosyloxyethyl methacrylate) (p(NIPAm-*co*-GEMA)) based polymer transducer was developed for glucose quantification via surface plasmon resonance (SPR) spectrometer with improved sensitivity over bare Au SPR sensor surface. By understanding the copolymer conformation behavior (swelling/deswelling) on the SPR sensor surface, such polymer film can be used as a genetic materials for sensitivity improvement in small molecules detection for SPR based technique.

The glucose responsive microgel composed of p(NIPAm-*co*-GEMA) was synthesized by free radical polymerization. The copolymers contracted after introducing Concanavalin A (ConA) owing to the non-covalent crosslinking of the polymer network by the binding of the free pendent glycosyl group in GEMA to one of the four binding pockets in ConA. Such contractions could be removed in the presence of a free glucose solution because of the relatively high affinity between ConA and glucose. By monitoring the contraction/expansion process of the p(NIPAm-*co*-GEMA) microgel constructed film on the surface plasmon resonance (SPR) Au sensor

surface, the concentration of glucose in solution can be quantified. The p(NIPAm-*co*-GEMA) microgel constructed film shows absorption resistance to other proteins and retains a high affinity toward ConA in the presence of other interfering proteins. Experimentally, the microgel composition was characterized by nuclear magnetic resonance (NMR) spectroscopy to confirm the successful copolymerization of GEMA. The thermal responsiveness of the colloidal particle was investigated via photon correlation spectroscopy (PCS) by measuring the particle size as a function of temperature. The particles were visualized by transmission electron microscopy (TEM). A noticeable surface contraction can be observed under atomic force microscopy (AFM) after soaking the p(NIPAm-*co*-GEMA) microgels constructed polymer film in the ConA solution. In contrast, the pNIPAm constructed polymer film shows no change before and after soaking in the same ConA solution. Finally, the competition between the glycosyl group (in the p(NIPAm-*co*-GEMA) polymer network) and the free glucose (in solution) for the binding sites of ConA was monitored by a custom-built SPR instrument, which showed a 9-fold SPR signal enhancement than bare Au SPR sensor surface in the specific physiological concentrations of glucose detection. The polymer conformation change induced by biomolecules interaction showed more refractive index (RI) change than that by solely biomolecules.

4.1 Introduction

The development of rapid, affordable and portable technologies for diagnosing and treating infectious and chronic diseases is of global importance and a major challenge that many researchers are trying to address.[48, 111] While many examples of diagnostic technologies exist (e.g., cell culture methods[112] and enzyme-linked immunosorbent assay (ELISA)[113]), they are typically confined to lab-based settings where the appropriate environment and infrastructure is

in place to ensure the technology functions properly.[114] However, there are many situations that can benefit from performing a diagnostic test outside of the lab, therefore, point-of-care (POC) diagnostic technologies have been developed over the past few decades.

A number of technologies are currently commercially available, e.g., home pregnancy tests,[115] biological fluid testing (urinalysis)[116] and drug screening,[117] with many being amenable to use in resource-limited settings where inexpensive, robust and rapid tests can have a major impact on improving human health.[114b, 118] Optical biosensor platforms have many benefits that can be exploited for POC applications.[114b, 119] For example, the simplicity and the setup in AuNP-based colorimetric assays make it possible to identify the presence of a target by naked eye, which definitely reduces the necessity for technical personnel training. Some of the traditional optical sensors are including photonic crystal fibers,[120] interferometric devices[121] and plasmonic nanoparticles.[48-49, 122] Surface plasmon resonance (SPR) has emerged as one of the very useful optical sensors that was able to detect RI/thickness changes at the surface of a Au film, which can further be related to the surface binding/reactions.[10d] Surface plasmons (SPs) are the collective oscillation of electrons along the interface of a free electron metal (Au, Al, Cu) and a dielectric medium.[1] When the momentum of incident light matches that of the free electrons in the metal, the SPs will be generated as an evanescent wave field that decays exponentially as a function of distance from the SP-supporting surface and propagates along the metal/dielectric medium interface. In angular interrogated-based planar SPR spectroscopy, the reflected light intensity was recorded as the incident angle scanning, which finally yielded a SPR spectrum with the reflectance changes as a function of incident angle. Spectrally, a dip will be observed due to the absorption of SPs. The resonance angle (RA) is defined as the point where the minimum reflectance is reached. Two modes can be operated in the angular interrogated-based planar SPR

platform, a scanning mode and a real time mode. Specifically, when the biomolecules are detected in the scanning mode, they can be quantified by subtracting the RA shift before and after the bio-interaction occurs in the SPR spectrum, where the RA shifts are associated with refractive index increases due to the biomolecules binding. In the real-time mode, the binding process is monitored during the whole course that the RA or reflectance is recorded as a function of time; the incident angle is fixed at a certain value. The dissociation and association kinetics then can be derived from the SPR sensorgram by Langmuir Isotherm fitting.

One of the challenges in utilizing SPR spectroscopy in biosensing is that it is difficult to detect small molecules (< 400 Da) in low concentrations because of the undetectable refractive index changes accumulating from the target molecules. Stimuli-responsive polymers have emerged as alternative materials for SPR signal enhancement along with the antibody/antigen sandwiched based amplification assays.[123] Stimuli-responsive polymers are macromolecules that can change their chemical and/or physical properties upon exposure to external stimuli, e.g., temperature, pH, light, analyte and application of external fields (magnetic/electromagnetic).[35,124] Poly (N-isopropylacrylamide) (pNIPAm) is a well-known and extensively studied temperature responsive (thermoresponsive) polymer that exhibits a lower critical solution temperature (LCST) of ~32 °C.[36] As a result, pNIPAm exists as a solvated random coil at T < LCST and transits to a relatively desolvated globule at T > LCST. Like the linear pNIPAm, crosslinked networks of pNIPAm (hydrogel) and colloidally stable particles (microgels or nanogels) also can be synthesized while retaining their thermoresponsivities. PNIPAm can be made to respond to additional stimuli via copolymerization with other functional/responsive monomers. For example, the pH responsive microgels can be synthesized by copolymerizing with acrylic acid, which has a pK_a around 4.25. When the pH value is above the pK_a, the

polymer networks will swell due to the Coulumbic repulsion of negative charges as deprotonation takes place.[125] In addition, most of the biomolecules can be attached further to the polymer networks through carbodiimide coupling reactions.[126] When the specific interactions between the target (biomarker) and the recognition sites on the polymer networks are strong enough, the polymer conformation can be altered isothermally. Thus, the biomolecule interactions were transduced into an optical signal (RI change) that can be applied to amplify the SPR signals.

In current investigation, I developed an optical transducer that potentially can be coupled to a portable SPR device and used as a POC device. Glucose was chosen as a model molecule for detection, as a proof of concept, due to its clinical significance;[127] the sensing mechanism is shown in Figure 4-1b. Specifically, the glycosyl group in poly (*N*-isopropylacrylamide-*co*-glycosyloxyethyl methacrylate) (p(NIPAm-*co*-GEMA)) microgels can bind to any one of the four binding pockets in Concanavalin A (ConA) and result in the contraction of polymer networks.[128] As the glucose has a higher binding affinity toward ConA, the latter will disassociate from the polymer networks, and the contraction of the polymer networks can be removed. By monitoring the microgels conformational change (swelling/deswelling) on the SPR sensor, the number of glucose molecules in solution can be quantified. It was hypothesized that the conformation of the polymer-based film can be altered by the physiologically relevant concentrations of glucose that output as a detectable optical signal. By incorporating a p(NIPAm-*co*-GEMA) microgel film to a portable optical detector, the fabrication of a home glucose monitoring device is very promising.
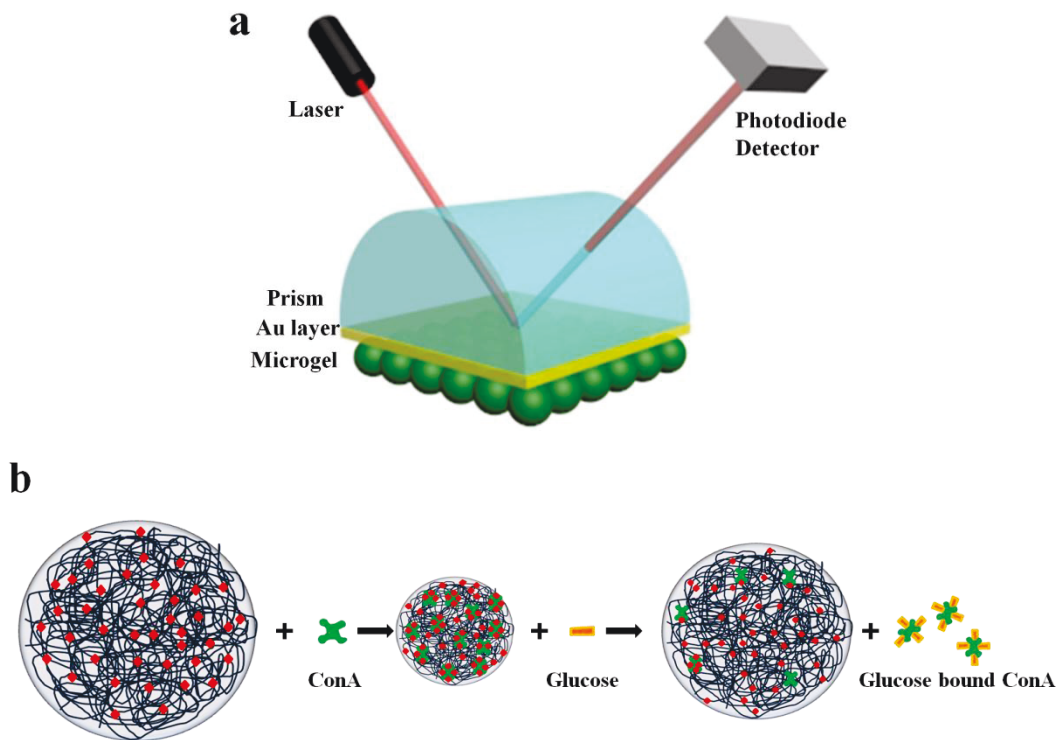
Figure 4-1. a) The surface plasmon resonance spectrometer setup. b) A proposed p(NIPAm-*co*-GEMA) microgel sensing mechanism in glucose detection. The red squares represent the pendent glycosyl group in GEMA, the green crosses represent ConA and the orange rectangles represent the glucose in the solution.

4.2 Experimental Section

4.2.1 Materials

Unless stated otherwise, all reagents and chemicals were purchased from commercial sources and used without further purification. N-isopropylacrylamide (NIPAm) was purchased from TCI (Portland, Oregon) and purified by recrystallization from hexanes (ACS reagent grade, EMD, Gibbstown, NJ) before use. Glycosyloxyethyl methacrylate solution (5% W/V in ethanol, Sigma Aldrich) was concentrated by removing the ethanol with a rotovap (IKA RV8, Wilmington, NC),

resulting in a pale green viscous fluid. N, N'-methylenebisacrylamide (BIS) (99%), ammonium persulfate (APS) (>98%), Trizma base (>99%), α-D-glucose, D-(+)-galactose, sucrose, Concanavalin A (ConA), erythrina crystagalli (Ery) and Bovine serum albumin (BSA) were purchased from Sigma Aldrich. Calcium chloride (anhydrous $CaCl_2$) was purchased from Fisher Chemical (Fair Lawn, New Jersey). Manganese chloride tetrahydrate ($MnCl_2 \cdot 4H_2O$) was purchased from Matheson Coleman & Bell (Norwood, Ohio). Hydrochloric acid (HCl) was purchased from Caledon (Georgetown, Ontario). Anhydrous ethanol (Brampton, Ontario) was processed by adding 3 Å molecular sieve to remove trace amounts of water. All deionized water (DI H_2O) was obtained from Milli-Q Plus system from Millipore (Billerica, MA) with a resistivity of 18 MΩ·cm. Glass cover slips were purchased from Fisher Scientific (Ottawa, Ontario). Chromium (99.999%) was purchased from ESPI (Ashland, OR) and Gold (99.99%) from MRCS Canada (Edmonton, AB, Canada).

4.2.2 Microgel Synthesis

Microgel particles were synthesized via surfactant free, free radical precipitation polymerization. The monomer mixture, with a total concentration of 112.2 mM, was composed of 78% (mol %) N-isopropylacrylamide (NIPAM), 21% glycosyloxyethyl methacrylate (GEMA) and 1% N,N'-methylenebisacrylamide (BIS) crosslinker. Briefly, NIPAm (0.88 mmol) and BIS (0.11 mmol) were dissolved in 10 mL of DI H_2O and filtered through a 0.2 μm filter into a 50-mL, 3-neck round-bottom flask. Additionally, the reaction vessel was equipped with a reflux condenser and a temperature probe. The mixtures were degassed with dry N_2 and heated to 65 ℃ for about 1 h. Next, GEMA (0.23 mmol) was dissolved in 500 μL anhydrous ethanol, added to the solution in an aliquot and allowed to stabilize for 5 min before adding APS (0.078M, 500 μL) solution. The mixtures were allowed to react at 65 ℃ for 4 h under a N_2 environment. The pale

yellow clear solution became turbid within the first 15 min after initiating the reaction. The dispersions were allowed to cool down to room temperature and filtered through glass wool to remove all large aggregates. The microgel solution was cleaned by repeated centrifugation at ~10,000 rpm for 30 min (X 6). The resultant is a concentrated pale yellow pellet.

4.2.3 p(NIPAm-*co*-GEMA) Film Modified SPR Sensor Chip

The glass cover slips were washed with copious DI H_2O, 95% ethanol, more DI H_2O and dried with flowing N_2 gas. The clean glass chip first was coated with 2 nm Cr and then with 50 nm Au using a Torr International Inc. (New Windsor, NY) thermal evaporation system under a pressure of 10^{-6} torr. The microgel film was generated using a previously described "paint-on" technique.[104] Briefly, an aliquot of 40 μL p(NIPAm-*co*-GEMA) microgel solution was deposited on an Au coated substrate and spread toward each edge using the side of a micropipette tip. The film was rotated 90° to spread the microgel solution to fully cover the slides. The painting procedure was processed on a hot plate at 30 ℃. When the temperature was increased to 35 ℃, the microgel solution on the Au substrate was allowed to dry for 2 h. The excess amount of microgels was removed by washing the surface with a large amount of DI H_2O and further soaking in DI H_2O for overnight.

4.2.4 Tris-HCl Buffer Preparation

A 0.1 M pH 7.5 Tris-HCl buffer solution was prepared by dissolving 12.144 g Trizma base in 990 mL DI H_2O in a 2-L beaker. After adjusting the pH of the solution to 7.5 by adding a concentrated HCl solution, 0.1979 g $MnCl_2 \cdot 4H_2O$ and 0.1110 g $CaCl_2$ were added to the mixture; the final volume of the solution was adjusted to 1 L in a volumetric flask. Different

concentrations of ConA were prepared with the 0.1M pH 7.5 Tris-HCl buffer. All the protein solutions (1 mg/mL BSA, 1 mg/mL Ery and 2 mg/mL BSA/ConA mixtures) were prepared with the pH 7.5 Tris-HCl buffer.

4.2.5 Microgel and Microgel Film Characterization

The chemical composition of the microgels was confirmed by nuclear magnetic resonance (NMR) spectroscopy (Agilent/Varian Inova two-channel 400 MHz). The transmission electron microscope (TEM) images of the microgel particles were acquired using a JEOL, JEM 2100 (JEOL USA, Inc., MA, USA) with an accelerating voltage of 200 kV, and the images were analyzed further by the Image-J software. The specimens were prepared by adding 10 µL of highly diluted microgel solutions onto the carbon coated copper grids and air-dried overnight. The hydrodynamic diameter of the p(NIPAm-*co*-GEMA) microgel particles was measured by photon correlation spectroscopy (PCS) (Brookhaven Instruments ZetaPlus zeta potential analyzer, Holtsville, NY) as a function of temperature from 25 °C to 60 °C in 5 degree increments. All the measurements were taken in DI water with an average of ten 30 s acquisitions and an average of three measurements per sample at each temperature. The surface morphology of the microgel modified SPR sensor chip (before and after soaking in ConA solution) was characterized by atomic force microscope (AFM) (Digital Instrument, Dimension 3100) in air. The images were acquired in a 10×10-µm area using a scan rate of 0.5 Hz and 512 scan points and lines in the tapping mode. The p(NIPAm-*co*-GEMA) microgels coated SPR sensor surface was soaked in 1 mg/mL ConA for 45 min, rinsed with pH 7.5 Tris-buffer and dried by blowing with N_2 before imaging. The glucose responsiveness of the p(NIPAm-*co*-GEMA)-ConA film was monitored by measuring the film thickness change in liquid by an AFM (Asylum Research MFP 3D AFM,

Santa Barbara, CA) and the reflectance changes by a surface plasmon resonance (SPR) spectrometer. The SPR spectrometer is a custom-built instrument equipped with a 632.8 nm HeNe laser (1.5 mW, R-32734, Newport) and a photodiode detector (918D-SL-OD3, Newport) with a scanning range of 25.000° to 90.000° and a resolution of 0.001°. The 50 nm Au sensor chip was coupled to the back of a BK7 hemicylindrical prism with a refractive index of 1.51. The motion of the rotation stages were controlled by a XPS C-8 controller (Newport) with a self-developed LabVIEW program. In addition, the position of the rotation stages and the readout of the photodiode detector were recorded synchronically with a self-developed LabVIEW program. The setup is shown in Figure 4-1a. The SPR instrument was calibrated by a series of sucrose solutions with different concentrations. The calibrated curve of the RA as a function of RI is shown in Figure 4-2.

Equation	y = a + b*x	
Weight	Instrumental	
Residual Sum of Squares	8.98373	
Pearson's r	0.99919	
Adj. R-Square	0.99757	
	Value	Standard Error
B Intercept	-89.50025	4.72468
B Slope	124.05805	3.53535
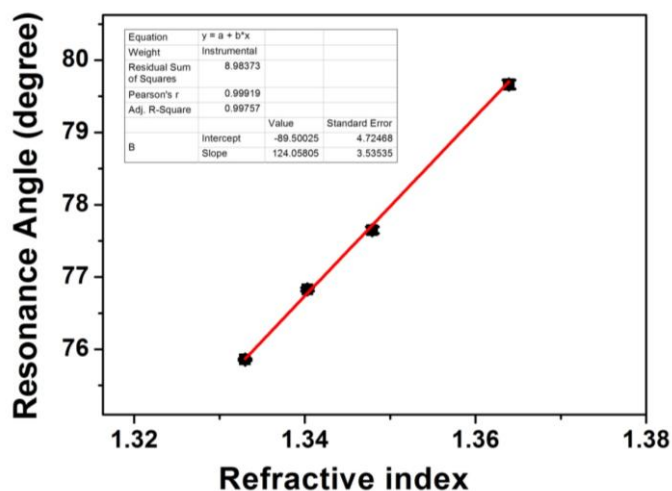
Figure 4-2. The calibration curve of a custom-built SPR spectrometer. Different concentrations of sucrose solution were prepared and their refractive index at different concentration was cited from the reference.[129] The RA at each concentration was determined and plotted as a function of refractive index. Each point represents the average of three different measurements, and the error

bars represent their standard deviation. The red line is the best fit with a slope of 124.058 degree/RIU, an intercept of -89.500 degree and a R^2 of 0.997.

4.3 Results and Discussion

4.3.1 p(NIPAm-*co*-GEMA) Microgel Characterization

First, the successful incorporation of GEMA comonomer to the microgel particles was confirmed by investigating the microgels chemical composition via ^{1}H NMR, as shown in Figure 4-3. By comparing the ^{1}H NMR spectrum of GEMA, pNIPAm and p(NIPAm-*co*-GEMA), the peak with a chemical shift of 3.5–4.5 can be ascribed to the existence of the pendent glycosyl group in GEMA of the p(NIPAm-*co*-GEMA) microgel. It proves that the GEMA has been successfully incorporated in the microgels. The morphology of resultant p(NIPAm-*co*-GEMA) microgels was investigated by TEM with a representative image shown in Figure 4-4. As can be seen, the microgels have a spherical morphology, although some of the features in Figure 4-4 seem oblong; this could be the result of two microgels coming together on the TEM grid. The measured diameter of the spherical features in the TEM image reveals an average dry diameter of 511 ± 9.6 nm (n=19). Next, the thermoresponsivity of the microgels was characterized with PCS, as shown in Figure 4-5. As can be seen, the hydrodynamic diameter of the particles decreases as the solution temperature was changed from 25 ℃ to 60 ℃, where ~1 μm diameter size changes can be observed as the microgel undergoes a fully swollen–collapsed state transition. In addition, a volume phase transition temperature (VPTT) of ~32 ℃ could be predicted for the p(NIPAm-*co*-GEMA) microgels from Figure 4-5. As can be seen, the presence of glycopolymer does not significantly affect the VPTT of the pNIPAm microgel.
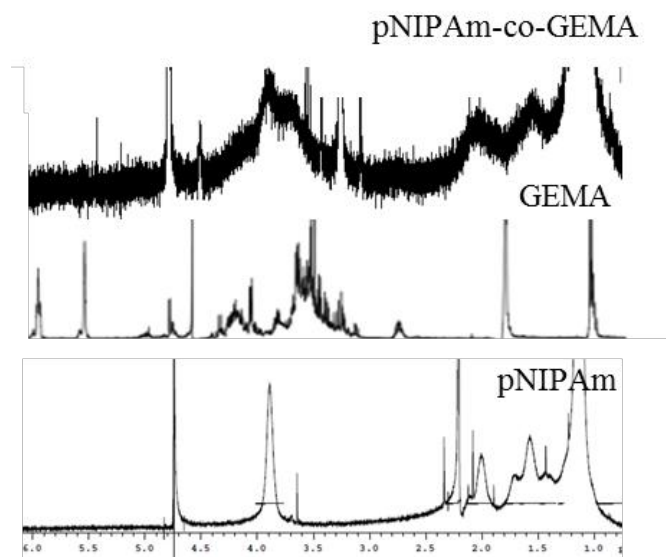
Figure 4-3. The ^{1}H NMR spectra of p(NIPAm-*co*-GEMA), GEMA and pNIPAm, respectively.
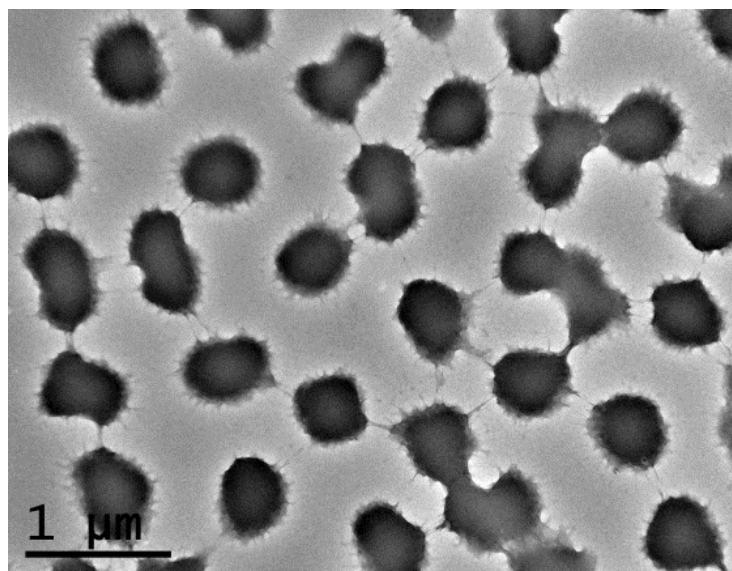
Figure 4-4. A TEM image of the p(NIPAm-*co*-GEMA) microgels.
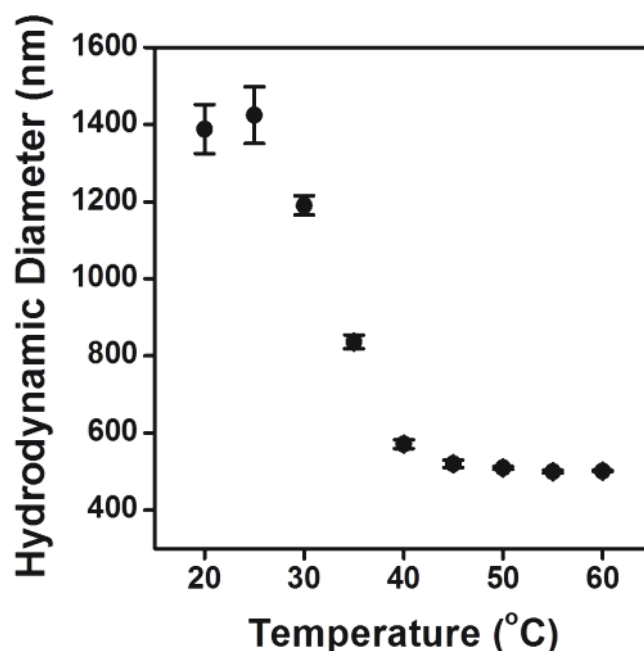
Figure 4-5. The p(NIPAm-*co*-GEMA) microgels particle sizes were measured by PCS as a function of temperature. The error bars represent the standard deviation of three measurements at each temperature.

4.3.2 The Binding Interaction between ConA and a p(NIPAm-*co*-GEMA) Constructed Microgel Film

ConA is a tetramer that reserves four binding sites for specific monosaccharides, such as glucose and mannose. It has been reported that the pendent glycol group in GEMA can specifically bind to one of the four binding pockets of ConA.[128] The interaction between ConA and GEMA from the polymer networks was probed morphologically and optically by using an AFM and a SPR spectrometer, respectively.

Morphologically, the AFM images of the p(NIPAm-*co*-GEMA) microgel coated SPR sensor surface were acquired before and after soaking in 1 mg/mL ConA solution, as shown in

97

Figure 4-6a and 4-6c, respectively. In Figure 4-6a, closely packed colloidal particles were observed with an average roughness of 10.9 nm over a scanning area of 100 μm^2 before exposing them to ConA. However, the particles are contracted when the interparticle distance increased and the bottom substrate was exposed after soaking in ConA, as shown in Figure 4-6c. Such changes were even more noticeable in a 3D demonstration, as shown in Figure 4-6b and 4-6d, where the flat p(NIPAm-*co*-GEMA) microgel film (Figure 4-6b) became more curved (Figure 4-6d) after incubation in the ConA solution. It was hypothesized that such a microgel contraction is a result of the polymer networks further crosslinked by GEMA and the multivalent binding site in ConA. As a control, the surface morphology of the pNIPAm microgel (without the co-monomer GEMA) coated SPR sensor surface also was characterized before and after soaking in the same concentration of ConA; no obvious changes can be seen from the AFM images, as shown in Figure 4-7.
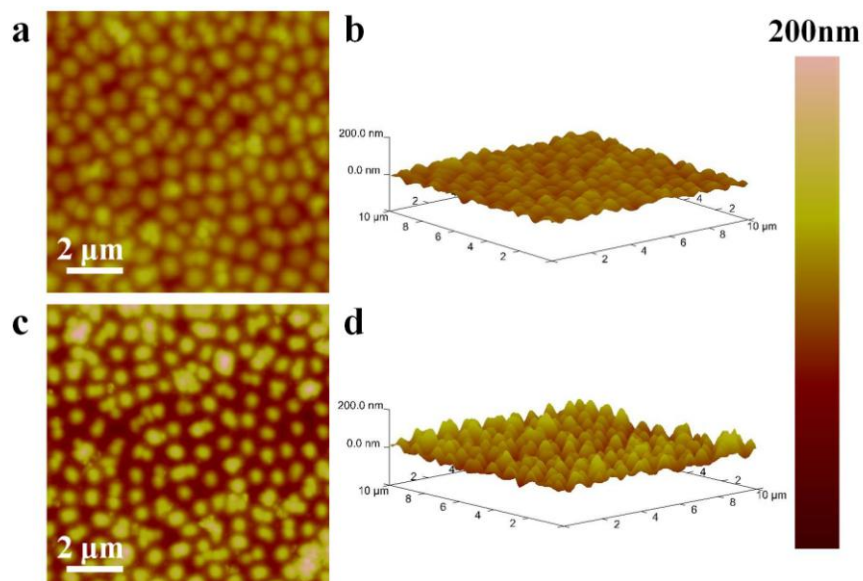
Figure 4-6. The AFM images of the p(NIPAm-*co*-GEMA) film a) before and c) after soaking in 1 mg/mL ConA. Images b) and d) are a 3D demonstration of the image a) and c), respectively.
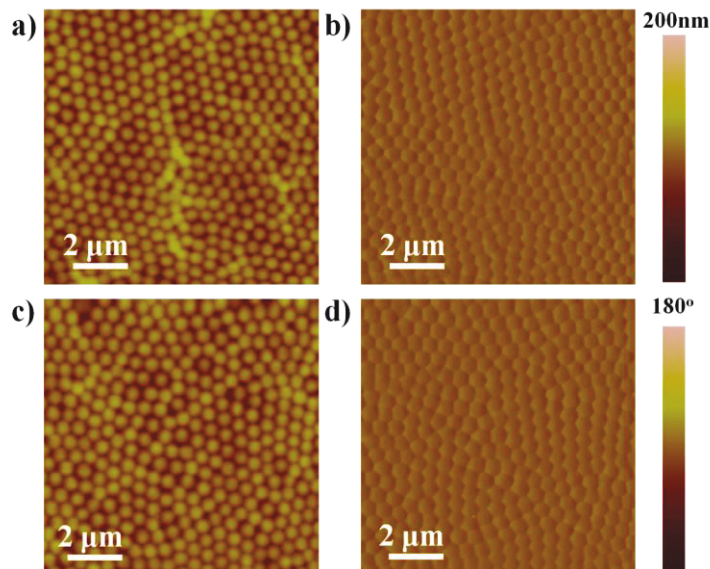
Figure 4-7. The AFM images of a pNIPAm microgels constructed film before a), b) and after c), d) soaking in 1 mg/mL ConA. Images a) and c) are the height profile; b) and d) are the phase profile.

Optically, the interactions between ConA and the p(NIPAm-*co*-GEMA) polymer film were investigated via the custom-built SPR spectrometer described in Chapter 2. The SPR spectra of the p(NIPAm-*co*-GEMA) microgel modified sensor surface were scanned before and after adding different concentrations of ConA. The results are shown in Figure 4-8a. The RA and the reflected light intensity at the RA shifted to a higher value as the ConA concentration increases. The SPR spectra red shift (RA increase) after ConA addition is a result of local RI increases, which may be due to complex reasons. Firstly, the RI of the bulk solvent increased intrinsically as more ConA was added into the same volume of solution. Secondly, such a RI increase possibly can be attributed to the polymer shrinkage as the pendent glycosyl groups in the p(NIPAm-*co*-GEMA) polymer networks were crosslinked by ConA, as was observed in the AFM images in Figure 4-6c.
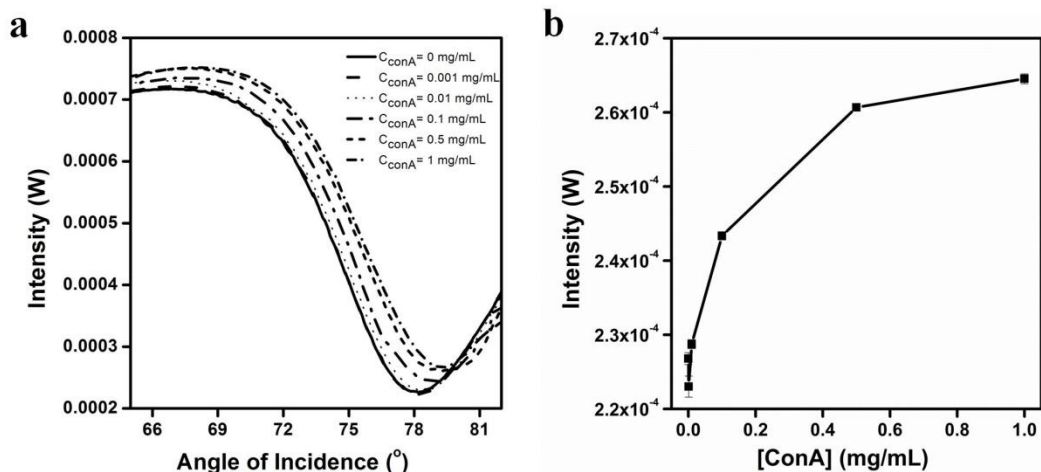
Figure 4-8. a) SPR spectra of the p(NIPAm-*co*-GEMA) microgels modified sensor chip in pH 7.5 Tris-HCl buffer and different concentrations of ConA. b) The reflectance at the RA plotted as a function of the ConA concentration.

To determine the reason for local RI increases, the RA was plotted as a function of the ConA concentration, as shown in Figure 4-9. Based on the calibration curve of RA *vs*. RI (in Figure 4-2) and the RA value at each ConA concentration, one can estimate the RI at each ConA concentration, which is listed in Table 4-1. There is a 87.2×10^{-4} refractive index units (RIU) change when the ConA concentration increased from 0 to 1 mg/mL. However, the intrinsic refractive index increase from such a concentration change is $\sim 1.85 \times 10^{-4}$ RIU, which was calculated by the dn/dc value of ConA with an estimation of ~ 0.185 mL/g.[130] Therefore, it can be concluded that the polymer shrinkage is the main reason for the local RI increase that finally resulted in a SPR spectrum red shift. In addition, the SPR spectra at the high angle region are not smooth, which can be attributed to the surface roughness of the microgel film in the collapsed state (scattering effect).
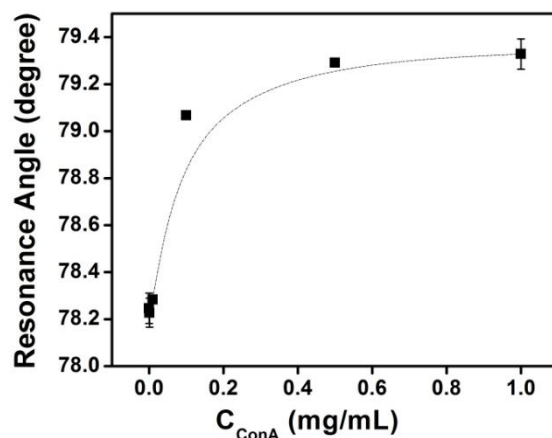
Figure 4-9. The RA of p(NIPAm-*co*-GEMA) film in different concentrations of ConA. The data were derived from Figure 4-8a. The RA at each ConA concentration was determined from SPR spectra by picking the point with the lowest reflected light intensity. Each point represents the average of three different measurements and the error bars represent their standard deviation. The line in the graph is used for guiding.

Table 4-1. The calculated effective refractive index at each RA based on the calibration curve in Figure 4-2.

Concentration of ConA (mg/mL)	Resonance Angle	Refractive Index
0	78.246	1.35216
0.001	78.228	1.35201
0.01	78.284	1.35246
0.1	79.067	1.35878
0.5	79.291	1.36058
1	79.328	1.36088

It should be pointed out that the SPR technique is very sensitive to the immediate vicinity (~λ/2, where λ is the wavelength of incident light) of the Au sensor surface, which is approximately less than ~300 nm in this case. It means that the outermost surface of the microgel (far away from the SPR Au substrate) is not under the electromagnetic field of the SPR

evanescent wave. The effective RI (n_{eff}) in the vicinity of the Au sensor chip can be characterized and estimated by Eq. (41),

$$n_{eff} = \partial_1 n_1 + \partial_2 n_2 + (1 - \partial_1 - \partial_2)n_3 \qquad (41)$$

where n_1 is the RI of the pNIPAm based polymer, normally in the range of 1.51–1.54 in visible light,[131] n_2 is the RI of water (~1.333 at 632.8 nm wavelength), n_3 is the RI of ConA (~1.52),[132] and ∂_1, ∂_2 and $1 - \partial_1 - \partial_2$ are the volume ratio of the polymer chain, water and ConA in a certain space, respectively. When there is no ConA in the solution ($1 - \partial_1 - \partial_2 = 0$), the volume ratio of water, ∂_2, in the polymer networks is estimated to be ~ 90%; this was calculated based on n = 1.35216 (as shown in Table 4-1), n_1= 1.54 and n_2= 1.333. The effective refractive index increased to n = 1.36088 (as shown in Table 4-1) as the concentration of ConA increased to 1 mg/mL, with n_1= 1.54 and n_2= 1.333. It is difficult to estimate the practical ConA occupation percentage in the polymer networks due to several reasons, such as the diffusion-limit (solvent to polymer networks), the number of binding ligand (GEMA) in the polymer networks. Since the refractive index of ConA is very close to that of the polymer, it can be assumed that the volume fraction of the ConA and polymer can be merged as one parameter. Thus, the volume ratio of water, ∂_2, changed to ~ 85%; this was calculated based on n = 1.36088 (as shown in Table 4-1), n_1= 1.54, n_2= 1.333 and n_3 ≈1.54 (should be 1.52). Such a 5% volume decrease of water is a result of polymer networks contraction after the addition of 1 mg/mL ConA and the concomitant change of inner osmotic pressures. To summarize, the effective RI is determined by the RI of the polymers and solvent as well as their occupation percentage in a fixed volume. When the polymer networks contract, the volume ratio of polymer will increase and the overall RI will be closer to that of the polymer. The increased RI was revealed as a RA shifting to a high value in the SPR spectrum.

It is noteworthy that the reflected light intensity was increased as well when more ConA was added to the solution. It was attributed to the higher light scattering efficiency of the ConA induced microgel particles collapse. This can be explained by the Mie theory.[133] The minimum reflected light intensity was plotted as a function of the ConA concentration, as shown in Figure 4-8b. As ConA adding to the solution, the minimum reflected light intensity was increased from 226.8 µW to 264.5 µW as the concentration increased and reached a plateau at a concentration of 1 mg/mL. Therefore, the 1 mg/mL ConA solution was used as the maximum contraction that can be achieved at this concentration. An even higher concentration probably will result in protein aggregation and make the protein lose activity in solution.

It is evident from Figure 4-8a that the SPR curve becomes too broad for an accurate plasmon RA determination when the ConA concentration increases. It would be more practical to measure the reflected light intensity change as a function of time at a fixed angle; despite the occurrence of a reflectance change, it possesses no clear physical meaning in terms of the interfacial dielectric properties. By monitoring the reflected light intensity changes at a fixed angle, a better understanding of the ConA–GEMA interactions in the real-time fashion will be obtained. To achieve this, the SPR spectrum of the p(NIPAm-*co*-GEMA) film in pH 7.5 Tris-HCl buffer was scanned, and the inflection point was determined by the first derivatives of the SPR spectrum. Then, the incident angle was fixed at the inflection point with the reflected light intensity monitored as a function of time, as shown in Figure 4-10. As can be seen, the reflected light intensity increased immediately, with 295 µW changes in 10 min after the addition of 1 mg/mL ConA (arrow 2-3 in Figure 4-10). The nonspecific adsorption of ConA to the polymer film was removed by subsequently running pH 7.5 Tris-HCl buffer through the sensor surface (arrow 3-4 in Figure 4-10). The intensity decrease in the dissociation phase possibly is due to the

following reasons: 1) a bulk refractive index change from ConA/buffer to only buffer; 2) nonspecific adsorption removal; 3) partial dissociation of bound ConA with GEMA. Due to the shorter decay length of the electromagnetic field of the SPR evanescent field, the dissociate responses can be attributed only to the removal of non-specifically bound ConA and the partial dissociation of bound ConA. The reflected light intensity is still much higher than the one before ConA is added to a running buffer, which further proved the successful interaction between ConA and GEMA. To regenerate the p(NIPAm-*co*-GEMA) sensor surface, a high concentration of sucrose (136 mg/mL) in buffer solution was introduced to the fluidic cell followed by running buffer solutions. In Figure 4-10 (arrow 4-6), it can be seen that the reflected light intensity decreased immediately and then increased suddenly, while the intensity finally went back to the initial state (before introducing ConA). Such behavior can be explained by the fact that due to a higher binding affinity toward ConA/sucrose than ConA/GEMA and an extremely high concentration of sucrose, more ConA would be expected to dissociate from the polymer networks, resulting in a rapid reflectance decrease. However, such a high concentration of sucrose also will result in an imbalance between the inner and out osmotic pressure of the polymer film after ConA dissociation, which would be expected to result in polymer collapse and is revealed as an interrupted reflectance increase in the SPR profile. After switching to pH 7.5 Tris-HCl buffer, the reflectance decreased immediately back to where it was before adding ConA, which indicates that all the bound ConA has dissociated from the polymer film.
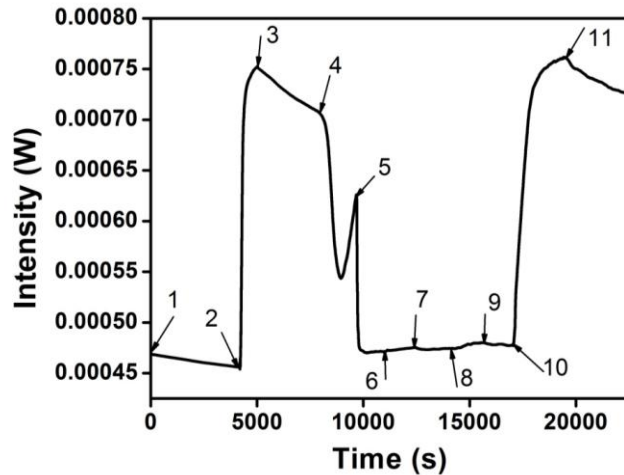
Figure 4-10. Real time SPR data of the p(NIPAm-*co*-GEMA) modified Au sensor surface in different solutions: 1), 3), 5), 7), 9), 11) pH 7.5 Tris-HCl buffer; 2) 1mg/mL ConA in buffer solution; 4) 136 mg/mL sucrose in buffer solution; 6) 1 mg/mL BSA in buffer solution; 8) 1 mg/mL Ery in buffer solution; 10) 1 mg/mL BSA and 1 mg/mL ConA mixture in buffer solution.

To prove that the interaction is from GEMA instead of NIPAm, the microgel without GEMA as co-monomer was synthesized and modified on a SPR sensor surface, and the same procedures were carried out for comparison. The results are shown in Figure 4-11. There is only a ~30 μW intensity change after the addition of 1 mg/mL ConA, which is negligible compared to the ~290 μW increase in the p(NIPAm-*co*-GEMA) modified SPR sensor surface. In comparison to the dissociation phase, more reflected light intensity decrease can be observed in the case of p(NIPAm-*co*-GEMA). However, the total reflected light intensity change of the p(NIPAm-*co*-GEMA) modified film (~250 μW) is still much higher than that of the pNIPAm modified one (~10 μW) after the nonspecific adsorption removal.
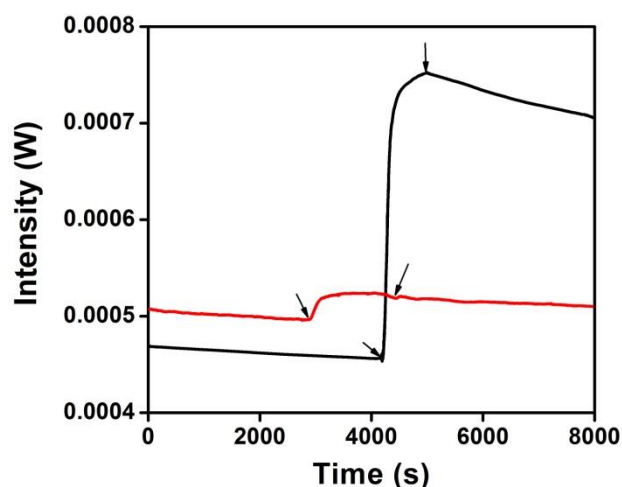
Figure 4-11. A real-time SPR profile of a p(NIPAm-*co*-GEMA) film (black line) and a pNIPAm film (red line) interaction with 1 mg/mL ConA in a pH 7.5 Tris-HCl buffer. The first arrow in each line represents the point where 1 mg/mL ConA was introduced, and the second arrow in each line represents the point where pH 7.5 Tris-HCl buffer was added.

4.3.3 Nonspecific Binding Studies

To make such a glycol-copolymer film as a general transducer in a sensing application, it is desirable that this film should have very few nonspecific interactions and should not be affected by other interferences. To verify that the SPR signal change is due to the specific interaction from ligand and receptor, the following experiments were carried out. First, the regenerated device was exposed to bovine serum albumin (BSA), which was expected not to interact with the GEMA-modified microgels. As apparent in the SPR profile in Figure 4-10 (arrow 6-7), there is a slight reflectance increase after BSA injection, which drops back to the initial baseline after the addition of pH 7.5 Tris-HCl buffer (arrow 7-8). There is only a ~2 μW reflected intensity change, which is negligible in comparison to that from ConA. This proves that such a polymer film does not interact with other proteins.

Furthermore, the same surface was exposed to the erythrina crystagalli (Ery) (lectin), a dimer plant lectin with a molecular weight of 56 KDa, which specifically binds to galactose. No interaction was expected in this case either. As can be seen in Figure 4-10 (arrow 8-9), there was a minimal signal change after the Ery injection and the intensity decreased to the baseline after running a wash buffer. Again, only a ~4 μW reflected light intensity increase was observed between buffer cycles. From the above results, it can be concluded that the p(NIPAm-*co*-GEMA) film neither interacts with other proteins nor has an affinity toward other lectins.

Lastly, the same device was exposed to a 2 mg/mL ConA/BSA (1:1 mass ratio) mixture buffer solution for which a similar response was expected for the case of the 1 mg/mL ConA addition. As can be seen in Figure 4-10 (arrow 10-11), the reflected intensity increased dramatically after the ConA/BSA mixture addition and reached a similar amplitude when only 1 mg/mL ConA (arrow 2-3) was added. The intensity decrease in the dissociation phase is similar to the case of only running ConA. In conclusion, the performance of such a transducer was not affected by other interferences.

4.3.4 Glucose Response Studies

The glucose responsiveness of the conjugated polymer film p(NIPAm-*co*-GEMA)-ConA was investigated further since the specific interactions between ConA and GEMA have been proved. As can be seen in Figure 4-1b, a swelling response with microgel size increases will be expected when exposing the ConA-GEMA microgels to a glucose solution. It was hypothesized that the polymer contraction was released after glucose exposure owing to the higher binding affinity of ConA toward glucose than GEMA. If this happens, one expects to see a decrease in the SPR signal as the biomolecular interactions transfer to a polymer conformation change with a

concomitant refractive index decrease. As a first step, liquid AFM imaging was performed to verify the change in the diameter of the microgels in response to addition of glucose. For this experiment, a microgel sandwich was generated to facilitate the imaging process by first depositing 15 nm Au on a glass substrate, followed by a monolayer of microgels and subsequently a 5 nm Au overlayer. As can be seen, the thickness increased from 1.3 ± 0.1 μm to 1.9 ± 0.2 μm after exposure to glucose, as shown in Figure 4-12. It is important to note that the images were acquired in the same region of the film that was scratched with a razor prior to imaging. With the SPR spectrometer, the p(NIPAm-*co*-GEMA)-ConA film was exposed to a series of glucose concentrations with the reflected intensity recorded, as shown in Figure 4-13. A decreasing trend in the reflected intensity can be observed as the glucose concentration increases. Interestingly, there are two linear ranges in the calibration curve, with 5 mM as the critical point where the sensitivity is lower below this glucose concentration. This was attributed to the competition between GEMA in the polymer networks and free glucose in the solutions for the ConA binding sites. Although glucose has a higher binding affinity toward ConA, the low concentration of glucose made it hard for ConA to dissociate from the glycosyl group of the polymer network, which finally yielded less reflectance changes. For comparison in terms of sensor sensitivity, a bare Au film was exposed to the same series of glucose solutions. The p(NIPAm-*co*-GEMA) film showed a 9-fold enhancement in glucose detection, as seen in Figure 4-13. Lastly, the responsiveness of polymer–ConA conjugate toward other carbohydrates, such as galactose, was also investigated and the result is shown in Figure 4-14. As can be seen, the reflected intensity decrease rates are similar in the buffer and in the galactose/buffer solution (200 mg/dL); this demonstrated the low affinity between ConA and galactose. In the dissociation phase, the reflected intensity decrease is reasonable as the free ConA in the solution was

removed constantly (by running a solution, either buffer or galactose), which resulted in the establishment of a re-equilibrium between ConA in the solution and the polymer network.
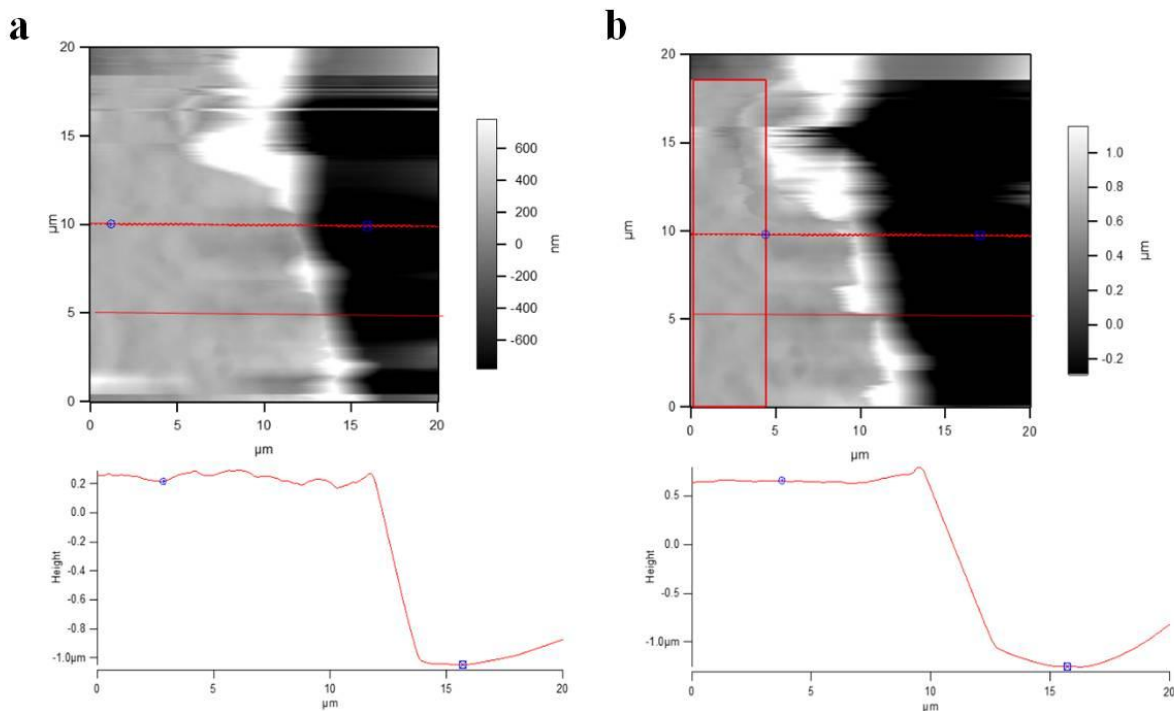
Figure 4-12. In-liquid AFM images of the Au film sandwiched p(NIPAm-*co*-GEMA)-ConA conjugates before and after incubating in the 1mg/mL glucose solution. A line was scratched into the device using a razor blade, and the scratched spot was imaged. Images were taken first in the pH 7.5 Tris-HCl buffer solution at 25 ℃.
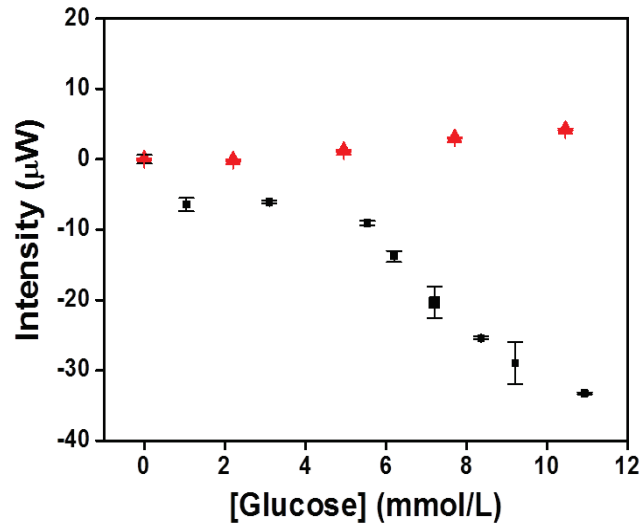
Figure 4-13. Reflectance changes as a function of glucose concentration of the p(NIPAm-*co*-GEMA) polymer film (black squares) and bare Au sensor device (red triangles). Before exposing the p(NIPAm-*co*-GEMA) polymer film to a different concentration of glucose, it was first stabilized in buffer, followed by loading a 1 mg/mL ConA solution and washing with a running buffer to remove the non-specific adsorptions. The buffer was run before and after introducing a different concentration of glucose. The reflected intensity change was obtained by subtracting the intensity between the two buffer cycles. The intensity decrease represented the disassociation of ConA from the GEMA.

110
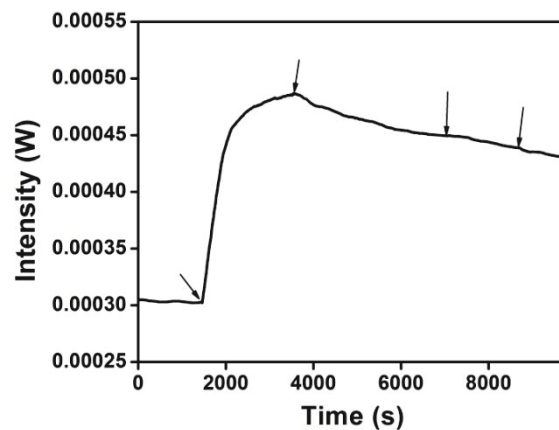
Figure 4-14. A real-time SPR profile of a p(NIPAm-*co*-GEMA) film in different solutions in the order: buffer/ConA/buffer/galactose (200 mg/dL)/buffer. The arrows in the plot represent the point at which a different solution was switched in the fluidic cell.

4.4 Conclusions

In conclusion, the successful synthesis of glucose responsive microgel particles composed of p(NIPAm-*co*-GEMA) was demonstrated. The chemical compositions have been confirmed by ^{1}H NMR. Such synthetic particles also were used to construct a homogenous film with a "paint on" self-assemble technique. The specific interaction between GEMA and ConA was visualized by AFM, showing noticeable surface contractions after soaking in the ConA solution, while no changes occurred in the case of a pNIPAm film. Such specific interactions were further investigated by a real-time SPR spectrometer, with an obvious association and dissociation phase observed in a ConA/buffer and a buffer solution, respectively. The polymer film showed neither any affinity toward other lectins, like Ery, nor other proteins, like BSA. In the presence of other interfering proteins, the polymer film still showed a high binding affinity toward ConA. Finally, the responsiveness of polymer–ConA conjugates toward glucose was first confirmed by a height measurement in liquid AFM and further studied by a custom-built SPR spectrometer. The calibration curve was obtained and showed a 9-fold enhancement compared to the bare Au film. The interaction with other carbohydrates was also investigated, with non-binding affinity observed. In future work, a simple modified polymer film is expected to be coupled to a portable SPR spectrometer and be applied as a disposable POC sensor transducer with a well-designed control channel.

Chapter 5

Microgel Assisted Self-Assembly of Au Nanoparticles for Lithographic Applications

The fabrication and assembly of nanoscale materials and features is the foundation of nanoscience and nanotechnology and the key to generating ever smaller electronic components.[134] Photolithography has been used successfully thus far to produce devices with nanoscale features; however, it is difficult to produce features with a resolution below $\sim\lambda/4$. Here, Au nanoparticle core and poly(N-isopropylacrylamide) shell (Au@pNIPAm) colloidal core-shell particles are generated and their self-assembly is shown to potentially improve on this limitation. First, Au@pNIPAm core-shell colloidal particles were synthesized by free radical emulsion polymerization. The colloidal particles were spread on a substrate using a "paint-on" technique.[104] This procedure resulted in a monolayer of Au@pNIPAm core-shell particles, and after plasma etching, the Au nanoparticle core remained on the substrate. Therefore, an ordered Au nanoparticle array formed by Au nanoparticles could be achieved by using the Au@pNIPAm core-shell particles to template the deposition. The periodicity of the array can be tuned dynamically by controlling the deposition temperature owing to the thermoresponsivity of pNIPAm.

5.1 Introduction

Au nanoparticles (AuNPs) exhibit unique optical properties arising from localized surface plasmon resonance; they have been widely applied in photonic,[135] electronic,[136] catalytic,[137] and other fields. The ordered AuNPs nanostructure (array,[138] pillar,[139] hole[140]) on a solid substrate has attracted great attention due to the synergic effect of these structures. For example, the optical electric filed would be enhanced greatly at the interparticle gap when two nanoparticles are close.[141] The optical spectra can be tuned easily by varying the interparticle distance of nanoparticles.[142] It is critical to generate local regularity at nano scale levels for collective plasmonic properties because of the short-range coupling.[143]

Different approaches have been applied to generate these nanostructures, such as electron-beam lithography (EBL)[144] and focus ion beam lithography (FIB).[145] These techniques provide high resolution and are able to yield features of 1-2 nm with fine control. However, the time consuming serial processes and low throughput limited their application in semiconductor industry. Nanosphere lithography (NSL) has emerged as an alternate approach to fabricate a nanostructure over a large surface area with low-cost and time-saving.[66, 146] Generally, the hard polystyrene (PS) spheres are coated on the substrate and self-assembled into a hexagonal packed structure as the solvent evaporates.[66] Afterwards, Au is deposited on the film by thermal evaporation and fills into the gap created by the PS particles.[66] An ordered triangular Au array can be formed by removing the PS spheres pattern in the desired solvent. However, the interparticle distance can only be varied by the size of the PS particles. In addition, the morphology of the nanostructure generated by this approach is limited. As an alternative method, a smart polymer has emerged as a great candidate to replace the hard sphere PS for surface nanopattern. Smart polymers[147] are macromolecules that undergo chemical or physical property changes on exposure to external stimuli, such as temperature,[148] pH,[149] light,[150] analytes,[151] etc.

Poly(N-isopropylacrylamide) (pNIPAm) is one of the most well-documented thermoresponsive polymers, which exhibits a low critical solution temperature of ~32 °C.[152] The pNIPAm polymer chain can undergo a linear to globular conformation change as the temperature is raised above its LCST.[152] We would like to take advantage of this property to generate a surface pattern with a tunable size just by varying the temperature.

A simple alternative method was applied to produce a 2D Au nano array with a tunable interparticle distance and a variable array size by a microgel assisted self-assembly process. In principle, the Au nanoparticles were isolated by smart polymer encapsulation (Au@pNIPAm core shell particles) and were self-assembled on the substrate as the solvent was evaporating. The interparticle distance was controlled by the polymer layer thickness, which is dependent on the swelling state of the shell and which ultimately is controlled by the annealing temperature. In addition, the nanoparticles array sizes can be varied by overgrowing the Au core over the Au@pNIPAm particles. Finally, the polymer layers were removed by plasma etching without invasion of the Au cores. Thus, a simple and inexpensive method of producing an Au nano array was demonstrated with a tunable interparticle distance and an array dimension that potentially can be applied in surface-enhanced Raman spectroscopy (SERS) or nanosensor devices.

5.2 Experimental Section

5.2.1 Materials

Gold chloride trihydrate (HAuCl$_4$·3H$_2$O) (Aldrich, >99.9%), sodium citrate dehydrate (Aldrich, >99%), sodium dodecyl sulfate (Aldrich, >99%), 3-butenylamine hydrochloride (B-en-A) (Aldrich, >97%), N,N'-methylenebisacrylamide (BIS) (Aldrich, >99%), acrylic acid (AAc)

(>98%), potassium peroxodisulfate (PPS) (Aldrich, > 99%), 95% ethanol (Brampton, Ontario), cetyltrimethylammonium chloride (CTAC) (Aldrich, 25 wt%, H_2O) were used as received. N-isopropylacrylamide (NIPAm) was purchased from TCI (Portland, Oregon) and purified by recrystallization from hexanes (ACS reagent grade, EMD, Gibbstown, NJ) before use. Milli-Q deionized water (DI H_2O) with a resistivity of 18 MΩ·cm was used. Glass cover slips were purchased from Fisher Scientific (Ottawa, Ontario). Chromium (99.999%) was purchased from ESPI (Ashland, OR) and Gold (99.99%) from MRCS Canada (Edmonton, AB, Canada). All glassware was cleaned with aqua regia and thoroughly rinsed with DI H_2O.

5.2.2 AuNPs Synthesis and Functionalization

The AuNPs were synthesized following the well established Turkevich et al. protocol.[153] Briefly, a preheated 25 ml sodium citrate dehydrate solution (1 wt %) was added quickly to 500 mL of 0.5 mM $HAuCl_4$ with vigorous stirring and strong boiling. After reacting for 20 min, the mixture was allowed to cool down to room temperature with slow stirring. The stabilizing of AuNPs was achieved by adding 3 mL of 1 mM SDS solution dropwise and stirring for 20 min. Next, 1.63 mL of B-en-A (1.4mM in ethanol) was added dropwise to the mixture and stirred for another 20 min to generate a hydrophobic surface of AuNPs. The resultant was concentrated by centrifugation at 1065 rcf for 14 h.

5.2.3 Au@pNIPAm Core Shell Particle Synthesis

Core-shell Au@pNIPAm microgel particles were synthesized by seeded precipitation polymerization.[154] The particle size (or shell thickness) was tuned by varying the Au seed concentration. More seeds would generate more nucleation sites, resulting in less monomer

polymerization on each AuNP surface. Experimentally, NIPAm (0.1132g, 1.000 mmol) and BIS (0.0272g, 0.176 mmol) were dissolved in 50 mL DI H$_2$O and filtered through a 0.2 μm filter into a 100-mL, 3-neck round-bottom flask, which was equipped with a reflux condenser and a temperature probe. The mixtures were degassed with N$_2$ and heated to 70 ℃ over 1 h. Next, an AuNPs seed solution ([Au] 0.017M, 50μL/70 μL/100μL/200 μL) was added to the heated solution dropwise and stirred continually for 10 min before adding the initiator PPS (1 mg in 0.5 mL H$_2$O) solution. The red clear solution became turbid within the first 15 min after initiation of the reaction. The mixtures were allowed to react at 70 ℃ for 2 h under a N$_2$ environment. The dispersions were allowed to cool down to room temperature and filtered through glass wool to remove large aggregates. The microgel solution was cleaned by repeated centrifugation at ~10,000 rpm for 30 min (×6). The resultant core shell particles were labeled as shown in Table 5-1.

5.2.4 Au Core Overgrowth

The Au core overgrowth was obtained by reducing HAuCl$_4$ in the presence of Au@pNIPAm-2 microgel particles (70 μL as seed).[155] First, the 2 wt% Au@pNIPAm microgel solution was diluted with the same volume of 100 mM CTAC. Next, a feed solution was prepared containing 0.5 mM HAuCl$_4$ and 4.75 mM CTAC. In a typical synthesis, a 200 μL precursor solution was combined with 8 mL of 2.4 mM CTAC under vigorous stirring in a 20-mL glass vial, followed by the addition of 130 μL of 10 mM freshly prepared ascorbic acid. Next, a 2 mL feed solution was added dropwise to the seed solution under stirring, and the reaction was allowed to proceed for 20 min. The particles were purified by centrifugation at 3740 rcf until the supernatant was colorless, whereupon the supernatant was discarded and the

precipitate was redispersed in water. This process was repeated twice. The final core size of ~40 nm was determined by transmission electron microscopy (TEM). Particles with an overgrowth gold core of ~50 nm, ~60 nm and ~75 nm in diameter were obtained by adding a 5 mL, 15 mL and 30 mL feed solution, respectively, to the precursor particles. The ratio of ascorbic acid/$HAuCl_4$ was kept constant at 1.3 in all overgrowth experiments.

5.2.5 Au@pNIPAm Microgel Particles Assembled Film

The Au@pNIPAm microgels were coated on a 50 nm Au coated glass substrate (1×1 inch) by a "paint-on" technique.[104] Initially, the 50 nm Au coated glass substrate was cleaned with 95% ethanol and DI H_2O and dried with N_2 before use. An aliquot of 40 μL resultant Au@pNIPAm hybridized microgel was dropped onto the pre-cleaned surface and spread toward each edge using the side of a micropipette tip. The film was rotated 90 degrees to spread the microgel solution to fully cover the slides. The painting procedure was processed on a hot plate with controllable temperature. The Au@pNIPAm microgel solution coated substrate was allowed to dry on the hotplate at a fixed temperature for 2 h. The excess amount of microgels was removed by washing the slide with a large amount of DI H_2O and further soaking in DI H_2O overnight.

5.2.6 Au Nano Array

The Au nano array was formed by removing the polymer shell of the self-assembled Au@pNIPAm microgel film by plasma etching. The resultant film was set in a RIE (Oxford NGP 80) plasmon etching chamber at 100W under an O_2 environment. The etching time was

explored to fully remove the polymer shell without invasion to the AuNPs; the AuNPs remained at their original array location.

5.2.7 *UV-vis* Spectroscopy

The absorbance spectra of AuNPs and Au@pNIPAm microgel particles were recorded with an Agilent 8453 *UV-vis* spectrophotometer, equipped with an 89090A temperature controller and a peltier heating device. Measurements were performed at ambient temperature. The absorbance spectrum of the Au@pNIPAm microgel particle solution was measured as a function of temperature from 20 to 60 ℃ in 5 degree increments. The temperature was allowed to stabilize for 5 min before a spectrum was recorded.

5.2.8 Transmission Electron Microscopy

Both AuNPs and Au@pNIPAm microgel particles were characterized with a JEOL TEM instrument (JEM 2100, USA) in terms of particle morphology and size. The specimens were prepared by drying 10 µL solutions of highly diluted samples on carbon coated copper grids.

5.2.9 Photon Correlation Spectroscopy (PCS)

The hydrodynamic radius of Au@pNIPAm microgel particles was measured by PCS (Brookhaven Instruments ZetaPlus zeta potential analyzer, Holtsville, NY) as a function of temperature from 25 to 60 ℃ in 5 degree increments. All the measurements were taken in DI H_2O with an average of ten 30 s acquisitions and an average of three measurements per sample at each temperature.

5.2.10 Atomic Force Microscopy (AFM)

The Au array and Au@pNIPAm microgel film on a 50 nm Au coated glass substrate were imaged by AFM (Digital Instrument, Dimension 3100) in air. The images were acquired using a scan rate of 0.5 Hz and 512 scan points and lines in the tapping mode.

5.2.11 Scanning Electron Microscopy (SEM)

The Au array generated by Au@pNIPAm-5/6/7/8 on a 50 nm Au coated glass substrates were imaged by a Zeiss Sigma FESEM instrument and operated at 5 KV.

Table 5-1. List of Au@pNIPAm microgel particles with different synthetic ratios.

Sample name	AuNPs seed Volume (µL)	NIPAm (mmol)	Au@pNIPAm-2 precursor solution (µL)	Feed solution volume (HAuCl$_4$ + CTAC) (mL)
Au@pNIPAm-1	50	1.000	-	-
Au@pNIPAm-2	70	1.000	-	-
Au@pNIPAm-3	100	1.000	-	-
Au@pNIPAm-4	200	1.000	-	-
Au@pNIPAm-5	-	-	200	2
Au@pNIPAm-6	-	-	200	5
Au@pNIPAm-7	-	-	200	15
Au@pNIPAm-8	-	-	200	30

5.3 Results and discussion

5.3.1 AuNPs Characterization

The AuNPs synthesized following the Turkevich protocol were 14 ± 2.3 nm in diameter, measured by analyzing TEM images with Image J (n=156). As can be seen in Figure 5-1a, most of the AuNPs were of spherical shape. The characteristic LSPR peak in the *UV-vis* spectrum of AuNPs can be observed in Figure 5-1b at 518 nm.
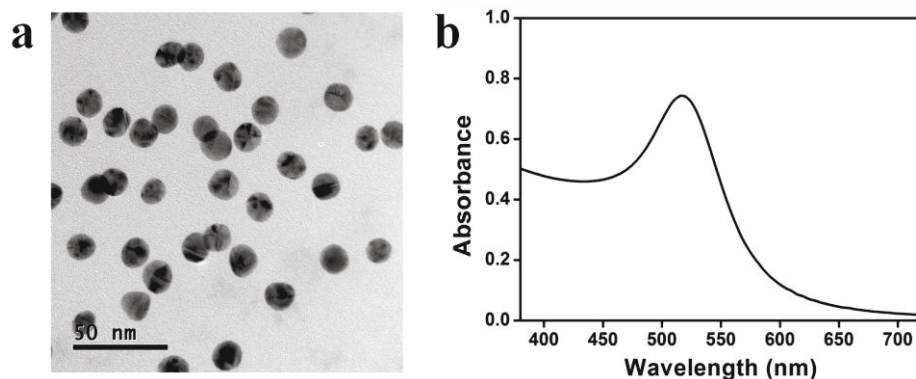
Figure 5-1. a) A TEM image of AuNPs. b) *UV-vis* spectrum of AuNPs dispersion in DI H$_2$O.

5.3.2 Au@pNIPAm Characterization

The Au@pNIPAm microgel particles are the building blocks in Au nano array fabrication, therefore, we would like to expand their versatility by generating different sizes of Au@pNIPAm particles with the same core dimensions. Different shell thicknesses of core-shell particles can be generated simply by tuning the AuNPs seeds to monomer concentration ratios. It was hypothesized that a thinner shell layer will be formed if more AuNPs cores existed in the initial stage of the reaction owing to the multiple nucleation sites. The resultant Au@pNIPAm microgel particles with different seed feeding ratios were characterized by TEM, as shown in Figure 5-2. As can be seen, the AuNPs have been encapsulated successfully by the pNIPAm shell in all cases. However, a few microgel particles were formed without an Au core when the AuNPs seed concentration was too low (50 µL), shown in Figure 5-2a. In addition, the Au@pNIPAm-1 particle size (50 µL) was even smaller than the size of Au@pNIPAm-2 with more AuNPs seeds (70 µL) added in the reaction. It can be explained by the fact that the polymerization occurred on the AuNPs seeds and in the solution at the same time when the AuNPs core concentrations were too low, such as 50 µL in 50 mL mixture solutions. When the

AuNPs seed volume further increased (from 70 µL to 100 µL and 200 µL), the Au@pNIPAm

particles sizes decreased as expected, as shown in Figure 5-2 b/c/d; neither free AuNPs nor two

AuNPs in one microgel were observed in these TEM images. The thermoresponsivity of the

pNIPAm shell of these core-shell particles was investigated further via PCS in terms of the

particle hydrodynamic diameter. The result is shown in Figure 5-3. As can be seen, well-defined

volume phase transitions can be observed at ~32 °C for the Au@pNIPAm particles with different

seed feeding ratios. This means that the presence of the AuNPs core has a negligible effect on the

thermoresponsivity of the shell. Furthermore, the size of the core-shell particles (or the shell

thickness) is smaller as the concentration of the AuNPs seeds in the reaction increases at each

temperature, except for the case with an initial seed volume of 50 µL.
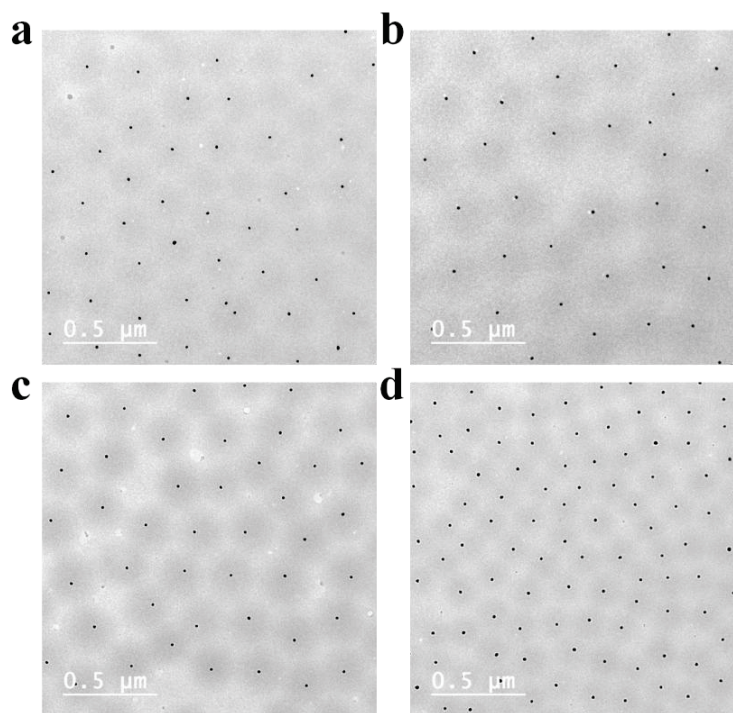
Figure 5-2. TEM images of a) Au@pNIPAm-1 microgel particles, b) Au@pNIPAm-2 microgel

particles, c) Au@pNIPAm-3 microgel particles, d) Au@pNIPAm-4 microgel particles.
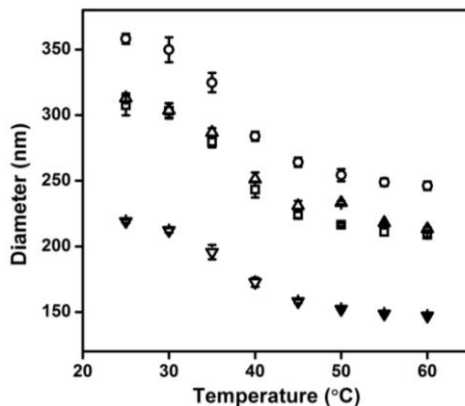
Figure 5-3. Au@pNIPAm microgel particles hydrodynamic diameters measured at different temperature by PCS. The open squares represent Au@pNIPAm-1 microgel particles; the open circles represent Au@pNIPAm-2 microgel particles; the open triangles represent Au@pNIPAm-3 microgel particles; the open inverted triangles represent Au@pNIPAm-4 microgel particles.

5.3.3 Au Core Overgrowth

The Au core size can be tuned further by growing AuNPs on the Au/pNIPAm interface by reducing the $HAuCl_4$ in the presence of Au@pNIPAm-2 microgel particles. The resultant Au core overgrowth particles were characterized by TEM, as shown in Figure 5-4. As can be seen, the Au core increased gradually when more feed solution was added to the same amount of Au@pNIPAm-2 precursor particle solutions. The diameter of the Au cores can be measured by analyzing the TEM images with Image J. The final core sizes were 40±3.9 nm, 49±2.6 nm, 59±4.8 nm and 75±3.8 nm when the volume of feed solution was 2 mL, 5 mL, 15 mL and 30 mL, respectively. It is noteworthy that the shape of the AuNPs core remained the same in the process of overgrowing except for the case of a 5 mL feed solution addition. In the TEM image in Figure 5-4b, irregular shapes of AuNPs were observed, and the color of the Au@pNIPAm-6 solution was purple. This is ascribed to the ratio of the capping agent (CTAC) to the AuNPs cores which affects the faceting tendency and growth kinetics.[156] The resultant core-shell

122

particles were characterized by *UV-vis* spectra at room temperature. The results are shown in Figure 5-5. As can be seen, the characteristic LSPR peaks became noticeable and exhibited a red shift as the Au core diameter increased. However, the LSPR peak of the Au@pNIPAm-6 with a 5 mL feed solution overgrowth showed an even longer wavelength at ~580 nm compared to particles with the largest AuNPs core owing to the irregular shapes of AuNPs.
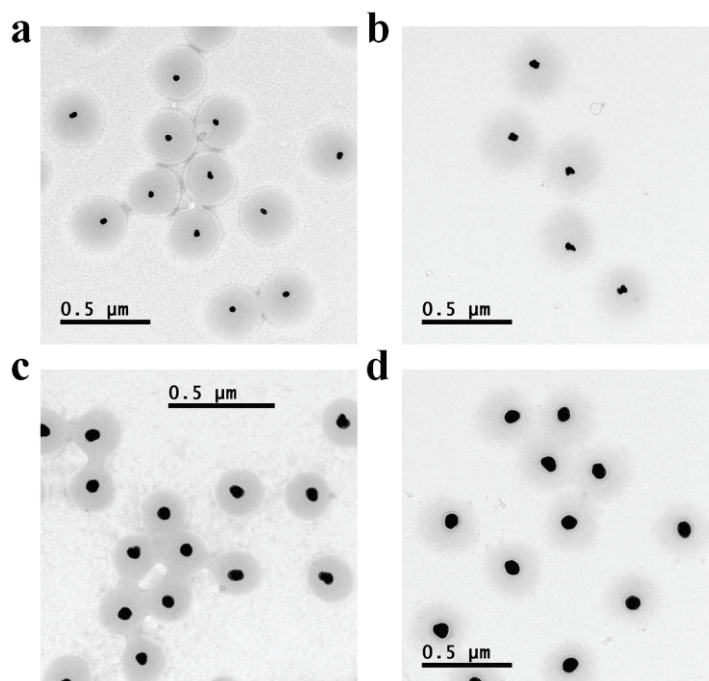
Figure 5-4. a) A TEM image of Au core over growth core-shell particles of Au@pNIPAm-5 with a 2 mL feed solution. b) A TEM image of Au core over growth core-shell particles of Au@pNIPAm-6 with a 5 mL feed solution. c) A TEM image of Au core over growth core-shell particles of Au@pNIPAm-7 with a 15 mL feed solution. d) A TEM image of Au core over growth core-shell particles of Au@pNIPAm-8 with a 30 mL feed solution.
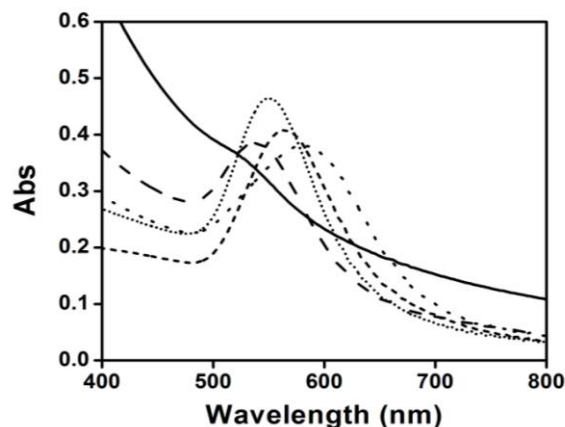
Figure 5-5. *UV-vis* spectra of Au@pNIPAm particles with Au core over growth. The solid line represents spectra of the precursor Au@pNIPAm-2 particles; the dashed line represents the spectrum of the Au@pNIPAm-5 particles with a plasmon peak at 537 nm; the dotted line represents the spectrum of the Au@pNIPAm-6 particles with a plasmon peak at 580 nm; the dash–dot line represents the spectrum of the Au@pNIPAm-7 particles with a plasmon peak at 551 nm; the short–dash line represents the spectrum of the Au@pNIPAm-8 particles with a plasmon peak at 564 nm.

5.3.4 Au Nano Array

With the possibility of a variable shell and core size of Au@pNIPAm microgel particles, Au nano arrays can be generated with different interparticle distances and different array sizes. The resultant Au@pNIPAm-2 microgel film deposited at 25 ℃ was characterized by AFM, as shown in Figure 5-6a. A predominantly hexagonal arrangement of microgel particles can be observed, with no obvious AuNPs core owing to the location of the AuNPs in the hybridized particles buried inside of the microgel particles. Next, the pNIPAm shell was removed by plasmon etching without invasion of the AuNPs cores, expecting the AuNPs cores to remain at the original array spot. To do so, the exposing time of the resultant polymer film was explored

under the same plasma etching conditions, and AFM images of each film were taken after plasma treatment. As can be seen in Figure 5-6b, the AuNPs started to appear after plasmon etching for 10 s as the shell was removed partially. It can be seen that the AuNPs–AuNPs are well separated by the pNIPAm shell, which can be considered as a mechanical spacer. After a 30 s exposure, in Figure 5-6c, all the pNIPAm shell has been removed and only Au cores remain on the surface. The same results can be observed after a 60 s exposure. It is obvious that a 30 s exposure is enough for the complete removal of polymer shells, as shown in Figure 5-6c. Therefore, the AuNPs array can be obtained after exposure of an Au@pNIPAm microgel film under O_2 plasma etching for 30 s with no effect on the array structure of the remaining AuNPs.
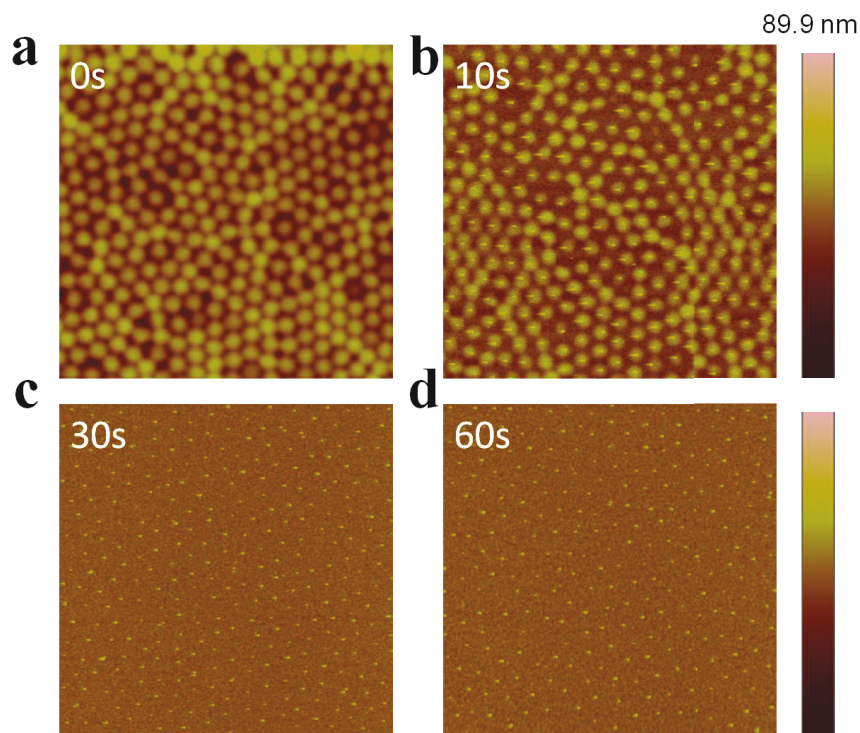
Figure 5-6. AFM images of Au@pNIPAm-2 microgel particles array deposited at 25 ℃ after an exposure time of 0 s (a), 10 s (b), 30 s (c) and 60 s (d) under plasmon etching. All the scan areas are 5×5 μm.

5.3.5 Interparticle Distance Control of Au Nano Arrays

As can be seen from Figure 5-2 and Figure 5-3, the polymer shell thickness can be controlled by two methods: 1) changing the AuNPs seed to monomer ratios in the reaction; 2) tuning the painting temperature owing to the instinct thermoresponsivity of the pNIPAm shell. As a result, it was hypothesized that the Au nano array interparticle distance can be tuned in two different ways. The first approach is to paint different sizes of microgel particles (Au@pNIPAm-2 and Au@pNIPAm-4) on the substrate at the same temperature (20 ℃). The second approach is to paint the same batch of microgel particles at a different temperature (20 ℃ and 60 ℃). The resultant films fabricated under different conditions were characterized subsequently by AFM after plasmon etching for 30 s. The results are shown in Figure 5-7. The interparticle distance between AuNPs was larger when the Au nano array was generated by comparatively large microgel particles (Au@pNIPAm-2 with a hydrodynamic diameter of 307.5±7.6 nm at 25 ℃) at the same painting temperature, as shown Figure 5-7a. For the Au@pNIPAm-4 resultant array painting at 20 ℃, the AuNPs–AuNPs are closer, with many more particles in the same scanning area, as shown in Figure 5-7b. The interparticle distances at 20 ℃ are ~334±34 nm and ~180±23 nm for Au@pNIPAm-2 and Au@pNIPAm-4 particles generated arrays, respectively, as shown in Figure 5-8. As the deposition temperature increased to 60 ℃, the interparticle distance between AuNPs decreased when the Au nano array was generated by the same batch of core-shell particles, as can be seen by comparing Figure 5-7a and Figure 5-7b to Figure 5-7c and Figure 5-7d. The measured AuNPs–AuNPs interparticle distance is shown in Figure 5-8. As can be seen, the interparticle distances at 60 ℃ decreased to ~253±33 nm and ~169±22 nm for Au@pNIPAm-2 and Au@pNIPAm-4 particles generated array, respectively. Therefore, the interparticle distance can be controlled by either depositing different sizes of microgels at

constant temperature or by painting the same batch of particles at different temperatures. Thus, an Au nanoarray can be generated with a wide dynamic range of interparticle distances.
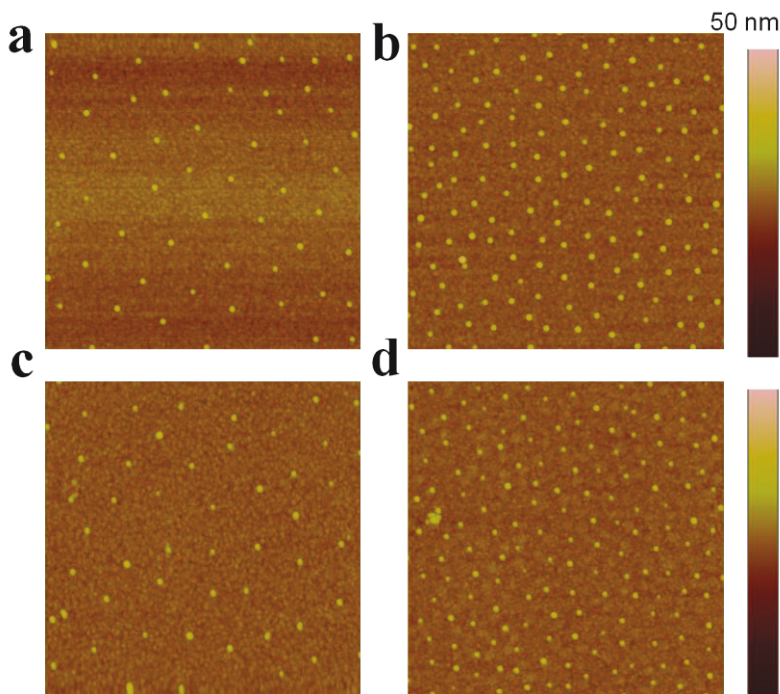
Figure 5-7. AFM images of Au@pNIPAm-2 microgel particles deposited on a 50 nm Au coated glass substrate at 20 ℃ (a) and 60 ℃ (c). AFM images of Au@pNIPAm-4 microgel particles deposited on a 50 nm Au coated glass substrate at 20 ℃ (b) and 60 ℃ (d). All the scan areas are 2×2 μm.

5.3.6 Au Nano Array Size Control

The versatility of this paint-on technique also allows one to control the Au nano array size in addition to the interparticle distance. The Au over growth core-shell particles were deposited on a cleaned substrate at 25 °C and the shell was removed by plasma etching. The resultant film was characterized further by SEM, as shown in Figure 5-9. A predominantly hexagonal structure of Au nano arrays can be observed with the Au core size increasing. The

interparticle distance was slightly different as the core size increased. It can be explained by that fact that the shell shrank as the AuNPs cores further grew in sizes. As can be seen from the TEM images in Figure 5-4, the core shell particles became smaller as the Au core increased even though they originated from the same precursor particles.
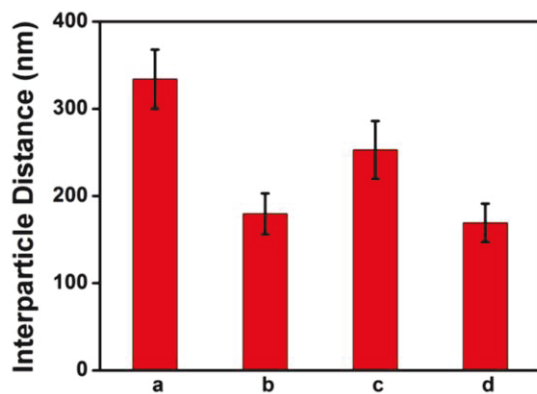
Figure 5-8. AuNPs–AuNPs interparticle distances measured by AFM. The Au nano array was generated by a) Au@pNIPAm-2 microgel particles painted at 20 ℃, b) Au@pNIPAm-4 microgel particles painted at 20 ℃, c) Au@pNIPAm-2 microgel particles painted at 60 ℃, d) Au@pNIPAm-4 microgel particles painted at 60 ℃.
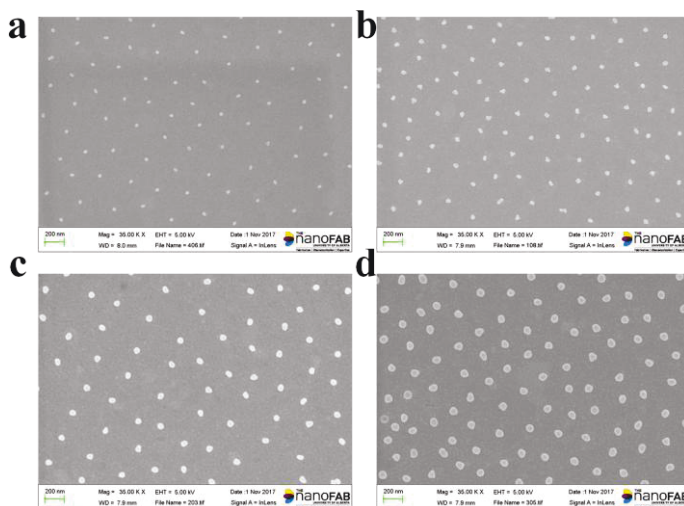
Figure 5-9. SEM images of Au nano arrays generated by (a) Au@pNIPAm-5 microgel particles, (b) Au@pNIPAm-6 microgel particles, (c) Au@pNIPAm-7 microgel particles, (d) Au@pNIPAm-8 microgel particles deposited on a 50 nm Au coated glass substrate at 25 ℃. The scale bar is 200 nm.

5.4 Conclusions

In conclusion, a simple and inexpensive approach to Au nano array fabrication has been demonstrated by "painting-on" Au@pNIPAm microgel particles on a substrate. The Au nano array periodicity can be dynamically tuned by painting different shell sizes of Au@pNIPAm microgel particles or varying the painting temperature. In addition, the Au core sizes are tunable by further growing on the Au@pNIPAm microgel particles. It is expected that such an Au nano array can be applied as a substrate for surface-enhanced Raman spectroscopy or surface plasmon resonance spectroscopy for signal enhancement.

Chapter 6

Au@pNIPAm Core-shell Microgel Based

Optical Device

Au nanoparticle core and poly(N-isopropylacrylamide) shell (Au@pNIPAm) microgels were synthesized by seed mediated free radical polymerization. Subsequently, a one dimensional photonic device was fabricated by sandwiching the resultant Au@pNIPAm particles in between two thin layers of Au film. Such an optical device exhibits visual color and yields a characteristic multipeak reflectance spectrum, where the peak position is primarily determined by the distance between two Au layers. In this Chapter, it was found that the optical properties of the core-shell particle based devices can be tuned by green LED light, and the responsivity is dependent on the exposure time. The optical properties in terms of response kinetics and optical spectrum homogeneity were compared with devices that were fabricated by pNIPAm-based microgels with AuNPs modified by physically adsorption. The uniform Au@pNIPAm microgel based devices showed a fast response and exhibited a comparatively homogenous spectrum over the 1×1 inch slides. Potentially, these materials could be used in drug delivery, active optics, as well as soft robotics.

6.1 Introduction

Gold nanoparticles (AuNPs) have attracted significant attention over the past few decades owing to their unique optical properties caused by what is known as localized surface plasmon resonance (LSPR).[157] LSPR is a phenomenon that allows for light of specific energy to be absorbed. This phenomenon is dependent on the nanoparticles' size, shape and structure, as well as the dielectric constant of the metal and media in contact with them.[158-159] AuNPs of various shapes and sizes have been exploited for a variety of applications, including optical sensing and bio-sensing,[160] gene targeting,[161] drug delivery,[162] stem cell tracking[163] and optical imaging.[164] In addition, the local heat generated by LSPR excitation of AuNPs makes them an excellent candidate for photothermal therapy, which can be used to kill tumor cells non-invasively.[165] In this submission, the photothermal properties of AuNPs were used to generate heat that can trigger the phase transition of the thermoresponsive poly(N-isopropylacrylamide) (pNIPAm); these materials can then be used as light responsive optical devices.

Stimuli-responsive polymers are macromolecules that undergo physical and/or chemical changes in response to changes in their local environment,[35] e.g., temperature,[148, 166] pH,[167] ionic strength,[168] analyte concentrations[169] and light exposure.[170] Ideally, the polymers should return to their initial state once the external stimuli are removed. Of all the stimuli-responsive polymers, temperature responsive pNIPAm is the most well known and well studied.[36b, 166, 171] The conformation of pNIPAm chains in water can transition from a solvated random coil to a relatively desolvated globule as the environmental temperature increases above pNIPAm's lower critical solution temperature (LCST) of ~ 32 °C.[36b] Like linear pNIPAm, crosslinked networks of pNIPAm (hydrogel) and colloidally stable particles (microgels or nanogels) also can be synthesized while retaining their thermoresponsivities. That is, pNIPAm hydrogels, microgels and nanogels swell in water below LCST and collapse above LCST reducing their size and

volume.[172] By introducing additional functional/responsive groups into the polymers at the time of synthesis, other stimuli-responsivities can be engineered into the polymer networks in addition to temperature. Of particular interest to this submission is light responsivity because of the ability to apply the stimulus remotely and the ease of field manipulation (switching on/off, intensity control).[173] There are many examples of light-responsive polymers that are triggered by photochromic molecules that undergo isomerization change upon specific wavelength light illumination, such as azobenzene,[174] spiropyran[174] and diarylethene.[175] Generally, the molecular structure change is accompanied by a local polarity change and even a color change of the photochromic unit. In this submission, AuNP core–pNIPAm shell (Au@pNIPAm) particles were generated through seed mediated free radical polymerization and their light responsivity evaluated. Finally, they were incorporated into optical devices (etalons) to generate colored materials with light stimulated optical properties.

Etalons are optical devices composed of two semi-transparent layers sandwiching a dielectric. The Serpe Group developed etalons composed of responsive polymers that change their optical properties in response to specific stimuli. These devices have been used to generate drug delivery platforms,[176] sensors (pH,[177] temperature,[177a] humidity[178]) and biosensors (specific proteins,[102a] DNA,[169b] small molecules[178]). The structure of the devices is shown schematically in Figure 6-1. A monolayer of pNIPAm-based microgel was sandwiched between two thin layers of Au film supported on a glass substrate. This device exhibits visual color and characteristic reflectance spectra. The characteristics peak can be predicated by Eq. (38),

$$\lambda = 2\,n\,d\,cos\theta/m \qquad\qquad (38)$$

where n is the refractive index of the dielectric medium (microgel layer), d is the distance between two Au layers, θ is the angle of incident light and the integer m is the peak order. Therefore, the microgel size change will be revealed as a peak shift in the reflectance spectrum. It is noteworthy that the mirror–mirror distance dominated the optical properties of etalon; the refractive index change of the microgel layer has a negligible effect on the peak position.
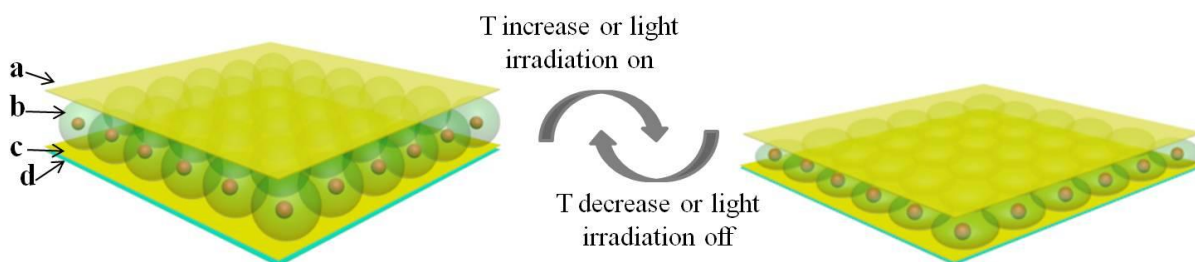
Figure 6-1. A schematic illustration of an Au@pNIPAm microgel based etalon device response to temperature and green LED light. The etalon is constructed by sandwiching the Au@pNIPAm microgel layer (b) between two Au layers (a) (15 nm) and (c) (50 nm) on a glass substrate (d). The red dots represent the AuNPs, and the green spheres represent the pNIPAm microgels. Upon stimulation, temperature increase or green light irradiation, the microgel layers collapsed, resulting in a distance decrease between the two Au layers.

Light responsive optical devices were developed by taking advantage of AuNPs core photothermal properties and pNIPAm shell thermal responsivity. Specifically, the LSPR of AuNPs core can be excited under visible light and subsequently transforms to local heat energy, which induces pNIPAm shell collapse and results in a mirror–mirror distance decrease and a concomitant reflectance spectrum blue shift. In addition, the impact of the AuNPs distribution in a microgel layer was investigated with regard to optical properties in terms of response kinetics

and optical uniformity. In future, AuNPs cores are expected to have a tunable morphology (size or shape) so that they are able to absorb light in the near-infrared (NIR) range and be applied in light triggered drug delivery in vivo. [159]

6.2 Experimental Section

6.2.1 Materials

Gold chloride trihydrate (HAuCl$_4$·3H$_2$O) (Aldrich, > 99.9%), sodium citrate dehydrate (Aldrich, > 99%), sodium dodecyl sulfate (Aldrich, > 99%), 3-butenylamine hydrochloride (B-en-A) (Aldrich, > 97%), N,N'-methylenebisacrylamide (BIS) (Aldrich, > 99%), acrylic acid (AAc) (> 98%), potassium peroxodisulfate (PPS) (Aldrich, > 99%) and 95% ethanol (Brampton, Ontario) were used as received. N-isopropylacrylamide (NIPAm) was purchased from TCI (Portland, Oregon) and purified by recrystallization from hexanes (ACS reagent grade, EMD, Gibbstown, NJ) before use. Branch polyethyleneimine-coated AuNPs (15 nm) were purchased from nanoComposix (San Diego, CA). Milli-Q deionized water (DI H$_2$O) with a resistivity of 18 MΩ·cm was used. Glass microscope slides were purchased from Fisher. Chromium (99.999%) was purchased from ESPI (Ashland, OR) and Gold (99.99%) from MRCS Canada (Edmonton, AB, Canada). All glassware was cleaned with aqua regia and thoroughly rinsed with DI H$_2$O.

6.2.2 AuNPs Synthesis and Functionalization

The AuNPs were synthesized following the well established Turkevich et al. protocol.[153-154] In brief, preheated 25 ml sodium citrate dehydrate solution (1 wt %) was added quickly to 500 mL of 0.5 mM HAuCl$_4$ solution under vigorous stirring and strong boiling. The clear yellow solution became dark red immediately after the addition of sodium citrate dehydrate. After 20

min, the mixture was allowed to cool down to room temperature with slow stirring. To further stabilize the AuNPs, 3 mL of 1 mM SDS solution was added to the AuNPs dispersion and stirred for 20 min. The hydrophobic AuNPs surface was achieved by further modification with 3-butenylamine, 1.63 mL of B-en-A (1.4mM in ethanol), which was added dropwise to the mixture and stirred for another 20 min. The resultant was concentrated by centrifugation at 1065 rcf for 14 h.

6.2.3 Au@pNIPAm Core Shell Particle Synthesis

Core-shell Au@pNIPAm microgel particles were synthesized by seeded precipitation polymerization.[154a] NIPAm (0.2263g, 2.000 mmol) and BIS (0.0544g, 0.353 mmol) were dissolved in 99 mL DI H_2O and filtered through a 0.2 μm filter into a 250-mL, 3-neck round-bottom flask, equipped with a reflux condenser and a temperature probe. The mixtures were degassed with N_2 and heated to 70 ℃ over 1 h. Next, AuNPs seed solution ([Au] 0.017M, 320 μL) was added to the heated solution dropwise and was allowed to stabilize for 10 min before adding initiator PPS (2 mg in 1 mL H_2O) solution. The red clear solution became turbid within the first 15 min after initiator addition. The mixtures were allowed to react at 70 ℃ for 2 h under a N_2 environment. The dispersions were allowed to cool down to room temperature and filtered through glass wool to remove large aggregates. The microgel solution was cleaned by repeated centrifugation at ~10,000 rpm for 30 min (X 6). As a control, the poly(N-isopropylacrylamide) (pNIPAm) and poly(N-isopropylacrylamide-co-acrylic acid) p(NIPAm-co-AAc) microgels were synthesized in a similar fashion without adding AuNPs seeds at the initial stage of the reaction. The p(NIPAm-co-AAc) microgel was composed of 10% mole ratio of AAc.

6.2.4 Etalon Fabrication

Glass coverslips were washed copiously with DI H_2O, 95% ethanol and DI H_2O sequentially, and dried with N_2. A coating of 2 nm Cr (adhesive layer) and 50 nm Au layer were applied on a precleaned glass substrate with a Torr International Inc. (New Windsor, NY) thermal evaporation system (Model THEUPG) under a pressure of 10^{-6} torr. The resultant microgel particles were immobilized on an Au coated glass substrate with the "paint-on" technique.[104] Briefly, an aliquot of 40 μL resultant Au@pNIPAm hybridized microgel was dropped onto the Au coated substrate and spread toward each edge using the side of a micropipette tip. The film was rotated 90 degrees to spread the microgel solution to fully cover the slides. The painting procedure was processed on a hot plate at 30 ℃. When the temperature was increased to 35 ℃, the Au@pNIPAm microgel solution on the Au coated glass substrate was allowed to dry for 2 h. The excess amount of microgels was removed by washing the slip with a large amount of DI H_2O and further soaking in DI H_2O overnight. Additional layers of 2 nm Cr and 15 nm Au films were coated on top of the microgel surface with thermal evaporation. The fabricated device was stored in DI H_2O and dried with N_2 prior to use. As a control, the p(NIPAm-*co*-AAc) based microgels were also painted on the 50 nm Au substrate. The BPEI coated AuNPs were incorporated into the microgel layer by soaking the microgel coated device in a 0.05 mg/mL AuNPs solution for 45 min. Extra AuNPs on the surface were removed by washing the surface with DI H_2O. An additional Au layer (15 nm) was subsequently deposited on top to form a sandwiched structure.

6.2.5 *UV-vis* Spectroscopy

The absorbance spectrum of AuNPs before and after polymerization was recorded with an Agilent 8453 *UV-vis* spectrophotometer, equipped with an 89090A temperature controller and a peltier heating device. Measurements were carried out at ambient temperature. The absorbance spectrum of Au@pNIPAm microgel particle solution as a function of temperature was measured from 20 to 60 ℃ in ten degree increments. The temperature was allowed to stabilize for 5 min before a spectrum was recorded.

6.2.6 Transmission Electron Microscopy (TEM)

Both the AuNPs and Au@pNIPAm microgel particles were characterized with a JEOL TEM instrument (JEM 2100, USA) in terms of particle morphology and size. The specimens were prepared by drying 10 µL solutions of highly diluted samples on carbon coated copper grids.

6.2.7 Photon Correlation Spectroscopy (PCS)

The hydrodynamic radius of Au@pNIPAm microgel particles was measured by PCS (Brookhaven Instruments ZetaPlus zeta potential analyzer, Holtsville, NY) as a function of temperature from 25 to 60 ℃ in 5 degree increments. All the measurements were taken in DI H_2O with an average of ten 30 s acquisitions and an average of three measurements per sample at each temperature.

6.2.8 Atomic Force Microscopy (AFM)

The surface morphology of Au@pNIPAm microgel based etalon devices was characterized by AFM (Digital Instrument, Dimension 3100) in air. Images were acquired in a 10×10 μm^2 area using a scan rate of 0.5 Hz and 512 scan points and lines in tapping mode.

6.2.9 Reflectance Spectroscopy

Reflectance spectra of Au@pNIPAm microgel based etalon devices were collected with a USB2000+ spectrometer, an HL-2000-FHSA tungsten light source and an R400-7-VIS-NIR optical fiber reflectance probe, all from Ocean Optics (Dunedin, FL). The spectra were recorded using Ocean Optics Spectra Suite Spectroscopy Software over a wavelength range of 350–1250 nm. The sample was measured for thermoresponsivity in DI H$_2$O in a temperature controlled chamber fitted with a reflectance probe. The sample and solution temperature were cooled to 0 ℃ and the temperature was increased manually in increments of two degrees up to 70 ℃. The temperature was allowed to stabilize for 5 min at each temperature before a spectrum was recorded. The light responsivity of core-shell microgel based etalon devices was investigated by monitoring the spectrum shift as a function of green LED light irradiation (~517 nm). The sample was immersed in 3 mL DI H$_2$O and fixed in a Petri dish that was positioned ~1 cm on top of LED light source (isolated with foam block). All the spectra were recorded with the LED light off. The control experiment was performed in a similar way with pNIPAm microgel based etalon devices without the AuNPs core.

6.3 Results and Discussion

6.3.1 AuNPs and Au@pNIPAm Synthesis and Characterization

AuNPs were synthesized following the well established Turkevich protocol[153] and characterized by TEM, as shown in Figure 6-2a. The size of AuNPs was 24.9 ± 2.5 nm, measured by analyzing TEM images with Image J (n=1455). Using seed precipitated polymerization, a thermoresponsive pNIPAm shell was coated on the outside of AuNPs. The successful encapsulation of AuNPs can be proved by a TEM image of AuNPs before and after polymerization, as shown in Figure 6-2b. As can be seen, each particle only has one Au nanoparticle core after polymerization; neither free AuNPs nor aggregated AuNPs were observed in the TEM images. Further characterization of the resultant nanocomposites was carried out by *UV-vis* spectroscopy and PCS. In *UV-vis* spectra, shown in Figure 6-2c, the distinct plasmon band diminished and exhibited a red shift from 518 nm to 520 nm after pNIPAm shell modification. It is likely a result of the plasmon damping by the pNIPAm shell of increasing local refractive index around the AuNPs as well as the strong light scattering effect of the microgel layer. When the temperature increased, the absorbance of Au@pNIPAm particles increased both at low wavelengths and at the surface plasmon peak, as shown in Figure 6-2d. Both these effects are likely to arise from microgel collapse at elevated temperatures, which results in more light scattering owing to a high refractive index contrast with the solvent as well as a local refractive index increase on AuNPs. The variation of the absorbance at 400 nm was plotted against temperature, as shown in Figure 6-3, reflected the increase in turbidity of the colloid. In addition, the plasmon band red shift is a result of a local refractive index increase of microgel collapse at elevated temperatures. The size of Au@pNIPAm in the hydrated state is around 279±3 nm at 25 ℃, measured by PCS. The thermoresponsivities of Au@pNIPAm particles were characterized with PCS by measuring the particle hydrodynamic radius as a function of temperature, as shown in Figure 6-4, where a well-defined volume transition is

observed around 32 ℃. The incorporation of AuNPs core did not affect the thermoresponsivity of the pNIPAm shell.
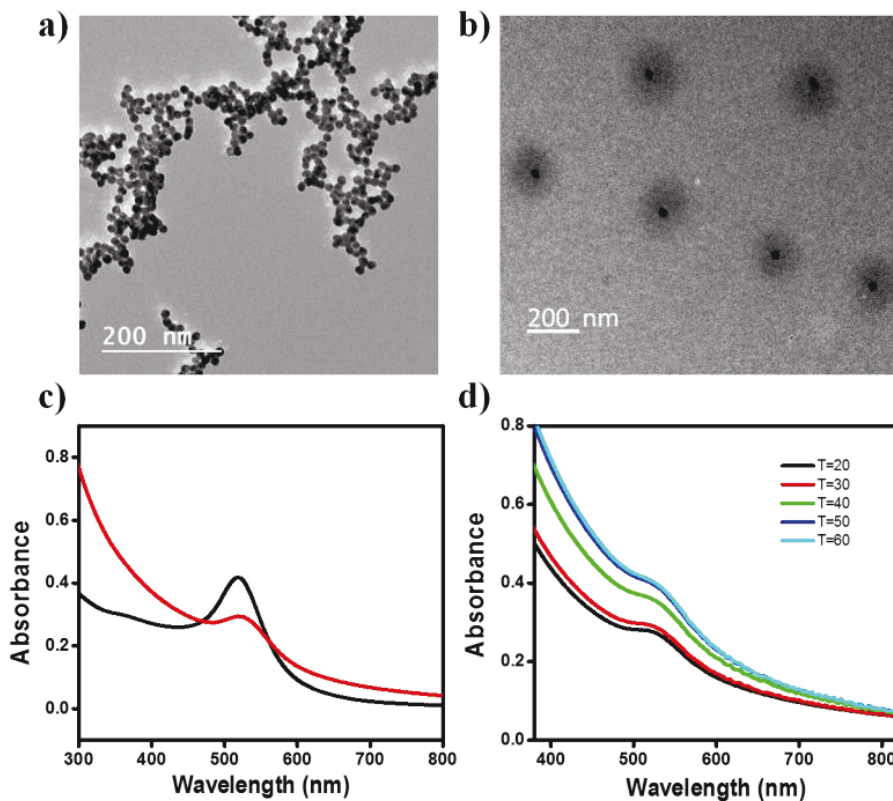
Figure 6-2. TEM images of AuNPs (a) and Au@pNIPAm particles (b). (c) *UV-vis* spectra of AuNPs (black) and Au@pNIPAm nanocomposites (red) dispersions in DI H_2O at 25 ℃. (d) *UV-vis* spectra of Au@pNIPAm nanocomposites dispersions in DI H_2O with temperature increasing from 20 ℃ to 60 ℃.
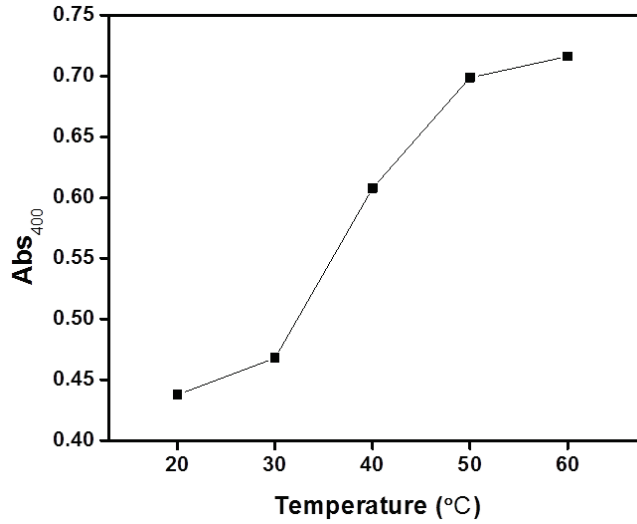
Figure 6-3. The *UV-vis* absorbance of the Au@pNIPAm nanocomposites dispersion in DI H_2O at 400 nm plotted as a function of temperature.
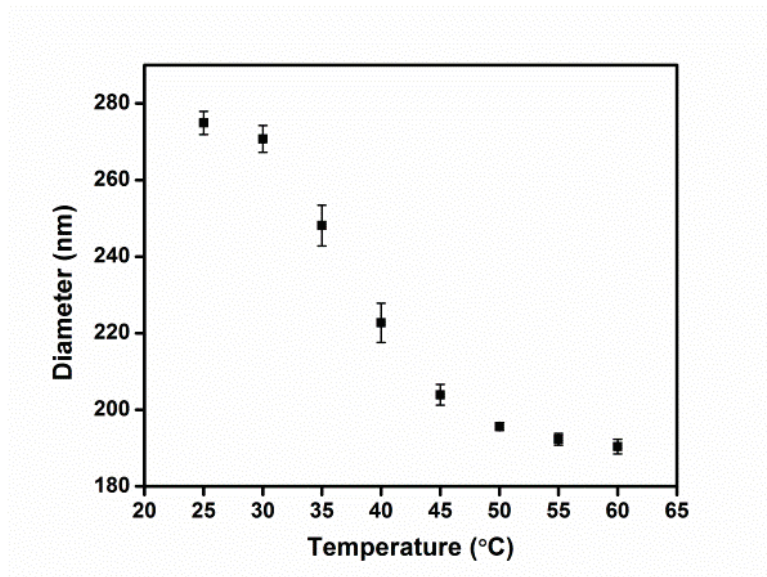
Figure 6-4. The hydrodynamic diameters of Au@pNIPAm particles in DI H_2O measured by PCS as a function of temperature.

6.3.2 Thermoresponsivity of Au@pNIPAm Microgel based Etalon Devices

The core-shell particles obtained were subsequently deposited on an Au coated glass substrate to fabricate optical devices (etalons) following a previously reported "paint-on" technique as detailed in the experimental section. The surface topology of etalon devices was characterized via tapping mode AFM; the result is shown in Figure 6-5. The surface roughness (Rq) of the resultant optical device is 5.40 nm in an area of 100 μm^2. To confirm the basic responsivity and function of the etalons, an initial experiment was focused on characterizing the etalon thermoresponsivity. The reflectance spectrum of an Au@pNIPAm microgel based etalon device in DI H$_2$O is shown in Figure 6-6a. As can be seen, a characteristic peak and trough can be observed at 568 nm and 712 nm, respectively, at 22 °C. In order to determine the spectral shift accurately, the trough position was monitored instead of the peak because it is smoother and narrower. As temperature increased, the trough moved toward lower wavelength. This can be predicted by Eq. (38) since the wavelength is proportional to the distance between two layers of Au, which was determined by the size of the microgels between them. When the temperature is increased, the pNIPAm shell collapses, resulting in two Au mirrors approaching each other, which finally lead to a reflectance spectrum blue shift. The wavelength at the trough was plotted as a function of temperature, as shown in Figure 6-6b. A total ~330 nm blue shift can be observed as the temperature changed from 2 °C to 70 °C. Again, the volume phase transition trend can be observed in Figure 6-6b owing to the thermoresponsivity of the pNIPAm shell. It is of note that the optical properties of the etalons were completely reversible over a number of cycles without an obvious loss in function, as can be seen in Figure 6-7.
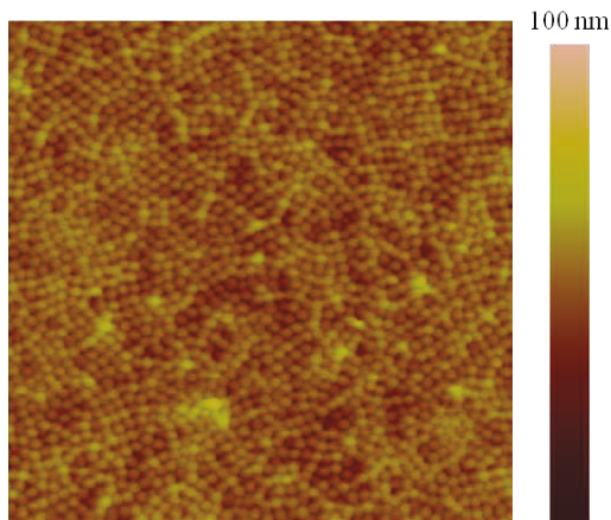
Figure 6-5. An AFM image of an Au@pNIPAm microgel based etalon device in air. The scanning size is 100 μm^2.
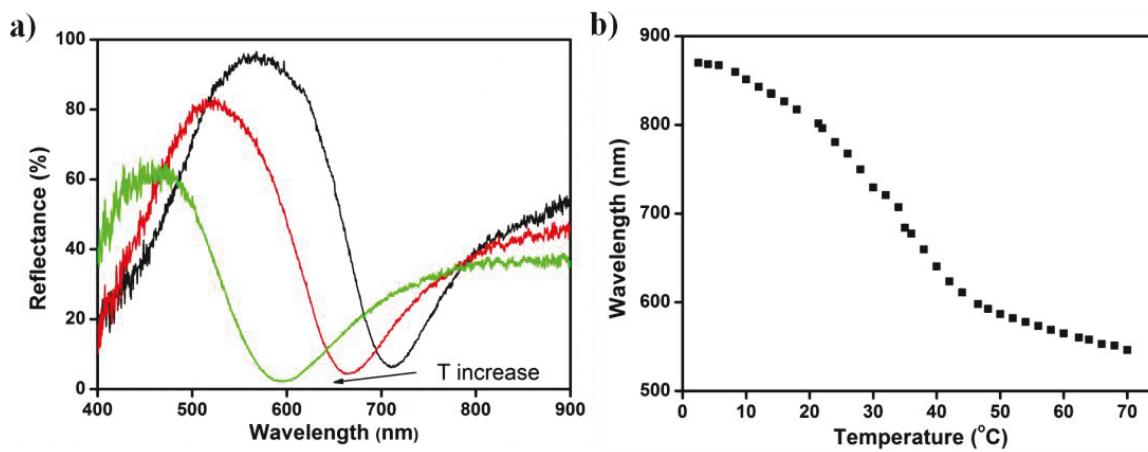
Figure 6-6. a) The reflectance spectrum of an Au@pNIPAm microgel based etalon device in DI H$_2$O at 22 ℃ (black), 30 ℃ (red) and 37 ℃ (green). b) The wavelength of the groove in the reflectance spectrum plotted as a function of temperature from 0 ℃ to 70 ℃ in two degree increments.
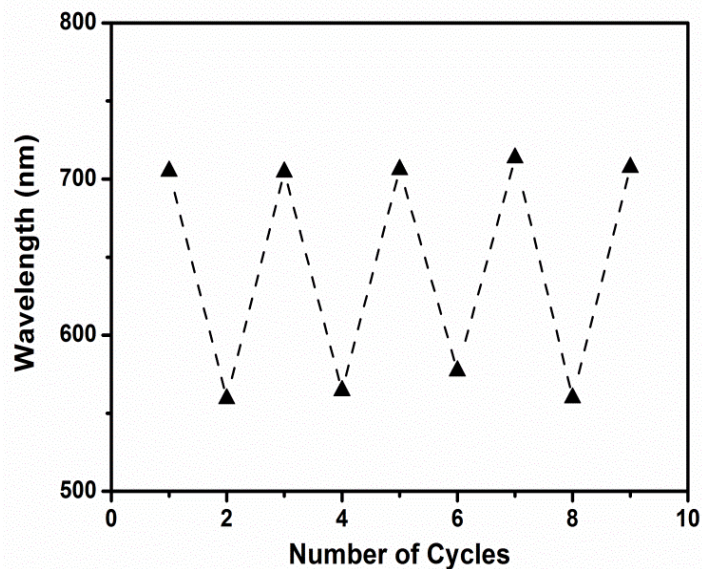
Figure 6-7. The groove wavelength in the reflectance spectrum of the Au@pNIPAm microgel based etalon device at 22 °C (odd numbers) and 40 °C (even numbers).

6.3.3 Light Responsivity of Au@pNIPAm Microgel based Etalon Devices

After investigating the basic thermal response of the Au@pNIPAm microgels based device, the light response of the etalon device was characterized in DI H_2O. During this process, a green LED light was exposed from the bottom of the etalon device. The reflectance spectrum of the device was collected after exposing to LED light every 5 min with the light off, as shown in Figure 6-8a, and the reflectance spectrum shift was plotted as a function of irradiation time, as shown in Figure 6-8b. As can be seen, light illumination caused a ~10 nm spectrum red shift every 5 min of irradiation during the first 15 min. The amount of red shift diminished gradually after 25 min and ceased around 60 min with an accumulated shift of 60 nm. The light response was attributed to the localized surface plasmon resonance generated by AuNPs core followed by a release of heat into the local surrounding environment. It is proposed that the heat generated

from the LSPR effect of AuNPs causes the pNIPAm shell collapse and brings the two Au mirrors close, resulting in a concomitant spectrum blue shift.
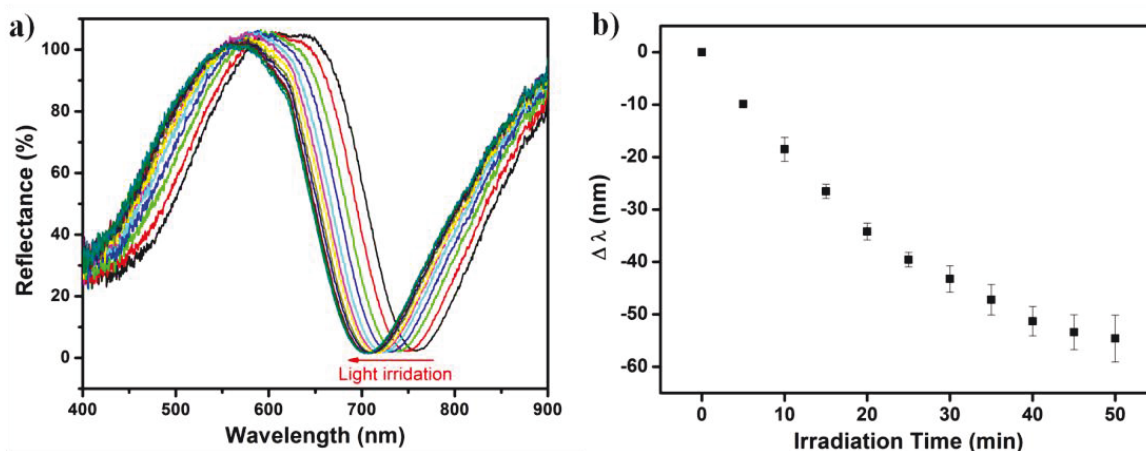
Figure 6-8. a) The reflectance spectrum of an Au@pNIPAm microgel based etalon response to green LED light irradiation. The spectrum was recorded every 5 min. b) The reflectance spectrum shift as a function of irradiation time. Each point represents the average of three independent measurements on a different device from the same batch, and the error bars are the standard deviation for those values.

The light response reversibility of the device was investigated further by monitoring the spectrum shift with the light on/off for several cycles. To accomplish this, the reflectance spectra of each device were collected after continuous light irradiation for 30 min. Then the light source was turned off and the spectrum was recorded after another 30 min; the result is shown in Figure 6-9. As can be seen, a total ~50 nm blue shift can be observed after a 30 min light exposure. With irradiation removal, the reflectance spectra returned to its initial position. The light responsivity of such an optical device did not show too much loss after 5 cycles. To confirm that the observed light-triggered response was a result of the AuNPs core, another etalon device was fabricated with pNIPAm microgel without AuNPs core, following the same procedure. It was

found that illumination of a pNIPAm microgel based etalon device with the green LED light had limited impact on the optical properties, which showed only a ~10 nm blue shift in total after 30 min exposure. It is likely that the Au film of the etalon device absorbs the light energy and releases it as heat. From Figure 6-9, it can be seen that the response of a pNIPAm based etalon device is much smaller than that of an Au@pNIPAm microgel based device. This further proved that AuNPs core in the microgels absorbed green light and dissipated it as heat to induce pNIPAm shell collapse.
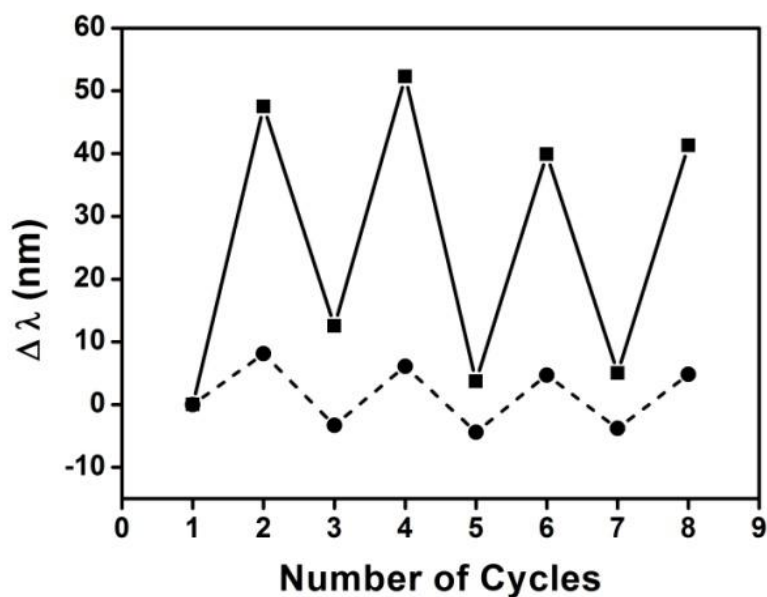
Figure 6-9. The reflectance spectrum blue shift of an Au@pNIPAm microgel (squares) and a pNIPAm microgel (dots) based etalon device as light is on (even numbers) and off (odd numbers) over several cycles.

6.3.4 Light Responsivity Dependence of AuNPs Distribution in Microgel

The impact of AuNPs distribution in the microgel layer was investigated further with respect to light responsivity in terms of optical heterogeneity and responsive kinetics. A previous

article[179] from our group has demonstrated that an AuNPs impregnated etalon device can respond to light irradiation as well. It was shown that the AuNPs were modified in the microgel layer by electrostatic interactions, where the positively charged BPEI-AuNPs were expected to be attracted by negatively charged microgels and be distributed in the polymer networks randomly. However, the Au@pNIPAm core-shell particle based etalon here is constructed with each microgel containing a single AuNP in the center, resulting in a homogenous AuNPs distribution in the microgel layer. Visually, as shown in Figure 6-10, the Au@pNIPAm microgel based etalon gives a uniform color over the whole device, while the AuNPs impregnated microgel etalon device gives a dense color at the outside layer, likely due to a coffee ring effect of AuNPs air-drying. Three spots in each of the devices were randomly selected, and their reflectance spectra were recorded, as shown in Figure 6-11. From the almost overlapped reflectance spectra in Figure 6-11a, it can be concluded that the Au@pNIPAm microgel based device was optically homogenous over the 1×1 inch area. In comparison, an AuNP impregnated microgel etalon device showed significant variation from spot to spot. The AFM image of an Au impregnated microgel device was included in Figure 6-12. By comparing it to the AFM image of Au@pNIPAm microgel based device in Figure 6-5, it is noted that the roughness increased due to the surface adsorption of AuNPs. In addition, the characteristic spherical shape of the microgel particles disappeared. Next, the light responsive kinetics was compared by monitoring the reflectance spectrum shift of three different spots in each device; the results are shown in Figure 6-13. In the initial 15 min, the Au@pNIPAm microgel based etalon devices showed more blue shift under light irradiation than the AuNPs impregnated microgel etalon devices. After irradiation for nearly 30 min, a noticeable spectrum shift started to be observed in the AuNPs impregnated microgel etalon device. The total response is similar though over the course of 60

min illumination in both devices. The fast response of a uniformed core-shell particle based device demonstrated that the energy transfer possibly is due to the particle structure with the energy source (AuNPs core) surrounded by the microgel shell layer. It was hypothesized that the localized surface plasmons of AuNPs are dissipated in a non-irradiative manner as heat which was absorbed by the surrounding microgel layers; this ultimately results in shell collapse. However, in the AuNPs impregnated microgel device, the distance between each AuNPs was unknown because they possibly form AuNPs dimers, trimers or even aggregates. Upon light illumination, the localized surface plasmon resonance of AuNPs would be similar while the energy transfer probably happened between nanoparticles instead of AuNPs and microgels directly. Since the total response is similar after 50 min irradiation, it can be assumed that all the energy finally dissipates into heat and transfers to the surroundings, resulting in microgel collapse. Furthermore, the consistent light response from three different spots in an Au@pNIPAm microgel based etalon device proved the optical homogeneity. The obvious response variation from spot to spot in an AuNPs impregnated microgel device demonstrated the uneven distribution of AuNPs in the microgel, which lead to non-uniform local heating and resulted in a different behavior of the surrounding microgels. The mechanism of this photothermal induced polymer conformation change should be looked at in detail by probing the micro phase behavior of polymers at the metal/polymer interface to elucidate the energy transfer and light/metal interactions.
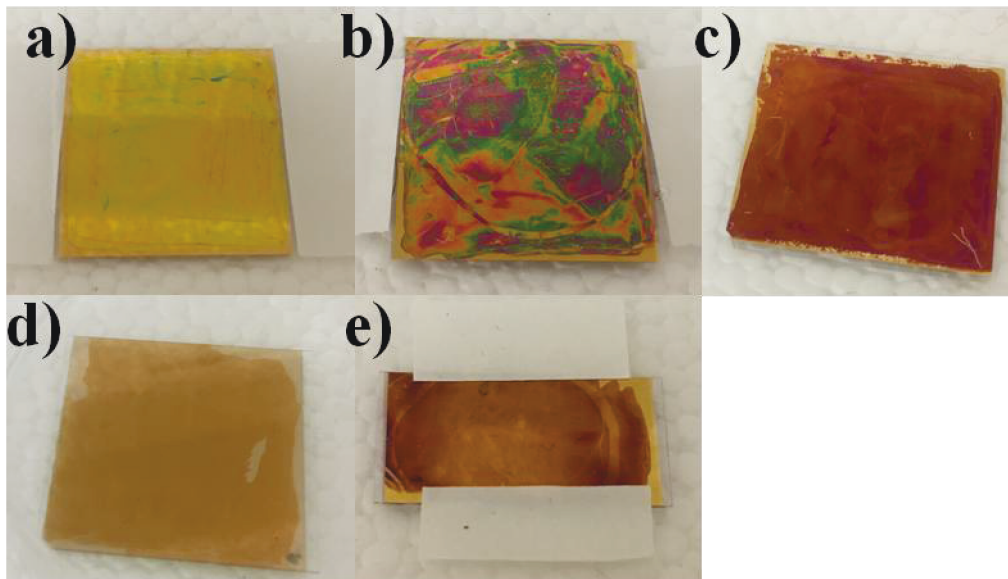
Figure 6-10. Photographs of different microgel based etalon devices in DI H$_2$O (a-c) and air (d-e). (a) and (d) are an Au@pNIPAm microgel based etalon device; (b) and (e) are an Au impregnated microgel based etalon device; (c) is a pNIPAm microgel based etalon device.
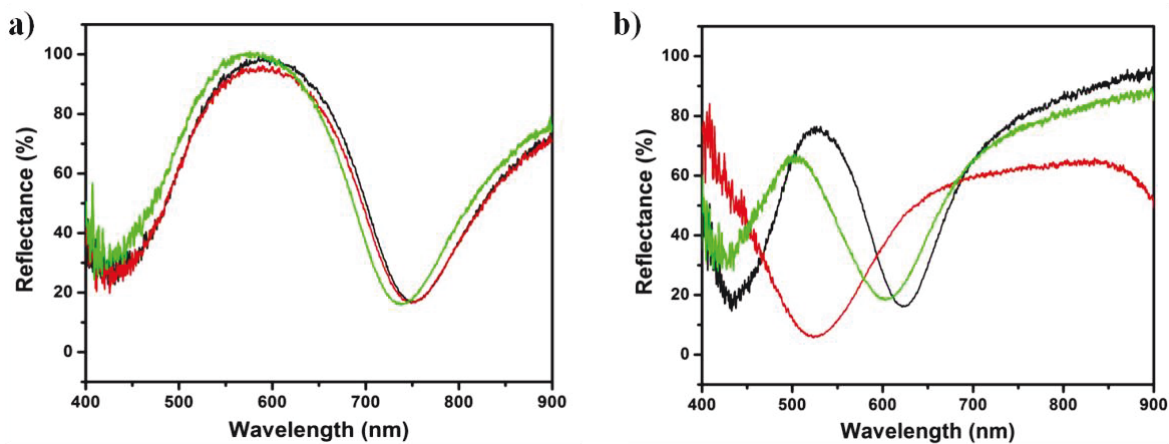
Figure 6-11. The reflectance spectrum of three random spots from an Au@pNIPAm microgel based etalon device (a) and an AuNPs impregnated microgel based etalon device (b).
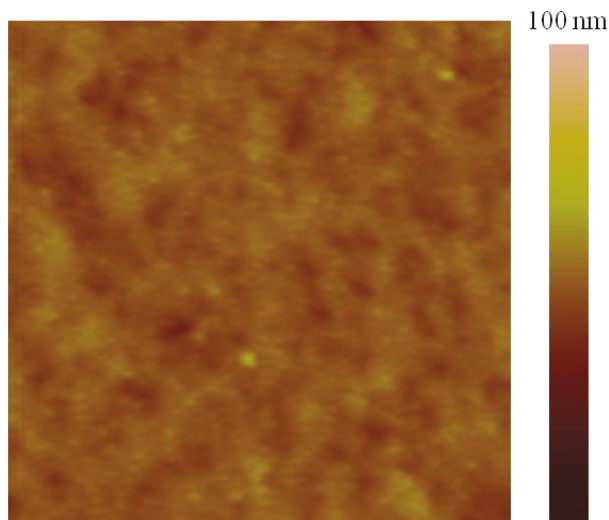
Figure 6-12. The AFM image of a p(NIPAm-*co*-AAc)-AuNPs microgel based etalon device in air. The scanning size is 100 μm^2.
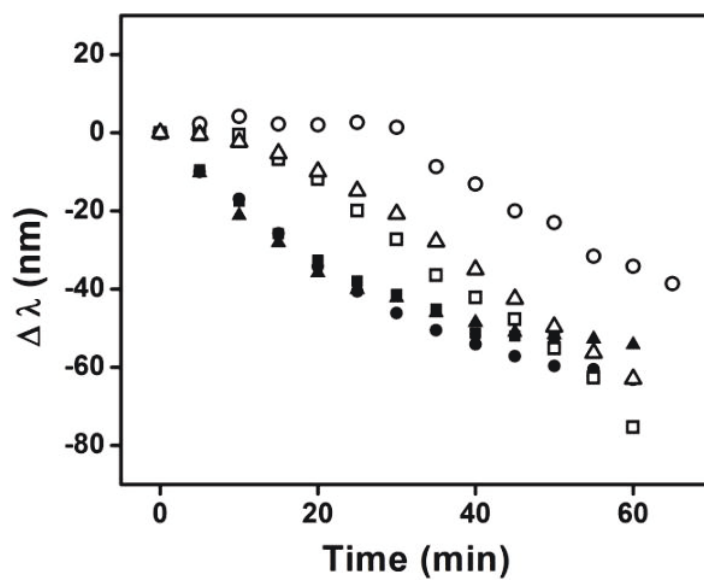
Figure 6-13. The reflectance spectra blue shifts as a function of irradiation time from three random spots of an Au@pNIPAm microgel based etalon device (filled) and an AuNPs impregnated microgel based etalon device (open).

6.4 Conclusions

In summary, it has been demonstrated that Au@pNIPAm microgels can be used to fabricate an optical device which is able to respond to temperature and a specific wavelength of light. The thermoresponsive properties of the device came from the inherent properties of the pNIPAm shell, which exhibits a LCST of ~32 ℃. The light responsivity was fulfilled by taking advantage of the fact that AuNPs are able to absorb green light and generate heat locally. Specifically, the LSPR can be generated on the AuNPs core with green light irradiation, which is finally released by a non-radiative pathway as heat. The local heat energy can lead to pNIPAm shell collapse and a concomitant spectrum blue shift. Moreover, it was found that the thermal and light response of such a device could be cycled many times without significant loss of functionality. Finally, the impact of the AuNPs distribution in the microgel to light responsivity have been investigated and showed uniform optical spectra and fast response in the Au@pNIPAm microgel based device. In future, it is expected to fabricate these optical devices with a tunable AuNPs core morphology such that they respond to NIR light, which is considered as a transparency "therapeutic window" with deeper penetration depth and less absorption and scattering in vivo. Potentially, such a device can be used for a locally triggered on-demand drug delivery platform.

Chapter 7

Polymer Brush Based Multiple Responsive Optical Device

Poly(N-isopropylacrylamide-*co*-acrylic acid) (pNIPAm-*co*-AAc) polymer brushes were grown from Au-coated glass substrates via surface initiated atom transfer radical polymerization (SI-ATRP). Subsequently, another thin Au layer was deposited on top of the brush to yield a sandwich structure, with the brush confined between the two Au layers. This structure was shown to exhibit excellent optical properties and shows a response to multiple external stimuli, such as pH, temperature and humidity. This novel device could be used for sensing, biosensing, drug delivery or for other applications that require light manipulation and wavelength filtration.

7.1 Introduction

Since the pioneering work of Yablonovitch[180] and John[181] in 1987, photonic materials have attracted significant attention. These materials possess periodic refractive index variability and can be classified as one-dimensional (1D), two-dimensional (2D) or three-dimensional (3D), depending on whether their periodicity is in 1, 2 or 3 dimensions, respectively. Photonic

materials have found many uses and applications, e.g., optical fibers,[182] photovoltaic devices,[183] displays[184] and sensors.[185] While photonic materials in general are of great interest, structures that change their optical properties in response to stimuli only increase their utility. Previously, a number of materials have been used to fabricate these devices. Among them, responsive polymer-based photonic structures[186] have emerged as some of the most useful.[187] Structures have been made that respond to stimuli such as pH,[188] ionic strength,[185a] solvent,[189] and electric[190] and magnetic fields.[191] In our previous studies, we demonstrated that poly (N-isopropylacrylamide) (pNIPAm)-based hydrogel particles (microgels) could be used to fabricate tunable photonic materials.[104, 178, 192]

PNIPAm has received significant attention over the years due to its thermally switchable solubility and conformation in water.[172c] Specifically, in water of a temperature lower than pNIPAm's lower critical solution temperature (LCST) of 32 ℃, it is fully soluble and exists as a random coil, while pNIPAm collapses and becomes insoluble when the temperature above 32 ℃. PNIPAm has been used for a variety of applications including: separations,[193] biotechnology,[194] actuation[195] and tissue engineering.[196] As mentioned above, pNIPAm can exist as a random coil in solution, while it can also be crosslinked into network structures to make hydrogels and hydrogel particles (microgels).[197]

In this Chapter, we synthesize pNIPAm-based brushes on surfaces. Polymer brushes are polymer chains tethered to a surface or interface via physisorption[198] or covalent attachment.[199] Physisorption involves the adsorption of polymer chains on the surface or interface, however, the polymer attachment can be weakened at high temperature and upon solvent replacement.[198, 200] To yield a more robust film, covalent attachment can be used. This can be achieved via "grafting

to" or "grafting from" techniques.[201] The "grafting to" method involves polymers diffusing to the substrate surface and reacting with a surface functional group. The "grafting from" approach uses a surface that has a reactive group, e.g., initiator or monomer, covalently attached to a surface, which can be polymerized. In this case, the thickness of the polymer film can be controlled by varying the polymerization time. One of the most common polymerization methods used for "grafting from" is atom transfer radical polymerization (ATRP).[202] Compared to traditional radical polymerizations, it provides control of polymer chain elongation, which gives narrow polydispersity index (PDI) and controlled molecular weight. In this way, the thickness of polymer brushes can be controlled.[203]

We used a "grafting from" approach to generate a pNIPAm brush layer on an Au-coated glass substrate, and then deposited another thin Au layer on top of the resultant brush to make a "sandwich" structure. This device yields bright visual color, which could be tuned by adjusting the thickness of the polymer brush. Furthermore, the devices could change their color dynamically with temperature changes, i.e., tuning the pNIPAm solvation state allowed the brush thickness to be dynamically tuned, therefore changing the visual color. Additionally, we made the pNIPAm layer pH responsive by copolymerization of acrylic acid (AAc) into the pNIPAm layer, and its pH response was characterized. Finally, we investigated the device's response to humidity.
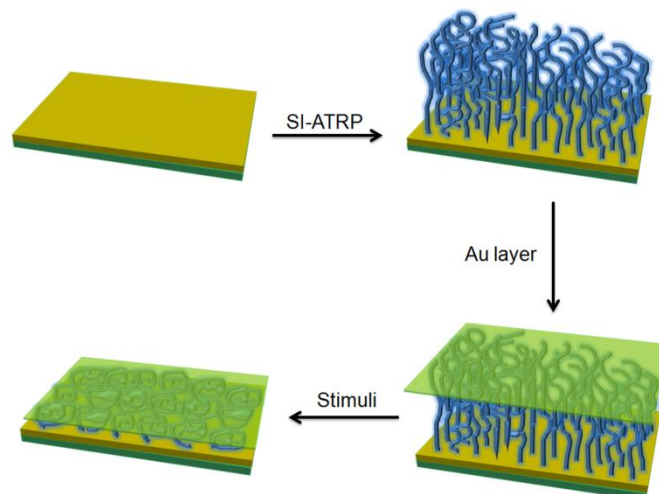
Figure 7-1. A schematic representation of the fabrication process of a polymer brush based optical device.

7.2 Experimental Section

7.2.1 Materials

N-isopropylacrylamide (NIPAm) was purchased from TCI (Portland, Oregon) and purified by recrystallization from hexanes (ACS reagent grade, EMD, Gibbstown, NJ) before use. Copper(I) bromide (Cu^{I}Br, 98%, Aldrich), was purified by adding it to a 10% H$_2$SO$_4$ solution, followed by addition of a saturated NaHSO$_3$ solution. After stirring for 5 min, the precipitated CuBr was separated by vacuum filtration and washed by acetic acid, anhydrous ethanol and ether, which finally yielded a white powder. Anhydrous ethanol (Brampton, Ontario) was processed by adding 3 Å molecular sieve. Acrylic acid (99%, Aldrich), 2-Bromo-2-methylpropionyl bromide (BiBB, 98%, Aldrich), 11-Mercapto-1-undecanol (97%, Aldrich), N,N,N',N',N''-pentamethyldiethyldiethylenetriamine (PMDETA, 99%, Aldrich), dichloromethane (>99.8%, Aldrich) were used as received, without further purification. Milli-Q

deionized water (DI H_2O) with a resistivity of 18 MΩ·cm was used. Glass microscope slides were purchased from Fisher. Chromium (99.999%) was purchased from ESPI (Ashland, OR) and Gold (99.99%) from MRCS Canada (Edmonton, AB, Canada).

7.2.2 Instrumentation

Imaging Ellipsometer (Nano film ep4, Accurion, Germany), Atomic Force Microscopy (Digital Instrument, Dimension 3100), Reflectance Spectroscopy (Ocean optics, Dunedin), Thermal Evaporator (Torr International Inc., NY).

7.2.3 ATRP initiator $(BrC(CH_3)_2COO(CH_2)_{10}S)_2$ Synthesis[204]

11-Mercapto-1-undecanol (1.02 g), 10% potassium hydrogen carbonate (5 mL) and dichloromethane (40 mL) were added to a round-bottom flask and stirred for 30 min to mix well. Bromine (0.4 g) was added dropwise to the mixture, with continuous stirring, for another 30 min. The organic phase was separated and the aqueous phase was extracted with dichloromethane (15 mL x 2) twice. The organic phases were combined and dried by magnesium sulfate. After vacuum filtration, the solvent was collected and rotary evaporated, yielding a white solid. The crude disulfide was recrystallized from an ethanol/hexane solution.

Recrystallized disulfide (0.55 g) and triethylamine (1.9 mL) were dissolved in dichloromethane (31.4 mL) and incubated in an ice bath under a N_2 environment, and 2-bromo-2-methylpropionyl bromide (0.42 mL) was added drop by drop to the mixture. After stirring for 1 h, the solution was moved to room temperature and stirred for another 2 h. The solution was extracted by 2 M sodium carbonate, followed by saturated ammonium. The organic phase was

dried by magnesium sulfate and was evaporated. The crude product was purified by column chromatography (hexane:ethyl acetate 13:1 V/V), resulting in a pale yellow oil.

7.2.4 Surface-Initiated ATRP Preparation of PNIPAM Brush

Microscope slides (1×1 inch) were washed copiously with ethanol and DI H_2O. After drying with N_2 gas, they were put in a thermal evaporator to coat an adhesive layer of Cr (2 nm) followed by a 50 nm thick layer of Au. The freshly prepared slides were immersed into a 0.5 mM initiator solution (dissolved in anhydrous ethanol) and allowed to sit for 3 h at room temperature. The initiator modified slides were rinsed with ethanol and dried by N_2 before use. NIPAm (6.9 g) was dissolved in water (68 mL) and degased with N_2 for 3 h, and PMDETA (216 μL) was added to methanol (20 mL) and degased with N_2 for 3 h. After that, CuBr (31.15 mg) was added to the methanol mixture under a N_2 environment and was sonicated for 30 s. The microscope slide was put in a reaction vessel with a N_2 stream, and 17 mL degased NIPAM solution was transferred to the vessel with a syringe, followed by a 2 mL degased CuBr/PMDETA/methanol solution. The reaction time was varied from 5 min to 6 h. After the polymerization, the slides were removed from the vessel, washed with copious methanol and water and dried with nitrogen.

7.2.5 Surface-Initiated ATRP Preparation of P(NIPAm-*co*-AAc) Brush

The procedure was similar to the one used in preparing pNIPAm brushes. Instead of using a NIPAm solution, acrylic acid (6 mL) was added to the monomer solution. After that, 0.5 M sodium hydroxide was added to adjust the pH of the mixture close to 7.

7.2.6 Ellipsometry and Atomic Force Microscope Analysis

The thickness of NIPAm based brushes was measured by ellipsometry with an angle of incidence (AOI) of 42 degrees and multiple wavelengths (from 400 nm to 900 nm in increments of 40 nm between each scan). Each slide was measured in three spots, and each spot was selected in three areas of interest, with a total of nine areas measured. The fitting parameters for NIPAM were a refractive index (n) of 1.485 and an absorption coefficient (k) of 0. The thicknesses of Au-brushes-Au assemblies and the surface topology were also measured by AFM. The polymerization time vs. NIPAm film thickness measured by ellipsometry and AFM were compared.

7.2.7 Reflectance Spectrum Measurement

Reflectance measurements were conducted in a temperature controlled chamber. The reflectance spectra were recorded using Ocean Optics Spectra Suite Spectroscopy Software. To evaluate the reproducibility of temperature response, the temperature was increased from 24 ℃ to 40 ℃ and then decreased back to 24 ℃ for several runs. For the pH response reproducibility of pNIPAm-*co*-AAc brushes, the pH was changed from ~2.7 to ~6.2 and back to ~2.7 for several runs by adding diluted HCl or NaOH solution.

7.3 Results and Discussion

Initially, pNIPAm-based brushes were grown onto Au-coated glass substrates, as shown in Figure 7-1. First, an ATRP initiator was attached to the Au surface by a self-assembly process in anhydrous ethanol. Following this step, surface-initiated atom transfer radical polymerization (SI-ATRP)[199a, 202b] was conducted to produce the desired brush. The resultant brush was characterized by ellipsometry and atomic force microscopy (AFM) as shown in Figure 7-2 and

7-3. Ellipsometry revealed that the thickness could be tuned over 300 nm, with a RMS roughness on the order of less than 20 nm. Finally, another 15 nm Au layer was thermally evaporated onto the resultant polymer brush. This yields a layered structure, which is capable of interacting with light to produce color. Specifically, light is capable of entering the brush-based cavity and undergoes multiple reflections, yielding constructive and destructive interference. This interference allows specific wavelengths of light to be reflected/transmitted, yielding color. The specific wavelengths that are reflected can be predicted from Eq. (38),

$$m\lambda = 2nd \cos \theta \tag{38}$$

where λ is the wavelength maximum of the reflected peak/peaks, m is the peak order, n is the refractive index of the dielectric medium, d is the distance between the two layers of Au and θ is the incident angle. It can be seen that the wavelength is directly proportional to the distance between these two layers of Au. Since the distance can be tuned by the pNIPAm brush responsivity, the position of the device's reflectance peaks and its color can be tuned dynamically.
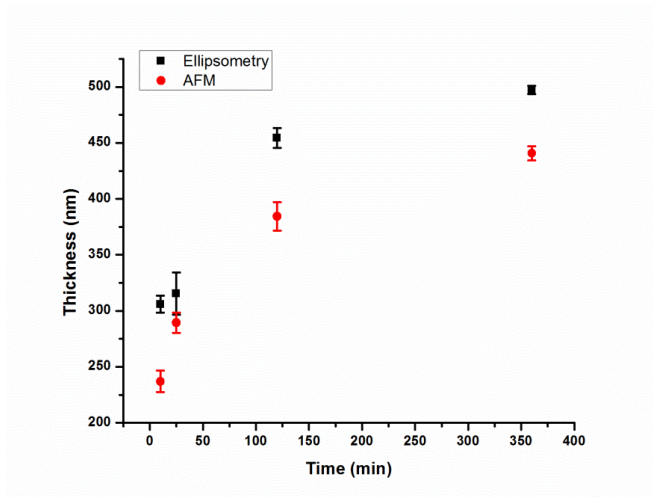
Figure 7-2. PNIPAm polymer brushes thickness measured as a function of different polymerization time by Ellipsometry (■) and AFM (●).
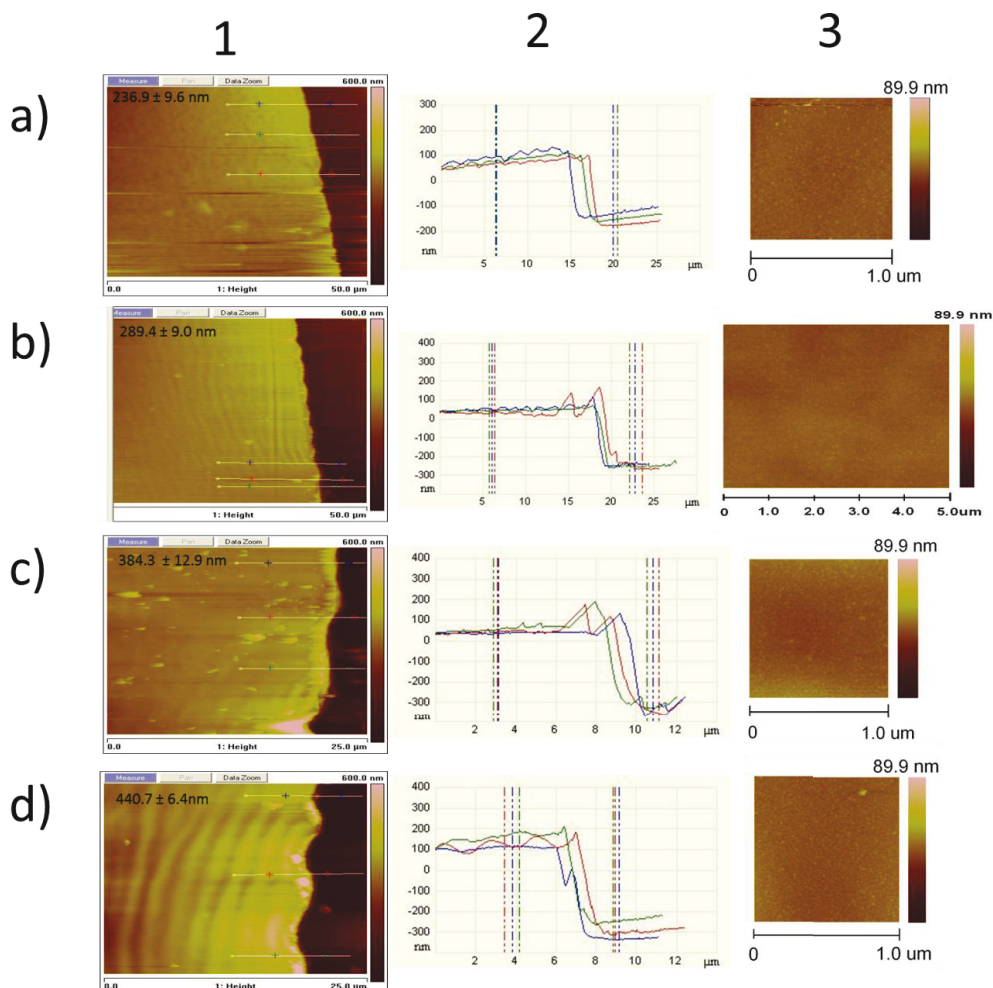
Figure 7-3. AFM Images of pNIPAm brushes based devices. a), b), c), d) are four different samples. The first column shows AFM images of the Au-pNIPAm assemblies' surface with a razor scratch. The second column shows the height information that correlated with the cross section in AFM images of the first column. The third column shows the surface topology of different thicknesses of the device. The thickness was measured by AFM in air. a) 236.9 ± 9.6 nm, b) 289.4 ± 9.0 nm, c) 384.3 ± 12.9 nm, d) 440.7 ± 6.4 nm.

Etalons composed of a variety of brush thicknesses were fabricated, and their optical properties investigated. As shown in Figure 7-4, when white light is exposed to the devices, specific wavelengths of light are reflected as dictated by the brush thickness. As the brush

thickness of the brush is increased, the number of peaks in the reflectance spectrum increases. This is a direct result of more orders of reflection being possible when the dielectric thickness of the etalons increases, as can be predicted from Eq. (38).
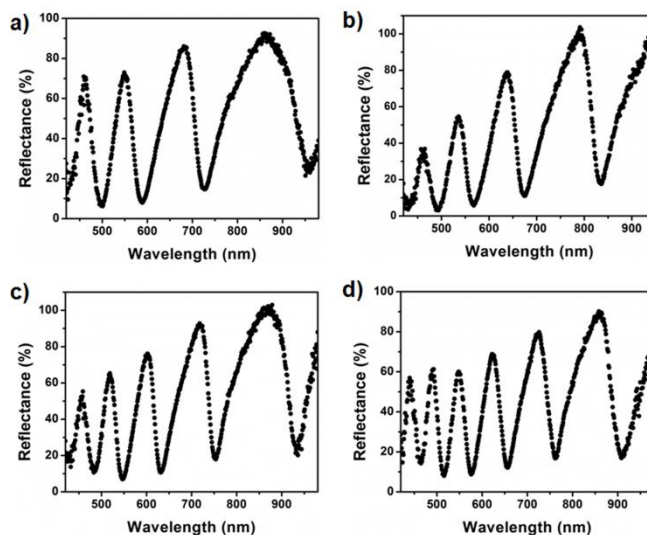
Figure 7-4. The reflectance spectra of pNIPAm polymer brush based devices with different brush thicknesses. The thickness was measured by AFM in air as shown in Figure 7-3 with: a) 236.9 ± 9.6 nm, b) 289.4 ± 9.0 nm, c) 384.3 ± 12.9 nm, d) 440.7 ± 6.4 nm.

To investigate the ability of these devices to respond to multiple stimuli, we prepared pNIPAm-based brushes with and without AAc. The various responsivities are shown in Figure 7-5. First, a pNIPAm brush-based device was generated, and its response to temperature investigated. In this case, the device was investigated using reflectance spectroscopy, and the position of a single wavelength monitored as an indicator of its response. As can be seen in Figure 7-5a, the device's reflectance peak shifted an impressive ~500 nm when the water temperature was changed from 24 to 40 ℃. The variability from device to device (polymer brush synthesized in the same batch) was investigated over the thermoresponsivity. As can be seen from Figure 7-6, a slight difference in the wavelength shift as a function of temperature can be

observed from the three pNIPAm brushes based devices. Additionally, the visible color of the device changed dramatically as shown in Figure 7-7. The response is a direct result of the pNIPAm brush layer collapsing at T > LCST, bringing the device's Au layers close to one another. The response was shown to be reversible over many cycles in Figure 7-8.

In addition to the temperature response, we looked into the pH response for the AAc-modified brushes. As AAc exhibits a pK_a value of ~4.25, it is deprotonated and negatively charged at pH > 4.25, while it is neutral at pH < 4.25. Coulombic repulsion of negative charges at pH > 4.25 causes the polymer brush to expand, which increases the distance between these two layers of Au. This response is expected to yield a red shift of the reflectance peaks, while protonation of the AAc groups (to neutralize the AAc groups) will cause the polymer to recontract and yield a blue shift in the reflectance spectrum. As can be seen in Figure 7-5b, the reflectance peaks yielded a red shift from 440 nm to 570 nm as the pH was brought above the AAc pK_a, and went back to the original position once the pH returned to < 4.25. The pH response is also reproducible over many cycles, as shown in Figure 7-9. We also investigated the temperature response at both high and low pH as shown in Figure 7-5c. At pH 2.44, the wavelength shifted from 800 nm to 600 nm as temperature was increased from 22 to 34 ^{o}C. As can be seen, the transition temperature for these devices is lower than the devices without AAc as a result of the increased hydrophilicity of the brush due to the AAc groups. At pH 6.50 (above the AAc pK_a), the wavelength shifts from 600 nm to 500 nm when temperature in increased from 24 to 40 ^{o}C. The minimal temperature responsivity is a result of the negative charges in the brush preventing the collapse at high temperature. As can be seen from Figure 7-10, the p(NIPAm-*co*-AAc) polymer brush based optical device showed obvious color change as temperature increased above its LCST at pH 3 solution.

Finally, we demonstrated that the pNIPAm-*co*-AAc brush-based devices exhibit optical responses to atmospheric humidity changes. As shown in Figure 7-5d, the wavelength shifts from 470 nm to 550 nm as the relative humidity increases. Large wavelength shifts can be observed when humidity increases up to 40 %. The reason for the red shift is that the polymer brush chain is in a collapsed state when the humidity is low, while it transitions to a more solvated state as the humidity increases. This is a result of the hygroscopic properties of the pNIPAm-based brush.
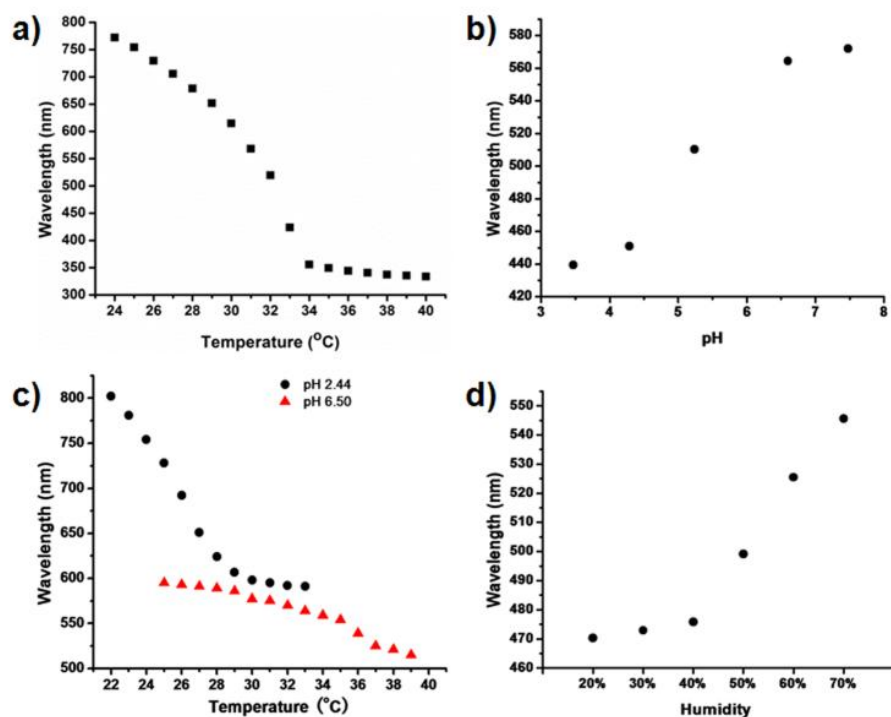
Figure 7-5. Stimuli-responsive properties of a polymer brush based device. a) Temperature responsivity on a pNIPAm brush based device; b) pH responsivity on a p(NIPAm-*co*-AAc) brush based device; c) temperature responsivity on a p(NIPAm-*co*-AAc) brush based device; d) humidity responsivity on a p(NIPAm-*co*-AAc) brush based device.
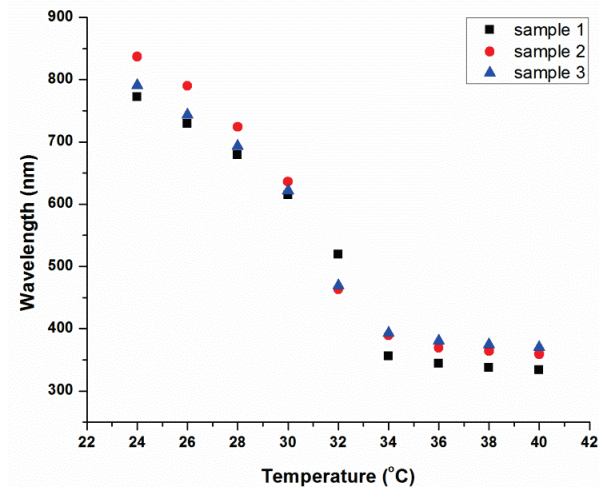
Figure 7-6. The temperature response of pNIPAm brushes based devices.
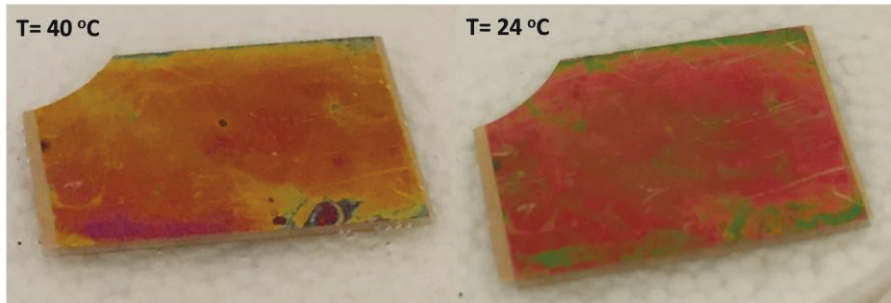
Figure 7-7. Images of a pNIPAm brushes based device in DI H_2O at different temperatures.
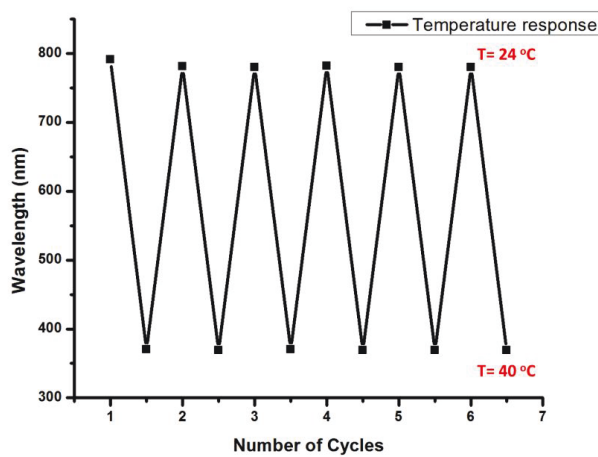
Figure 7-8. The response of pNIPAm brushes to temperature change from 24 °C to 40 °C for 6 cycles.
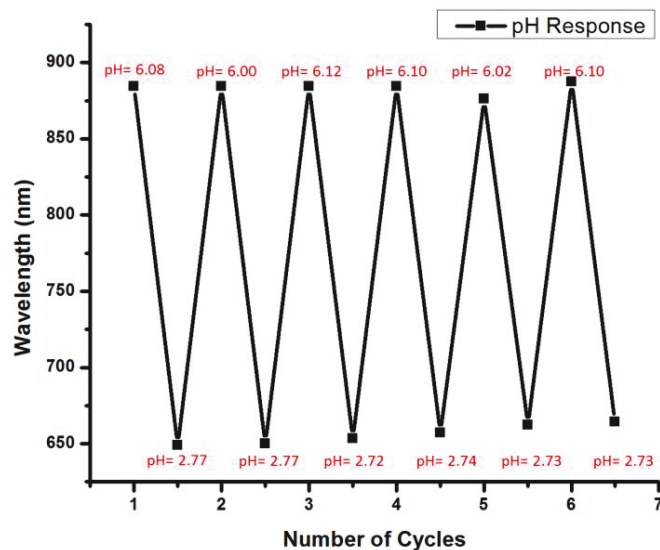
Figure 7-9. The response of p(NIPAm-*co*-AAc) brushes to pH change from ~ 2.7 to ~6.1 for 6 cycles.
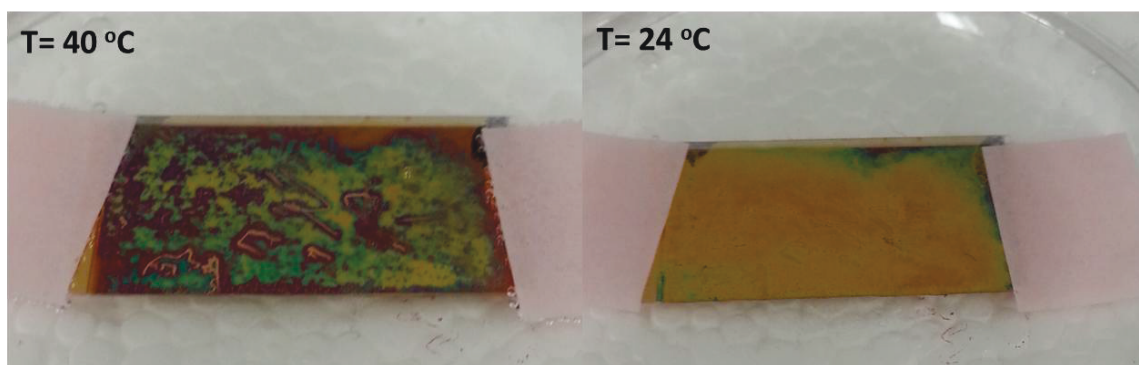
Figure 7-10. Images of a p(NIPAm-*co*-AAc) brushes based device in a pH 3 solution at different temperatures.

7.3 Conclusions

In conclusion, we have demonstrated a multiple stimuli-responsive optical device that exhibits responsivity to temperature, pH and humidity. The basic concept is based on the conformation change of polymer brushes under external stimuli and can be revealed in a readable

fashion. This device is versatile and is based on different functional monomers polymerized on this brush structure. In addition, by incorporating with specific molecules, the polymer brushes serve as a backbone; the specific interaction of these molecules with external stimuli or triggers can result in a size change, and potentially can be used as a sensor or drug delivery platform.

Chapter 8

Conclusions and Future Work

8.1 Conclusions of SPR Instrument

A high performance SPR spectrometer with a broad scanning range, angular resolution of 0.001° and multi-operation mode has been built for surface–surface interaction studies as well as sensing and biosensing studies. A LabVIEW based program has been developed with multifunction abilities including instrument motion controls, sensor-probe surface distance monitoring and data collections. However, improvements are still needed for the surface confinement control, which is expected to work at nanometer levels.

8.2 Conclusions of SPR Signal Enhancement

Novel thermoresponsive microgel-based thin films/Au assemblies were deposited on SPR sensor surfaces, leading to a multi-fold enhanced SPR signal in response to the microgel solvation state changes. The microgels conformation changes can be ascribed to either temperature changes or the concentration changes of small biomolecules of interest at constant temperature. Such assemblies showed higher sensitivity than those without an additional layer of Au film. The enhancement dependence of the top layer Au film thickness was investigated as a function of temperature, with the best sensitivity achieved when the Au overlayer thickness is 5

nm. The reason of enhancement can be ascribed to the efficient plasmon coupling and scattering effect of the assemblies.

A competitive assay based on a p(NIPAm-*co*-GEMA) microgel film was applied to amplify the SPR signals in glucose detection. The principle is that the conformation of the p(NIPAm-*co*-GEMA) microgels on the SPR sensor surface is altered isothermally as ConA association/dissociation takes place from the polymer networks. Both the glucose and GEMA in polymer networks were able to bind to ConA. Such assay has shown a 9-fold enhancement, which gives better sensitivity in detecting physiological concentrations of glucose than unmodified SPR Au sensor. The enhancement factor was slightly lower than that in the previous case (microgel/Au film assemblies) owing to the absence of the additional Au layer. Even with a thin Au film, such as 5 nm, the protein (ConA) is hard to penetrate through the Au film barrier. By specifically tailoring the chemistry of the microgel film, SPR sensor surfaces can be designed and fabricated for the detection of desirable small molecules.

8.3 Conclusions of the Universal Au Nanoarray Substrate for SPR Sensing and SERS

A simple and cost effective approach to Au nano array fabrication has been demonstrated by painting the Au@pNIPAm core shell microgel particles on the silicon wafer. The shell thickness (pNIPAm layer) can be tuned either by varying the seed/monomer ratio in the synthesis or the environmental solution temperature. Therefore, the periodicity of the Au nano array can be tuned dynamically by painting different batches of the Au@pNIPAm microgel particles or varying the painting temperature with the same batch of microgel particles. Furthermore, the Au core sizes were tunable by further growing on the Au@pNIPAm microgel particles. By tuning

the Au nanoarray periodicity and Au core size, an approximate 10^7 enhance factor is expected to be observed in SERS sensor.

8.4 Conclusions of the Etalon based Optical Device

A thermal/light dual responsive optical device composed of Au@pNIPAm core shell microgels has been demonstrated. The thermal responsivity is the intrinsic property of the pNIPAm shell that exhibits a swollen-to-collapsed state transition upon temperature changes, while the light responsivity is fulfilled by the LSPR properties of the Au core. The AuNPs can absorb green light and generate heat locally, which further can lead to the pNIPAm shell collapse and a concomitant spectrum blue shift. Moreover, the thermal and light response of such a device could be cycled many times without significant functionality loss. The optical heterogeneity and fast response of such a device showed its potential application in a remote light triggered drug releasing platform.

A multi-responsive optical device composed of p(NIPAm-*co*-AAc) polymer brushes has been fabricated, which is able to change color under the stimuli of temperature, pH and humidity. This device exhibits spectral uniformity over a 1×1 inch area and reproducibility over multiple pH/temperature/humidity cycles due to the homogeneity of polymer brushes synthesized via ATRP. The brushes thickness is varied by controlling the reaction time.

The versatility of the etalon device was proved by varying the dielectric medium between the two Au films in the etalon, which can be spherical microgels or polymer brushes. In addition, the chemistry of microgel/polymer brushes can further be explored for the desired functionality.

8.5 Future Work in SPR Instrument and SPR based Sensing Strategies

Once the instrument meets all the requirements mentioned in the introduction of Chapter 1, polymer–polymer interactions under confinement can be studied. First, the polymer brushes with a controllable thickness and graft density will be modified on the sensor and probe surfaces via the ATRP techniques (in Chapter 7). By tuning these parameters, such as polymer chemistry, polymer chain lengths, grafting densities and solvent, one can collect information about the impact of these factors on the conformation changes of the polymer brushes (sensor surface) as a function of distances to other brush layers (probe surface). Based on these fundamental studies, a surface coating with the desired tribology can be designed for use under confinement conditions.

On the other hand, the development of a portable SPR instrument is necessary for the POC application. Two factors need to be taken into consideration. First is the method for optical excitation of SPR. As described in Chapter 1, both the gratings coupling and the fiber optics are good options for the SPR setup miniaturization. Instead of applying an angular interrogation in SPR, a wavelength based platform can be used to reduce the complexity of the optical components and avoid the use of expensive light sources. Second is the solution handling platform in the SPR instrument. Microfluidic cells can meet the requirements for a low volume of sampling solution, instrument integrity and ease of operation. As demonstrated in Chapter 3 and 4, a stimuli-responsive polymer based transducer (with or without additional Au film) can be used in the portable SPR instrument to amplify the SPR signal and enhance the overall performance.

Other challenges in the SPR based sensing technology involve the detection of pathogens and cells because of their size, which are larger than the penetration depth of the evanescent

field. More focus should be put on the assay development for such a requirement. In addition, the design of the metal and dielectric medium interface should be considered.

8.6 Future Work in Au Nanoarray Surfaces

The optical properties of the Au nanoarray should be investigated either theoretically by finite different time domain or experimentally by reflectance/transmission spectra with periodicity and AuNPs size variation; this will provide very useful information for rational sensor surface design. In addition, the optimized substrates should be tested by SPR or SERS to calculate the enhancement factor.

8.7 Future Work in Au@pNIPAm Core Shell Microgels

The chemistry of a shell layer in Au@pNIPAm core shell particles can be tailored to respond to biological molecules of interest. In the presence of the target, the conformation of the shell can be tuned to have an impact on the LSPR properties of the AuNPs core. The Au@pNIPAm core-shell microgels by itself in solution can be applied in a sensing platform due to the LSPR effect of the AuNPs core. Instead of utilizing it as an assembly on the solid substrates (collective effect), the solution based assay has the advantage of fewer processing steps and an easy readout (without the need of additional spectroscopy) for signal processing. By observing the turbidity change of the solution, one can tell the presence or absence of the target of interest.

Bibliography

1. Ritchie, R., Plasma losses by fast electrons in thin films. *Physical Review* **1957,** *106* (5), 874.

2. Wood, R., On a remarkable case of uneven distribution of light in a diffraction grating spectrum. *Philosophical Magazine* **1902**, *4*, 396.

3. Fano, U., The theory of anomalous diffraction gratings and of quasi-stationary waves on metallic surfaces (Sommerfeld's waves). *Journal of the Optical Society of America,* **1941,** *31* (3), 213-222.

4. Stern, E.; Ferrell, R., Surface plasma oscillations of a degenerate electron gas. *Physical Review* **1960,** *120* (1), 130.

5. Kanazawa, H., On the plasma oscillations in metal foils. *Progress of Theoretical Physics* **1961,** *26* (6), 851-860.

6. (a) Otto, A., Excitation of nonradiative surface plasma waves in silver by the method of frustrated total reflection. *Zeitschrift für Physik* **1968,** *216* (4), 398-410; (b) Otto, A., A new method for exciting non-radioactive surface plasma oscillations. *Physica Status Soldi(b)* **1968,** *26*, 99-101.

7. Kretschmann, E.; Raether, H., Radiative decay of non radiative surface plasmons excited by light. *Zeitschrift für Naturforschung A* **1968,** *23* (12), 2135-2136.

8. Liedberg, B.; Nylander, C.; Lunström, I., Surface plasmon resonance for gas detection and biosensing. *Sensors and actuators* **1983,** *4*, 299-304.

9. Schasfoort, R. B.; Tudos, A., Introduction to surface plasmon resonance.In *Handbook of Surface Plasmon Resonance,* The Royal Society of Chemistry: Cambridge, 2008, pp 1-13.

10. (a) Piliarik, M.; Vaisocherová, H.; Homola, J., Surface plasmon resonance biosensing. *Biosensors and Biodetection* **2009**, 65-88; (b) Homola, J.; Yee, S. S.; Gauglitz, G., Surface plasmon resonance sensors. *Sensors and Actuators B: Chemical* **1999,** *54* (1), 3-15; (c) Liedberg, B.; Nylander, C.; Lundström, I., Biosensing with surface plasmon resonance—how it all started. *Biosensors and Bioelectronics* **1995,** *10* (8), i-ix; (d) Hoa, X.; Kirk, A.; Tabrizian, M., Towards integrated and sensitive surface plasmon resonance biosensors: a review of recent progress. *Biosensors and Bioelectronics* **2007,** *23* (2), 151-160.

11. Maier, S. A., *Plasmonics: Fundamentals and Applications*. Springer-Verlag: US, 2007.

12. Ashcroft, N. W.; Mermin, N. D., *Solid State Physics*. Holt, Rinehart and Winston: New York, 1976.

13. Johnson, P. B.; Christy, R.-W., Optical constants of the noble metals. *Physical review B* **1972,** *6* (12), 4370.

14. (a) Homola, J., Electromagnetic theory of surface plasmons. In *Surface plasmon resonance based sensors,* Springer-Verlag: Berlin Heidelbberg, 2006, pp 3-44; (b) Pitarke, J.; Silkin, V.; Chulkov, E.; Echenique, P., Theory of surface plasmons and surface-plasmon polaritons. *Reports on Progress in Physics* **2006,** *70* (1), 1.

15. Raether, H., Surface plasmons on smooth surfaces. In *Surface Plasmons on Smooth and Rough Surfaces and on Gratings*, Springer-Verlag: Berlin Heidelbberg, 1988, pp 4-39.

16. Jung, L. S.; Campbell, C. T.; Chinowsky, T. M.; Mar, M. N.; Yee, S. S., Quantitative interpretation of the response of surface plasmon resonance sensors to adsorbed films. *Langmuir* **1998,** *14* (19), 5636-5648.

17. Wang, S.; Shan, X.; Patel, U.; Huang, X.; Lu, J.; Li, J.; Tao, N., Label-free imaging, detection, and mass measurement of single viruses by surface plasmon resonance. *Proceedings of the National Academy of Sciences* **2010,** *107* (37), 16028-16032.

18. Homola, J.; Koudela, I.; Yee, S. S., Surface plasmon resonance sensors based on diffraction gratings and prism couplers: sensitivity comparison. *Sensors and Actuators B: Chemical* **1999,** *54* (1), 16-24.

19. Kurihara, K.; Suzuki, K., Theoretical understanding of an absorption-based surface plasmon resonance sensor based on Kretchmann's theory. *Analytical Chemistry* **2002,** *74* (3), 696-701.

20. Homola, J., Present and future of surface plasmon resonance biosensors. *Analytical and Bioanalytical Chemistry* **2003,** *377* (3), 528-539.

21. (a) Wang, S.; Boussaad, S.; Wong, S.; Tao, N., High-sensitivity stark spectroscopy obtained by surface plasmon resonance measurement. *Analytical Chemistry* **2000,** *72* (17), 4003-4008; (b) Tao, N.; Boussaad, S.; Huang, W.; Arechabaleta, R.; D'Agnese, J., High resolution surface plasmon resonance spectroscopy. *Review of Scientific Instruments* **1999,** *70* (12), 4656-4660.

22. (a) Pollet, J.; Delport, F.; Janssen, K. P.; Jans, K.; Maes, G.; Pfeiffer, H.; Wevers, M.; Lammertyn, J., Fiber optic SPR biosensing of DNA hybridization and DNA–protein interactions. *Biosensors and Bioelectronics* **2009,** *25* (4), 864-869; (b) Sharma, A. K.; Jha, R.; Gupta, B., Fiber-optic sensors based on surface plasmon resonance: a comprehensive review. *IEEE Sensors Journal* **2007,** *7* (8), 1118-1129.

23. Yin, S. S.; Ruffin, P.B.,Yu F.T.S. *Fiber Optic Sensors*, Second Edition; CRC Press: Boca Raton, FL, USA, 2008.

24. Slav k, R.; Homola, J.; Čtyroký, J., Single-mode optical fiber surface plasmon resonance sensor. *Sensors and Actuators B: Chemical* **1999,** *54* (1), 74-79.

25. Gupta, B. D.; Verma, R. K., Surface plasmon resonance-based fiber optic sensors: principle, probe designs, and some applications. *Journal of Sensors* **2009,** *2009*.

26. Obando, L. A.; Gentleman, D. J.; Holloway, J. R.; Booksh, K. S., Manufacture of robust surface plasmon resonance fiber optic based dip-probes. *Sensors and Actuators B: Chemical* **2004,** *100* (3), 439-449.

27. Yuk, J. S.; Yi, S.-J.; Lee, H. G.; Lee, H. J.; Kim, Y.-M.; Ha, K.-S., Characterization of surface plasmon resonance wavelength by changes of protein concentration on protein chips. *Sensors and Actuators B: Chemical* **2003,** *94* (2), 161-164.

28. Long, F.; Zhu, A.; Shi, H., Recent advances in optical biosensors for environmental monitoring and early warning. *Sensors* **2013,** *13* (10), 13928-13948.

29. (a) Carrascosa, L.; Calle, A.; Lechuga, L., Label-free detection of DNA mutations by SPR: application to the early detection of inherited breast cancer. *Analytical and Bioanalytical Chemistry* **2009,** *393* (4), 1173; (b) Karlsson, R., SPR for molecular interaction analysis: a review of emerging application areas. *Journal of Molecular Recognition* **2004,** *17* (3), 151-161; (c) Quinn, J. G.; O'Neill, S.; Doyle, A.; McAtamney, C.; Diamond, D.; MacCraith, B. D.; O'Kennedy, R., Development and application of surface plasmon resonance-based biosensors for the detection of cell–ligand interactions. *Analytical Biochemistry* **2000,** *281* (2), 135-143.

30. (a) Jain, P. K.; Huang, X.; El-Sayed, I. H.; El-Sayed, M. A., Review of some interesting surface plasmon resonance-enhanced properties of noble metal nanoparticles and their applications to biosystems. *Plasmonics* **2007,** *2* (3), 107-118; (b) Zeng, S.; Baillargeat, D.; Ho, H.-P.; Yong, K.-T., Nanomaterials enhanced surface plasmon resonance for biological and chemical sensing applications. *Chemical Society Reviews* **2014,** *43* (10), 3426-3452.

31. Lee, E. G.; Park, K. M.; Jeong, J. Y.; Lee, S. H.; Baek, J. E.; Lee, H. W.; Jung, J. K.; Chung, B. H., Carbon nanotube-assisted enhancement of surface plasmon resonance signal. *Analytical Biochemistry* **2011,** *408* (2), 206-211.

32. Lyon, L. A.; Musick, M. D.; Natan, M. J., Colloidal Au-enhanced surface plasmon resonance immunosensing. *Analytical Chemistry* **1998,** *70* (24), 5177-5183.

33. Severs, A.; Schasfoort, R.; Salden, M., An immunosensor for syphilis screening based on surface plasmon resonance. *Biosensors and Bioelectronics* **1993,** *8* (3-4), 185-189.

34. He, L.; Musick, M. D.; Nicewarner, S. R.; Salinas, F. G.; Benkovic, S. J.; Natan, M. J.; Keating, C. D., Colloidal Au-enhanced surface plasmon resonance for ultrasensitive detection of DNA hybridization. *Journal of the American Chemical Society* **2000,** *122* (38), 9071-9077.

35. Stuart, M. A. C.; Huck, W. T.; Genzer, J.; Müller, M.; Ober, C.; Stamm, M.; Sukhorukov, G. B.; Szleifer, I.; Tsukruk, V. V.; Urban, M., Emerging applications of stimuli-responsive polymer materials. *Nature Material* **2010,** *9* (2), 101-113.

36. (a) Pelton, R., Poly (N-isopropylacrylamide)(PNIPAM) is never hydrophobic. *Journal of Colloid and Interface Science* **2010,** *348* (2), 673-674; (b) Schild, H. G., Poly (N-isopropylacrylamide): experiment, theory and application. *Progress in Polymer Science* **1992,** *17* (2), 163-249.

37. (a) Zhang, Q. M.; Li, X.; Islam, M. R.; Wei, M.; Serpe, M. J., Light switchable optical materials from azobenzene crosslinked poly (N-isopropylacrylamide)-based microgels. *Journal of Materials Chemistry C* **2014,** *2* (34), 6961-6965; (b) Zhang, Q. M.; Xu, W.; Serpe, M. J., Optical devices constructed from multiresponsive microgels. *Angewandte Chemie International Edition* **2014,** *53* (19), 4827-4831; (c) Zhang, Q. M.; Ahiabu, A.; Gao, Y.; Serpe, M. J., CO 2-switchable poly (N-isopropylacrylamide) microgel-based etalons. *Journal of Materials Chemistry C* **2015,** *3* (3), 495-498.

38. (a) Liu, F.; Urban, M. W., Recent advances and challenges in designing stimuli-responsive polymers. *Progress in Polymer Science* **2010,** *35* (1), 3-23; (b) Schattling, P.; Jochum, F. D.; Theato, P., Multi-stimuli responsive polymers–the all-in-one talents. *Polymer Chemistry* **2014,** *5* (1), 25-36; (c) Jeong, B.; Gutowska, A., Lessons from nature: stimuli-responsive polymers and their biomedical applications. *Trends in biotechnology* **2002,** *20* (7), 305-311; (d) Zhai, L., Stimuli-responsive polymer films. *Chemical Society Reviews* **2013,** *42* (17), 7148-7160.

39.   Bio-rad   Laboratories   Inc.   Protein   Interaction   Analysis.   http://www.bio-rad.com/webroot/web/pdf/lsr/literature/Bulletin_6044A.pdf.

40. Schreiber, G.; Haran, G.; Zhou, H.-X., Fundamental aspects of protein−protein association kinetics. *Chemical Reviews* **2009,** *109* (3), 839-860.

41. Howes, P. D.; Rana, S.; Stevens, M. M., Plasmonic nanomaterials for biodiagnostics. *Chemical Society Reviews* **2014,** *43* (11), 3835-3853.

42. Anker, J. N.; Hall, W. P.; Lyandres, O.; Shah, N. C.; Zhao, J.; Van Duyne, R. P., Biosensing with plasmonic nanosensors. *Nature Materials* **2008,** *7* (6), 442-453.

43. Yang, X.; Yang, M.; Pang, B.; Vara, M.; Xia, Y., Gold nanomaterials at work in biomedicine. *Chemical Reviews* **2015,** *115* (19), 10410-10488.

44. Murray, R. W., Nanoelectrochemistry: metal nanoparticles, nanoelectrodes, and nanopores. *Chemical Reviews* **2008,** *108* (7), 2688-2720.

45. Murphy, C. J.; Sau, T. K.; Gole, A. M.; Orendorff, C. J.; Gao, J.; Gou, L.; Hunyadi, S. E.; Li, T., Anisotropic metal nanoparticles: synthesis, assembly, and optical applications. *The Journal of Physical Chemistry B* **2005**, 109 (29), 13857-13870.

46. Loo, C.; Lin, A.; Hirsch, L.; Lee, M.-H.; Barton, J.; Halas, N.; West, J.; Drezek, R., Nanoshell-enabled photonics-based imaging and therapy of cancer. *Technology in Cancer Research &Ttreatment* **2004,** *3* (1), 33-40.

47. Sagle, L. B.; Ruvuna, L. K.; Ruemmele, J. A.; Van Duyne, R. P., Advances in localized surface plasmon resonance spectroscopy biosensing. *Nanomedicine* **2011,** *6* (8), 1447-1462.

48. Tokel, O.; Inci, F.; Demirci, U., Advances in plasmonic technologies for point of care applications. *Chemical Reviews* **2014,** *114* (11), 5728-5752.

49. Willets, K. A.; Van Duyne, R. P., Localized surface plasmon resonance spectroscopy and sensing. *Annual Review of Physical Chemistry* **2007,** *58*, 267-297.

50. Stewart, M. E.; Anderton, C. R.; Thompson, L. B.; Maria, J.; Gray, S. K.; Rogers, J. A.; Nuzzo, R. G., Nanostructured plasmonic sensors. *Chemical Reviews* **2008,** *108* (2), 494-521.

51. Haes, A. J.; Van Duyne, R. P., A nanoscale optical biosensor: sensitivity and selectivity of an approach based on the localized surface plasmon resonance spectroscopy of triangular silver nanoparticles. *Journal of the American Chemical Society* **2002,** *124* (35), 10596-10604.

52. Fedlheim, D. L.; Foss, C. A., *Metal nanoparticles: synthesis, characterization, and applications*. CRC Press: Boca Raton, FL, USA, **2001**.

53. Wang, Y.; Mirkin, C. A.; Park, S.-J., Nanofabrication beyond electronics. *ACS Nano* 2009, 3 (5), 1049-1056.

54. Eustis, S.; El-Sayed, M. A., Why gold nanoparticles are more precious than pretty gold: noble metal surface plasmon resonance and its enhancement of the radiative and nonradiative properties of nanocrystals of different shapes. *Chemical Society Reviews* **2006,** *35* (3), 209-217.

55. Lu, W.; Lieber, C. M., Nanoelectronics from the bottom up. *Nature Materials* **2007,** *6* (11), 841.

56. Pillai, Z. S.; Kamat, P. V., What factors control the size and shape of silver nanoparticles in the citrate ion reduction method? *The Journal of Physical Chemistry B* **2004,** *108* (3), 945-951.

57. Kariuki, N. N.; Luo, J.; Maye, M. M.; Hassan, S. A.; Menard, T.; Naslund, H. R.; Lin, Y.; Wang, C.; Engelhard, M. H.; Zhong, C.-J., Composition-controlled synthesis of bimetallic gold− silver nanoparticles. *Langmuir* **2004,** *20* (25), 11240-11246.

58. Wiley, B.; Herricks, T.; Sun, Y.; Xia, Y., Polyol synthesis of silver nanoparticles: use of chloride and oxygen to promote the formation of single-crystal, truncated cubes and tetrahedrons. *Nano Letters* **2004,** *4* (9), 1733-1739.

59. Srnov - loufov , I.; l kov , B.; Bastl, Z.; Hasslett, T. L., Bimetallic (Ag) Au nanoparticles prepared by the seed growth method: two-dimensional assembling, characterization by energy dispersive X-ray analysis, X-ray photoelectron spectroscopy, and surface enhanced Raman spectroscopy, and proposed mechanism of growth. *Langmuir* **2004,** *20* (8), 3407-3415.

60. Huang, C.-J.; Chiu, P.-H.; Wang, Y.-H.; Yang, C.-F., Synthesis of the gold nanodumbbells by electrochemical method. *Journal of Colloid and Interface Science* **2006,** *303* (2), 430-436.

61. Jin, R.; Cao, Y.; Mirkin, C. A.; Kelly, K.; Schatz, G. C.; Zheng, J., Photoinduced conversion of silver nanospheres to nanoprisms. *Science* **2001,** *294* (5548), 1901-1903.

62. Su, C.-H.; Wu, P.-L.; Yeh, C.-S., Sonochemical synthesis of well-dispersed gold nanoparticles at the ice temperature. *The Journal of Physical Chemistry B* **2003,** *107* (51), 14240-14243.

63. (a) Dahl, J. A.; Maddux, B. L.; Hutchison, J. E., Toward greener nanosynthesis. *Chemical Reviews* **2007,** *107* (6), 2228-2269; (b) Talapin, D. V.; Shevchenko, E. V., Introduction: Nanoparticle Chemistry. *Chemical Reviews* **2016**, 116 (18), 10343-10345.

64. Chen, W.; Ahmed, H., Fabrication of 5-7 nm wide etched lines in silicon using 100 keV electron-beam lithography and polymethylmethacrylate resist. *Applied Physics Letters* **1993,** *62* (13), 1499-1501.

65. Watt, F.; Bettiol, A.; Van Kan, J.; Teo, E.; Breese, M., Ion beam lithography and nanofabrication: a review. *International Journal of Nanoscience* **2005,** *4* (3), 269-286.

66. Hulteen, J. C.; Van Duyne, R. P., Nanosphere lithography: a materials general fabrication process for periodic particle array surfaces. *Journal of Vacuum Science & Technology A: Vacuum, Surfaces, and Films* **1995,** *13* (3), 1553-1558.

67. Yang, S. M.; Jang, S. G.; Choi, D. G.; Kim, S.; Yu, H. K., Nanomachining by colloidal lithography. *Small* **2006,** *2* (4), 458-475.

68. Qin, D.; Xia, Y.; Whitesides, G. M., Soft lithography for micro-and nanoscale patterning. *Nature protocols* **2010,** *5* (3), 491.

69. Xia, D.; Biswas, A.; Li, D.; Brueck, S. R., Directed Self-Assembly of Silica Nanoparticles into Nanometer-Scale Patterned Surfaces Using Spin-Coating. *Advanced Materials* **2004,** *16* (16), 1427-1432.

70. Manako, S.; Fujita, J.-i.; Ochiai, Y.; Nomura, E.; Matsui, S., Nanometer-scale patterning of polystyrene resists in low-voltage electron beam lithography. *Japanese Journal of Applied Physics* **1997,** *36* (12S), 7773.

71. Sun, Y.; Walker, G. C., Two-dimensional self-assembly of latex particles in wetting films on patterned polymer surfaces. *The Journal of Physical Chemistry B* **2002,** *106* (9), 2217-2223.

72. Mela, P.; Ott, M.; Spatz, J.; Gorzolnik, B.; Möller, M., Photochemical method for manufacturing nanometrically surface-decorated substrates. US7655383 B2, February 2 **2010**.

73. Xia, Y.; Whitesides, G. M., Soft lithography. *Annual Review of Materials Science* **1998,** *28* (1), 153-184.

74. (a) Koch, C., Top-Down Synthesis Of Nanostructured Materials: Mechanical And Thermal Processing Methods. *Reviews on Advanced Materials Science* **2003,** *5* (2), 91-99; (b) Zhang, S., Fabrication of novel biomaterials through molecular self-assembly. *Nature Biotechnology* **2003,** *21* (10), 1171.

75. (a) Priest, M.; Taylor, C., Automobile engine tribology—approaching the surface. *Wear* **2000,** *241* (2), 193-203; (b) Mansky, P.; Liu, Y.; Huang, E.; Russell, T.; Hawker, C., Controlling polymer-surface interactions with random copolymer brushes. *Science* **1997,** *275* (5305), 1458-1460; (c) Rabinowicz, E., Friction and wear of materials. **1965**; (d) Israelachvili, J. N., *Intermolecular and surface forces*. Third Edition, Academic press: San Diego, USA, 2011.

76. de Vos, W. M.; Mears, L. L.; Richardson, R. M.; Cosgrove, T.; Dalgliesh, R. M.; Prescott, S. W., Measuring the structure of thin soft matter films under confinement: A surface-force type apparatus for neutron reflection, based on a flexible membrane approach. *Review of Scientific Instruments* **2012,** *83* (11), 113903.

77. Klein, J., Shear, friction, and lubrication forces between polymer-bearing surfaces. *Annual Review of Materials Science* **1996,** *26* (1), 581-612.

78. Klein, J.; Kumacheva, E., Confinement-induced phase transitions in simple liquids. *Science* **1995,** *269* (5225), 816.

79. (a) Yamamoto, S.; Ejaz, M.; Tsujii, Y.; Matsumoto, M.; Fukuda, T., Surface interaction forces of well-defined, high-density polymer brushes studied by atomic force microscopy. 1. Effect of chain length. *Macromolecules* **2000,** *33* (15), 5602-5607; (b) Yamamoto, S.; Ejaz, M.; Tsujii, Y.; Fukuda, T., Surface interaction forces of well-defined, high-density polymer brushes studied by atomic force microscopy. 2. Effect of graft density. *Macromolecules* **2000,** *33* (15), 5608-5612; (c) Mulder, D. J.; Kuhl, T. L., Polymer brushes in restricted geometries. *Soft Matter* **2010,** *6* (21), 5401-5407.

80. (a) Milner, S. T.; Witten, T.; Cates, M., Theory of the grafted polymer brush. *Macromolecules* **1988,** *21* (8), 2610-2619; (b) Kent, M.; Lee, L.; Factor, B.; Rondelez, F.; Smith, G., Tethered chains in good solvent conditions: an experimental study involving Langmuir diblock copolymer monolayers. *The Journal of chemical physics* **1995,** *103* (6), 2320-2342; (c) Kent, M. S., A quantitative study of tethered chains in various solution conditions using Langmuir diblock copolymer monolayers. *Macromolecular Rapid Communications* **2000,** *21* (6), 243-270.

81. (a) Zhu, X.; Yan, C.; Winnik, F.; Leckband, D., End-grafted low-molecular-weight PNIPAM does not collapse above the LCST. *Langmuir* **2007,** *23* (1), 162-169; (b) Choi, B.-C.; Choi, S.; Leckband, D., Poly (N-isopropyl acrylamide) brush topography: dependence on grafting conditions and temperature. *Langmuir* **2013,** *29* (19), 5841-5850; (c) Malham, I. B.; Bureau,

L., Density effects on collapse, compression, and adhesion of thermoresponsive polymer brushes. *Langmuir* **2009,** *26* (7), 4762-4768.

82. (a) Klein, J.; Kamiyama, Y.; Yoshizawa, H.; Israelachvili, J. N.; Fredrickson, G. H.; Pincus, P.; Fetters, L. J., Lubrication forces between surfaces bearing polymer brushes. *Macromolecules* **1993,** *26* (21), 5552-5560; (b) Kuhl, T.; Leckband, D.; Lasic, D.; Israelachvili, J., Modulation of interaction forces between bilayers exposing short-chained ethylene oxide headgroups. *Biophysical Journal* **1994,** *66* (5), 1479-1488; (c) Leckband, D.; Sheth, S.; Halperin, A., Grafted poly (ethylene oxide) brushes as nonfouling surface coatings. *Journal of Biomaterials Science, Polymer Edition* **1999,** *10* (10), 1125-1147; (d) Maeda, N.; Chen, N.; Tirrell, M.; Israelachvili, J. N., Adhesion and friction mechanisms of polymer-on-polymer surfaces. *Science* **2002,** *297* (5580), 379-382.

83. (a) Kelley, T. W.; Schorr, P. A.; Johnson, K. D.; Tirrell, M.; Frisbie, C. D., Direct force measurements at polymer brush surfaces by atomic force microscopy. *Macromolecules* **1998,** *31* (13), 4297-4300; (b) Raftari, M.; Zhang, Z. J.; Carter, S. R.; Leggett, G. J.; Geoghegan, M., Nanoscale contact mechanics between two grafted polyelectrolyte surfaces. *Macromolecules* **2015,** *48* (17), 6272-6279.

84. (a) Balazs, A. C.; Singh, C.; Zhulina, E., Modeling the interactions between polymers and clay surfaces through self-consistent field theory. *Macromolecules* **1998,** *31* (23), 8370-8381; (b) Russano, D.; Carrillo, J.-M. Y.; Dobrynin, A. V., Interaction between brush layers of bottle-brush polyelectrolytes: Molecular dynamics simulations. *Langmuir* **2011,** *27* (17), 11044-11051; (c) Ou, Y.; Sokoloff, J. B.; Stevens, M. J., Comparison of the kinetic friction of planar neutral and polyelectrolyte polymer brushes using molecular dynamics simulations. *Physical Review E* **2012,** *85* (1), 011801.

85. Abbott, S. B.; de Vos, W. M.; Mears, L. L.; Skoda, M.; Dalgliesh, R.; Edmondson, S.; Richardson, R. M.; Prescott, S. W., Switching the interpenetration of confined asymmetric polymer brushes. *Macromolecules* **2016,** *49* (11), 4349-4357.

86. Cosgrove, T.; Luckham, P.; Richardson, R.; Webster, J.; Zarbakhsh, A., The measurement of volume fraction profiles for adsorbed polymers under compression using neutron reflectometry. *Colloids and Surfaces A: Physicochemical and Engineering Aspects* **1994,** *86*, 103-110.

87. (a) Karim, A.; Satija, S.; Douglas, J.; Ankner, J.; Fetters, L., Neutron reflectivity study of the density profile of a model end-grafted polymer brush: influence of solvent quality. *Physical review letters* **1994,** *73* (25), 3407; (b) Elliott, I. G.; Mulder, D. E.; Träskelin, P. T.; Ell, J. R.; Patten, T. E.; Kuhl, T. L.; Faller, R., Confined polymer systems: synergies between simulations and neutron scattering experiments. *Soft Matter* **2009,** *5* (23), 4612-4622.

88. Homola, J.; Yee, S. S.; Gauglitz, G., Surface plasmon resonance sensors: review. *Sensors and Actuators B: Chemical* **1999,** *54* (1), 3-15.

89. Sorrell, C. D.; Serpe, M. J., Reflection Order Selectivity of Color-Tunable Poly (N-isopropylacrylamide) Microgel Based Etalons. *Advanced Materials* **2011,** *23* (35), 4088-4092.

90. Wood, R., XLII. On a remarkable case of uneven distribution of light in a diffraction grating spectrum. *The London, Edinburgh, and Dublin Philosophical Magazine and Journal of Science* **1902,** *4* (21), 396-402.

91. Rayleigh, L., On the dynamical theory of gratings. *Proceedings of the Royal Society of London. Series A, Containing Papers of a Mathematical and Physical Character* **1907,** *79* (532), 399-416.

92. (a) Lee, H. J.; Nedelkov, D.; Corn, R. M., Surface plasmon resonance imaging measurements of antibody arrays for the multiplexed detection of low molecular weight protein biomarkers. *Analytical Chemistry* **2006,** *78* (18), 6504-6510; (b) Myszka, D. G.; Rich, R. L., Implementing surface plasmon resonance biosensors in drug discovery. *Pharmaceutical Science & Technology Today* **2000,** *3* (9), 310-317; (c) Wegner, G. J.; Lee, H. J.; Corn, R. M., Characterization and optimization of peptide arrays for the study of epitope-antibody interactions using surface plasmon resonance imaging. *Analytical Chemistry* **2002,** *74* (20), 5161-5168; (d) Homola, J., Surface plasmon resonance sensors for detection of chemical and biological species. *Chemical Reviews* **2008,** *108* (2), 462-493.

93. Schasfoort, R. B.; Tudos, A. J., *Handbook of surface plasmon resonance*. The Royal Societry of Chemistry: Cambridge, 2008.

94. Kabashin, A.; Evans, P.; Pastkovsky, S.; Hendren, W.; Wurtz, G.; Atkinson, R.; Pollard, R.; Podolskiy, V.; Zayats, A., Plasmonic nanorod metamaterials for biosensing. *Nature Materials* **2009,** *8* (11), 867-871.

95. Cao, C.; Sim, S. J., Signal enhancement of surface plasmon resonance immunoassay using enzyme precipitation-functionalized gold nanoparticles: A femto molar level measurement of anti-glutamic acid decarboxylase antibody. *Biosensors and Bioelectronics* **2007,** *22* (9), 1874-1880.

96. Wink, T.; van Zuilen, S. J.; Bult, A.; Van Bennekom, W. P., Liposome-mediated enhancement of the sensitivity in immunoassays of proteins and peptides in surface plasmon resonance spectrometry. *Analytical Chemistry* **1998,** *70* (5), 827-832.

97. Huang, H.; Ran, P.; Liu, Z., Signal enhancement of surface plasmon resonance-based immunoassays for the allergen detection. *Sensors and Actuators B: Chemical* **2008,** *131* (2), 417-423.

98. Liu, C.; Balsamo, V.; Sun, D.; Naja, M.; Wang, X.; Rosen, B.; Li, C.-Z., A 3D localized surface plasmon resonance biosensor for the study of trivalent arsenic binding to the ArsA ATPase. *Biosensors and Bioelectronics* **2012,** *38* (1), 19-26.

99. (a) Lee, J. E.; Chung, K.; Lee, J.; Shin, K.; Kim, D. H., In Situ Studies of Surface-Plasmon-Resonance-Coupling Sensor Mediated by Stimuli-Sensitive Polymer Linker. *Advanced Functional Materials* **2015,** *25* (43), 6716-6724; (b) Song, J.; Cheng, L.; Liu, A.; Yin, J.; Kuang, M.; Duan, H., Plasmonic vesicles of amphiphilic gold nanocrystals: self-assembly and external-stimuli-triggered destruction. *Journal of the American Chemical Society* **2011,** *133* (28), 10760-10763.

100. Kuckling, D.; Harmon, M. E.; Frank, C. W., Photo-cross-linkable PNIPAAm copolymers. 1. Synthesis and characterization of constrained temperature-responsive hydrogel layers. *Macromolecules* **2002,** *35* (16), 6377-6383.

101. De las Heras Alarcón, C.; Pennadam, S.; Alexander, C., Stimuli responsive polymers for biomedical applications. *Chemical Society Reviews* **2005,** *34* (3), 276-285.

102. (a) Islam, M. R.; Serpe, M. J., Polyelectrolyte mediated intra and intermolecular crosslinking in microgel-based etalons for sensing protein concentration in solution. *Chemical Communications* **2013,** *49* (26), 2646-2648; (b) Islam, M. R.; Serpe, M. J., Polymer-based devices for the label-free detection of DNA in solution: low DNA concentrations yield large signals. *Analytical and Bioanalytical Chemistry* **2014,** *406* (19), 4777-4783.

103. (a) Islam, M. R.; Serpe, M. J., Poly (N-isopropylacrylamide) microgel-based thin film actuators for humidity sensing. *RSC Advances* **2014,** *4* (60), 31937-31940; (b) Han, D.-M.; Zhang, Q. M.; Serpe, M. J., Poly (N-isopropylacrylamide)-co-(acrylic acid) microgel/Ag nanoparticle hybrids for the colorimetric sensing of H_2O_2. *Nanoscale* **2015,** *7* (6), 2784-2789.

104. Sorrell, C. D.; Carter, M. C.; Serpe, M. J., A "paint-on" protocol for the facile assembly of uniform microgel coatings for color tunable etalon fabrication. *ACS Applied Materials & Interfaces* **2011,** *3* (4), 1140-1147.

105. Mie, G., Beiträge zur Optik trüber Medien, speziell kolloidaler Metallösungen. *Annalen der Physik* **1908,** *330* (3), 377-445.

106. Harmon, M. E.; Kuckling, D.; Frank, C. W., Photo-cross-linkable PNIPAAm copolymers. 2. Effects of constraint on temperature and pH-responsive hydrogel layers. *Macromolecules* **2003,** *36* (1), 162-172.

107. (a) Norrman, S.; Andersson, T.; Petö, G.; Somogyi, S., Quantitative evolution studies of particle separation, size and shape for vapour-deposited ultrathin gold films on glass substrates. *Thin Solid Films* **1981,** *77* (4), 359-366; (b) Golan, Y.; Margulis, L.; Rubinstein, I., Vacuum-deposited gold films: I. Factors affecting the film morphology. *Surface Science* **1992,** *264* (3), 312-326.

108. Carter, M. C.; Sorrell, C. D.; Serpe, M. J., Deswelling kinetics of color tunable poly (N-isopropylacrylamide) microgel-based etalons. *The Journal of Physical Chemistry B* **2011,** *115* (49), 14359-14368.

109. Bernheimer, H.; Birkmayer, W.; Hornykiewicz, O.; Jellinger, K.; Seitelberger, F., Brain dopamine and the syndromes of Parkinson and Huntington Clinical, morphological and neurochemical correlations. *Journal of the Neurological Sciences* **1973,** *20* (4), 415-455.

110. Matsui, J.; Akamatsu, K.; Hara, N.; Miyoshi, D.; Nawafune, H.; Tamaki, K.; Sugimoto, N., SPR sensor chip for detection of small molecules using molecularly imprinted polymer with embedded gold nanoparticles. *Analytical Chemistry* **2005,** *77* (13), 4282-4285.

111. (a) Mabey, D.; Peeling, R. W.; Ustianowski, A.; Perkins, M. D., Tropical infectious diseases: diagnostics for the developing world. *Nature Reviews Microbiology* **2004,** *2* (3), 231-240; (b) Petersen, P. E., The World Oral Health Report 2003: continuous improvement of oral health in the 21st century–the approach of the WHO Global Oral Health Programme. *Community Dentistry and Oral Epidemiology* **2003,** *31* (s1), 3-24; (c) Yager, P.; Edwards, T.; Fu, E.; Helton, K.; Nelson, K.; Tam, M. R.; Weigl, B. H., Microfluidic diagnostic technologies for global public health. *Nature* **2006,** *442* (7101), 412-418.

112. (a) Gamborg, O. L.; Constabel, F.; Fowke, L.; Kao, K.; Ohyama, K.; Kartha, K.; Pelcher, L., Protoplast and cell culture methods in somatic hybridization in higher plants. *Canadian Journal of Genetics and Cytology* **1974,** *16* (4), 737-750; (b) Gazdar, A. F.; Oie, H. K., Cell culture methods for human lung cancer. *Cancer Genetics and Cytogenetics* **1986,** *19* (1), 5-10.

113. (a) Engvall, E.; Perlmann, P., Enzyme-linked immunosorbent assay (ELISA) quantitative assay of immunoglobulin G. *Immunochemistry* **1971,** *8* (9), 871-874; (b) Engvall, E.; Perlmann, P., Enzyme-linked immunosorbent assay, ELISA III. Quantitation of specific antibodies by enzyme-labeled anti-immunoglobulin in antigen-coated tubes. *The Journal of Immunology* **1972,** *109* (1), 129-135; (c) Hager, T.; Spahr, C.; Xu, J.; Salimi-Moosavi, H.; Hall, M., Differential enzyme-linked immunosorbent assay and ligand-binding mass spectrometry for analysis of biotransformation of protein therapeutics: application to various FGF21 modalities. *Analytical Chemistry* **2013,** *85* (5), 2731-2738.

114. (a) Kaplan, R. N.; Riba, R. D.; Zacharoulis, S.; Bramley, A. H.; Vincent, L.; Costa, C.; MacDonald, D. D.; Jin, D. K.; Shido, K.; Kerns, S. A., VEGFR1-positive haematopoietic bone marrow progenitors initiate the pre-metastatic niche. *Nature* **2005,** *438* (7069), 820-827; (b) Myers, F. B.; Lee, L. P., Innovations in optical microfluidic technologies for point-of-care diagnostics. *Lab on a Chip* **2008,** *8* (12), 2015-2031; (c) Peeling, R.; Mabey, D., Point-of-care tests for diagnosing infections in the developing world. *Clinical Microbiology and Infection* **2010,** *16* (8), 1062-1069.

115. Hu, J.; Wang, S.; Wang, L.; Li, F.; Pingguan-Murphy, B.; Lu, T. J.; Xu, F., Advances in paper-based point-of-care diagnostics. *Biosensors and Bioelectronics* **2014,** *54*, 585-597.

116. (a) Soper, S. A.; Brown, K.; Ellington, A.; Frazier, B.; Garcia-Manero, G.; Gau, V.; Gutman, S. I.; Hayes, D. F.; Korte, B.; Landers, J. L., Point-of-care biosensor systems for cancer diagnostics/prognostics. *Biosensors and Bioelectronics* **2006,** *21* (10), 1932-1942; (b) Malhotra, R.; Patel, V.; Vaqué, J. P.; Gutkind, J. S.; Rusling, J. F., Ultrasensitive electrochemical immunosensor for oral cancer biomarker IL-6 using carbon nanotube forest electrodes and multilabel amplification. *Analytical Chemistry* **2010,** *82* (8), 3118-3123; (c) Ge, L.; Yan, J.; Song, X.; Yan, M.; Ge, S.; Yu, J., Three-dimensional paper-based electrochemiluminescence immunodevice for multiplexed measurement of biomarkers and point-of-care testing. *Biomaterials* **2012,** *33* (4), 1024-1031.

117. (a) Sibbing, D.; Braun, S.; Morath, T.; Mehilli, J.; Vogt, W.; Schömig, A.; Kastrati, A.; von Beckerath, N., Platelet reactivity after clopidogrel treatment assessed with point-of-care analysis and early drug-eluting stent thrombosis. *Journal of the American College of Cardiology* **2009,** *53* (10), 849-856; (b) Tüdős, A. J.; Besselink, G. A.; Schasfoort, R. B., Trends in miniaturized total analysis systems for point-of-care testing in clinical chemistry. *Lab on a Chip* **2001,** *1* (2), 83-95.

118. (a) Shafiee, H.; Wang, S.; Inci, F.; Toy, M.; Henrich, T. J.; Kuritzkes, D. R.; Demirci, U., Emerging technologies for point-of-care management of HIV infection. *Annual Review of Medicine* **2015,** *66*, 387-405; (b) McNerney, R.; Daley, P., Towards a point-of-care test for active tuberculosis: obstacles and opportunities. *Nature Reviews Microbiology* **2011,** *9* (3), 204-213.

119. Zhu, H.; Isikman, S. O.; Mudanyali, O.; Greenbaum, A.; Ozcan, A., Optical imaging techniques for point-of-care diagnostics. *Lab on a Chip* **2013,** *13* (1), 51-67.

120. Rindorf, L.; Jensen, J. B.; Dufva, M.; Pedersen, L. H.; Bang, O., Photonic crystal fiber long-period gratings for biochemical sensing. *Optics Express* **2006,** *14* (18), 8224-8231.

121. Gao, Y.; Gan, Q.; Xin, Z.; Cheng, X.; Bartoli, F. J., Plasmonic Mach–Zehnder interferometer for ultrasensitive on-chip biosensing. *ACS nano* **2011,** *5* (12), 9836-9844.

122. Yanik, A. A.; Cetin, A. E.; Huang, M.; Artar, A.; Mousavi, S. H.; Khanikaev, A.; Connor, J. H.; Shvets, G.; Altug, H., Seeing protein monolayers with naked eye through plasmonic Fano resonances. *Proceedings of the National Academy of Sciences* **2011,** *108* (29), 11784-11789.

123. Huang, L.; Reekmans, G.; Saerens, D.; Friedt, J.-M.; Frederix, F.; Francis, L.; Muyldermans, S.; Campitelli, A.; Van Hoof, C., Prostate-specific antigen immunosensing based on mixed self-assembled monolayers, camel antibodies and colloidal gold enhanced sandwich assays. *Biosensors and bioelectronics* **2005,** *21* (3), 483-490.

124. (a) Yan, X.; Wang, F.; Zheng, B.; Huang, F., Stimuli-responsive supramolecular polymeric materials. *Chemical Society Reviews* **2012,** *41* (18), 6042-6065; (b) Roy, D.; Cambre, J. N.; Sumerlin, B. S., Future perspectives and recent advances in stimuli-responsive materials. *Progress in Polymer Science* **2010,** *35* (1), 278-301.

125. (a) Serpe, M. J.; Lyon, L. A., Optical and acoustic studies of pH-dependent swelling in microgel thin films. *Chemistry of Materials* **2004,** *16* (22), 4373-4380; (b) Kim, J.; Serpe, M. J.; Lyon, L. A., Hydrogel microparticles as dynamically tunable microlenses. *Journal of the American Chemical Society* **2004,** *126* (31), 9512-9513.

126. Lloyd, D. R.; Burns, C. M., Coupling of acrylic polymers and collagen by use of a water-soluble carbodiimide. I. Optimization of reaction conditions. *Journal of Polymer Science: Polymer Chemistry Edition* **1979,** *17* (11), 3459-3472.

127. (a) Collaboration, E. R. F., Diabetes mellitus, fasting blood glucose concentration, and risk of vascular disease: a collaborative meta-analysis of 102 prospective studies. *The Lancet* **2010,** *375* (9733), 2215-2222; (b) Balkau, B.; Shipley, M.; Jarrett, R. J.; Pyörälä, K.; Pyörälä, M.; Forhan, A.; Eschwège, E., High blood glucose concentration is a risk factor for mortality in middle-aged nondiabetic men: 20-year follow-up in the Whitehall Study, the Paris Prospective Study, and the Helsinki Policemen Study. *Diabetes care* **1998,** *21* (3), 360-367; (c) Egi, M.; Bellomo, R.; Stachowski, E.; French, C. J.; Hart, G., Variability of blood glucose concentration and short-term mortality in critically ill patients. *The Journal of the American Society of Anesthesiologists* **2006,** *105* (2), 244-252.

128. Miyata, T.; Jikihara, A.; Nakamae, K.; Hoffman, A. S., Preparation of poly (2-glucosyloxyethyl methacrylate)-concanavalin A complex hydrogel and its glucose-sensitivity. *Macromolecular Chemistry and Physics* **1996,** *197* (3), 1135-1146.

129. bin Mat Yunus, W. M.; bin Abdul Rahman, A., Refractive index of solutions at high concentrations. *Applied Optics* **1988,** *27* (16), 3341-3343.

130. Tumolo, T.; Angnes, L.; Baptista, M. S., Determination of the refractive index increment (dn/dc) of molecule and macromolecule solutions by surface plasmon resonance. *Analytical Biochemistry* **2004,** *333* (2), 273-279.

131. Reufer, M.; D az-Leyva, P.; Lynch, I.; Scheffold, F., Temperature-sensitive poly (N-Isopropyl-Acrylamide) microgel particles: A light scattering study. *The European Physical Journal E* **2009,** *28* (2), 165-171.

132. Valenga, F.; Petri, D. F.; Lucyszyn, N.; Jó, T. A.; Sierakowski, M. R., Galactomannan thin films as supports for the immobilization of Concanavalin A and/or dengue viruses. *International Journal of Biological Macromolecules* **2012**, *50* (1), 88-94.

133. (a) Kamata, K.; Lu, Y.; Xia, Y., Synthesis and characterization of monodispersed core-shell spherical colloids with movable cores. *Journal of the American Chemical Society* **2003**, *125* (9), 2384-2385; (b) Weissman, J. M.; Sunkara, H. B.; Tse, A. S.; Asher, S. A. Thermally switchable periodicities and diffraction from novel mesoscopically ordered materials. *Science* **1996**, 274 (5289), 959-960.

134. Wang, Y.; Mirkin, C. A.; Park, S.-J., Nanofabrication beyond electronics. *ACS Nano* **2009,** *3* (5), 1049-1056.

135. Morandi, V.; Marabelli, F.; Amendola, V.; Meneghetti, M.; Comoretto, D., Colloidal photonic crystals doped with gold nanoparticles: spectroscopy and optical switching properties. *Advanced Functional Materials* **2007,** *17* (15), 2779-2786.

136. Gittins, D. I.; Bethell, D.; Schiffrin, D. J.; Nichols, R. J., A nanometre-scale electronic switch consisting of a metal cluster and redox-addressable groups. *Nature* **2000,** *408* (6808), 67.

137. Corma, A.; Garcia, H., Supported gold nanoparticles as catalysts for organic reactions. *Chemical Society Reviews* **2008,** *37* (9), 2096-2126.

138. Müller, M. B.; uttner , C.; ni g, T. A.; Tsukruk, V. V.; F r ster, S.; Karg, M.; Fery, A., Plasmonic library based on substrate-supported gradiential plasmonic arrays. *ACS Nano* **2014,** *8* (9), 9410-9421.

139. (a) Lyvers, D. P.; Moon, J.-M.; Kildishev, A. V.; Shalaev, V. M.; Wei, A., Gold nanorod arrays as plasmonic cavity resonators. *ACS Nano* **2008,** *2* (12), 2569-2576; (b) Kan, T.; Matsumoto, K.; Shimoyama, I. In *Nano-pillar structure for sensitivity enhancement of SPR sensor*, Solid-State Sensors, Actuators and Microsystems Conference, 2009. TRANSDUCERS 2009. International, 21-25 2009; pp 1481-1484.

140. (a) Choi, D.; Choi, Y.; Hong, S.; Kang, T.; Lee, L. P., Self-organized hexagonal-nanopore SERS array. *Small* **2010,** *6* (16), 1741-1744; (b) Kwak, E.-S.; Henzie, J.; Chang, S.-H.; Gray, S. K.; Schatz, G. C.; Odom, T. W., Surface plasmon standing waves in large-area subwavelength hole arrays. *Nano Letters* **2005,** *5* (10), 1963-1967.

141. (a) Li, M.; Cushing, S. K.; Liang, H.; Suri, S.; Ma, D.; Wu, N., Plasmonic nanorice antenna on triangle nanoarray for surface-enhanced Raman scattering detection of hepatitis B virus DNA. *Analytical Chemistry* **2013,** *85* (4), 2072-2078; (b) Chen, A.; DePrince, A. E.; Demortière, A.; JoshiImre, A.; Shevchenko, E. V.; Gray, S. K.; Welp, U.; Vlasko-Vlasov, V. K., Self-Assembled Large Au Nanoparticle Arrays with Regular Hot Spots for SERS. *Small* **2011,** *7* (16), 2365-2371; (c) Le, F.; Brandl, D. W.; Urzhumov, Y. A.; Wang, H.; Kundu, J.; Halas, N. J.; Aizpurua, J.; Nordlander, P., Metallic nanoparticle arrays: a common substrate for both surface-enhanced Raman scattering and surface-enhanced infrared absorption. *ACS Nano* **2008,** *2* (4), 707-718.

142. Murray-Méthot, M.-P.; Ratel, M.; Masson, J.-F., Optical properties of Au, Ag, and bimetallic Au on Ag nanohole arrays. *The Journal of Physical Chemistry C* **2010,** *114* (18), 8268-8275.

143. Wang, D.; Yang, A.; Hryn, A. J.; Schatz, G. C.; Odom, T. W., Superlattice plasmons in hierarchical Au nanoparticle arrays. *ACS Photonics* **2015,** *2* (12), 1789-1794.

144. Saboktakin, M.; Ye, X.; Chettiar, U. K.; Engheta, N.; Murray, C. B.; Kagan, C. R., Plasmonic enhancement of nanophosphor upconversion luminescence in Au nanohole arrays. *ACS Nano* **2013,** *7* (8), 7186-7192.

145. Ebbesen, T. W.; Lezec, H. J.; Ghaemi, H.; Thio, T.; Wolff, P., Extraordinary optical transmission through sub-wavelength hole arrays. *Nature* **1998,** *391* (6668), 667.

146. Iovan, A.; Fischer, M.; Conte, R. L.; Korenivski, V., Sub-10 nm colloidal lithography for circuit-integrated spin-photo-electronic devices. *Beilstein Journal of Nanotechnology* **2012,** *3*, 884.

147. Lendlein, A.; Shastri, V. P., Stimuli-Sensitive Polymers. *Advanced Materials* **2010,** *22* (31), 3344-3347.

148. Yuk, S. H.; Cho, S. H.; Lee, S. H., pH/temperature-responsive polymer composed of poly ((N, N-dimethylamino) ethyl methacrylate-co-ethylacrylamide). *Macromolecules* **1997,** *30* (22), 6856-6859.

149. Dai, S.; Ravi, P.; Tam, K. C., pH-Responsive polymers: synthesis, properties and applications. *Soft Matter* **2008,** *4* (3), 435-449.

150. Zhao, Y.; Ikeda, T., *Smart light-responsive materials: azobenzene-containing polymers and liquid crystals*. John Wiley & Sons: 2009.

151. Hu, J.; Liu, S., Responsive polymers for detection and sensing applications: current status and future developments. *Macromolecules* **2010,** *43* (20), 8315-8330.

152. Wu, C.; Wang, X., Globule-to-coil transition of a single homopolymer chain in solution. *Physical Review Letters* **1998,** *80* (18), 4092.

153. Turkevich, J.; Garton, G.; Stevenson, P., The color of colloidal gold. *Journal of Colloid Science* **1954,** *9*, 26-35.

154. (a) Volk, K.; Fitzgerald, J. P.; Retsch, M.; Karg, M., Time-Controlled Colloidal Superstructures: Long-Range Plasmon Resonance Coupling in Particle Monolayers. *Advanced Materials* **2015,** *27* (45), 7332-7337; (b) Rauh, A.; Honold, T.; Karg, M., Seeded precipitation polymerization for the synthesis of gold-hydrogel core-shell particles: the role of surface functionalization and seed concentration. *Colloid and Polymer Science* **2016,** *294* (1), 37-47.

155. Honold, T.; Volk, K.; Rauh, A.; Fitzgerald, J.; Karg, M., Tunable plasmonic surfaces via colloid assembly. *Journal of Materials Chemistry C* **2015,** *3* (43), 11449-11457.

156. Sau, T. K.; Murphy, C. J., Room temperature, high-yield synthesis of multiple shapes of gold nanoparticles in aqueous solution. *Journal of the American Chemical Society* **2004,** *126* (28), 8648-8649.

157. Huang, H.-C.; Rege, K.; Heys, J. J., Spatiotemporal temperature distribution and cancer cell death in response to extracellular hyperthermia induced by gold nanorods. *ACS Nano* **2010,** *4* (5), 2892-2900.

158. Xia, Y., Nanomaterials at work in biomedical research. *Nature Materials* **2008,** *7* (10), 758-760.

159. Jain, P. K.; Lee, K. S.; El-Sayed, I. H.; El-Sayed, M. A., Calculated absorption and scattering properties of gold nanoparticles of different size, shape, and composition: applications in biological imaging and biomedicine. *The Journal of Physical Chemistry B* **2006,** *110* (14), 7238-7248.

160. Saha, K.; Agasti, S. S.; Kim, C.; Li, X.; Rotello, V. M., Gold nanoparticles in chemical and biological sensing. *Chemical Reviews* **2012,** *112* (5), 2739-2779.

161. Ghosh, P. S.; Kim, C.-K.; Han, G.; Forbes, N. S.; Rotello, V. M., Efficient gene delivery vectors by tuning the surface charge density of amino acid-functionalized gold nanoparticles. *ACS Nano* **2008,** *2* (11), 2213-2218.

162. Brown, S. D.; Nativo, P.; Smith, J.-A.; Stirling, D.; Edwards, P. R.; Venugopal, B.; Flint, D. J.; Plumb, J. A.; Graham, D.; Wheate, N. J., Gold nanoparticles for the improved anticancer drug delivery of the active component of oxaliplatin. *Journal of the American Chemical Society* **2010,** *132* (13), 4678-4684.

163. Nagesha, D.; Laevsky, G.; Lampton, P.; Banyal, R.; Warner, C.; DiMarzio, C.; Sridhar, S., In vitro imaging of embryonic stem cells using multiphoton luminescence of gold nanoparticles. *International Journal of Nanomedicine* **2007,** *2* (4), 813.

164. Boisselier, E.; Astruc, D., Gold nanoparticles in nanomedicine: preparations, imaging, diagnostics, therapies and toxicity. *Chemical Society Reviews* **2009,** *38* (6), 1759-1782.

165. Terentyuk, G. S.; Maslyakova, G. N.; Suleymanova, L. V.; Khlebtsov, N. G.; Khlebtsov, B. N.; Akchurin, G. G.; Maksimova, I. L.; Tuchin, V. V., Laser-induced tissue hyperthermia mediated by gold nanoparticles: toward cancer phototherapy. *Journal of Biomedical Optics* **2009,** *14* (2), 021016-021016-9.

166. Heskins, M.; Guillet, J. E., Solution properties of poly (N-isopropylacrylamide). *Journal of Macromolecular Science—Chemistry* **1968,** *2* (8), 1441-1455.

167. Lynn, D. M.; Amiji, M. M.; Langer, R., pH-responsive polymer microspheres: Rapid release of encapsulated material within the range of intracellular pH. *Angewandte Chemie International Edition* **2001,** *40* (9), 1707-1710.

168. Zhao, B.; Moore, J. S., Fast pH-and ionic strength-responsive hydrogels in microchannels. *Langmuir* **2001,** *17* (16), 4758-4763.

169. (a) Stayton, P. S.; Shimoboji, T.; Long, C.; Chilkoti, A.; Ghen, G.; Harris, J. M.; Hoffman, A. S., Control of protein–ligand recognition using a stimuli-responsive polymer. **1995**; (b) Islam, M. R.; Serpe, M. J., A novel label-free colorimetric assay for DNA concentration in solution. *Analytica Chimica Acta* **2014,** *843*, 83-88.

170. Hribar, K. C.; Lee, M. H.; Lee, D.; Burdick, J. A., Enhanced Release of Small Molecules from Near-Infrared Light Responsive Polymer− Nanorod Composites. *ACS Nano* **2011,** *5* (4), 2948-2956.

171. (a) Kubota, K.; Fujishige, S.; Ando, I., Solution properties of poly (N-isopropylacrylamide) in water. *Polymer Journal* **1990,** *22* (1), 15-20; (b) Pelton, R.; Pelton, H.; Morphesis, A.;

Rowell, R., Particle sizes and electrophoretic mobilities of poly (N-isopropylacrylamide) latex. *Langmuir* **1989,** *5* (3), 816-818.

172. (a) Wu, C.; Zhou, S., Volume phase transition of swollen gels: discontinuous or continuous? *Macromolecules* **1997,** *30* (3), 574-576; (b) Kratz, K.; Hellweg, T.; Eimer, W., Structural changes in PNIPAM microgel particles as seen by SANS, DLS, and EM techniques. *Polymer* **2001,** *42* (15), 6631-6639; (c) Wu, C.; Zhou, S., Laser light scattering study of the phase transition of poly (N-isopropylacrylamide) in water. 1. Single chain. *Macromolecules* **1995,** *28* (24), 8381-8387.

173. (a) Sagar, V.; Atluri, V.; Tomitaka, A.; Shah, P.; Nagasetti, A.; Pilakka-Kanthikeel, S.; El-Hage, N.; McGoron, A.; Takemura, Y.; Nair, M., Coupling of transient near infrared photonic with magnetic nanoparticle for potential dissipation-free biomedical application in brain. *Scientific Reports* **2016,** *6*; (b) Levskaya, A.; Weiner, O. D.; Lim, W. A.; Voigt, C. A., Spatiotemporal control of cell signalling using a light-switchable protein interaction. *Nature* **2009,** *461* (7266), 997-1001; (c) Gorostiza, P.; Isacoff, E. Y., Optical switches for remote and noninvasive control of cell signaling. *Science* **2008,** *322* (5900), 395-399.

174. Eisenbach, C. D., Isomerization of aromatic azo chromophores in poly (ethyl acrylate) networks and photomechanical effect. *Polymer* **1980,** *21* (10), 1175-1179.

175. Yun, C.; You, J.; Kim, J.; Huh, J.; Kim, E., Photochromic fluorescence switching from diarylethenes and its applications. *Journal of Photochemistry and Photobiology C: Photochemistry Reviews* **2009,** *10* (3), 111-129.

176. Gao, Y.; Zago, G. P.; Jia, Z.; Serpe, M. J., Controlled and triggered small molecule release from a confined polymer film. *ACS Applied Materials & Interfaces* **2013,** *5* (19), 9803-9808.

177. (a) Johnson, K. C.; Mendez, F.; Serpe, M. J., Detecting solution pH changes using poly (N-isopropylacrylamide)-co-acrylic acid microgel-based etalon modified quartz crystal microbalances. *Analytica Chimica Acta* **2012,** *739*, 83-88; (b) Islam, M. R.; Johnson, K. C.; Serpe, M. J., Microgel-based etalon coated quartz crystal microbalances for detecting solution pH: The effect of Au overlayer thickness. *Analytica Chimica Acta* **2013,** *792*, 110-114.

178. Sorrell, C. D.; Serpe, M. J., Glucose sensitive poly (N-isopropylacrylamide) microgel based etalons. *Analytical and Bioanalytical Chemistry* **2012,** *402* (7), 2385-2393.

179. Islam, M. R.; Irvine, J.; Serpe, M. J., Photothermally Induced Optical Property Changes of Poly (N-isopropylacrylamide) Microgel-Based Etalons. *ACS Applied Materials & Interfaces* **2015,** *7* (43), 24370-24376.

180. Yablonovitch, E., Inhibited spontaneous emission in solid-state physics and electronics. *Physical Review Letters* **1987,** *58* (20), 2059.

181. John, S., Strong localization of photons in certain disordered dielectric superlattices. *Physical Review Letters* **1987,** *58* (23), 2486.

182. (a) Knight, J. C., Photonic crystal fibres. *Nature* **2003,** *424* (6950), 847-851; (b) Russell, P., Photonic crystal fibers. *Science* **2003,** *299* (5605), 358-362.

183. O'Neill, M.; Kelly, S. M., Liquid crystals for charge transport, luminescence, and photonics. *Advanced Materials* **2003,** *15* (14), 1135-1146.

184. Arsenault, A. C.; Puzzo, D. P.; Manners, I.; Ozin, G. A., Photonic-crystal full-colour displays. *Nature Photonics* **2007,** *1* (8), 468-472.

185. (a) Lee, K.; Asher, S. A., Photonic crystal chemical sensors: pH and ionic strength. *Journal of the American Chemical Society* **2000,** *122* (39), 9534-9537; (b) Debord, J. D.; Lyon, L. A., Thermoresponsive photonic crystals. *The Journal of Physical Chemistry B* **2000,** *104* (27), 6327-6331.

186. (a) Campbell, M.; Sharp, D.; Harrison, M.; Denning, R.; Turberfield, A., Fabrication of photonic crystals for the visible spectrum by holographic lithography. *Nature* **2000,** *404* (6773), 53-56; (b) Edrington, A. C.; Urbas, A. M.; DeRege, P.; Chen, C. X.; Swager, T. M.; Hadjichristidis, N.; Xenidou, M.; Fetters, L. J.; Joannopoulos, J. D.; Fink, Y., Polymer-based photonic crystals. *Advanced Materials* **2001,** *13* (6), 421-425; (c) Xu, X.; Asher, S. A., Synthesis and utilization of monodisperse hollow polymeric particles in photonic crystals. *Journal of the American Chemical Society* **2004,** *126* (25), 7940-7945.

187. (a) Li, J.; Zhang, Z.; Xu, S.; Chen, L.; Zhou, N.; Xiong, H.; Peng, H., Label-free colorimetric detection of trace cholesterol based on molecularly imprinted photonic hydrogels. *Journal of Materials Chemistry* **2011,** *21* (48), 19267-19274; (b) Kelly, J. A.; Shukaliak, A. M.; Cheung, C. C.; Shopsowitz, K. E.; Hamad, W. Y.; MacLachlan, M. J., Responsive photonic hydrogels based on nanocrystalline cellulose. *Angewandte Chemie International Edition* **2013,** *52* (34), 8912-8916; (c) Tian, E.; Wang, J.; Zheng, Y.; Song, Y.; Jiang, L.; Zhu, D., Colorful humidity sensitive photonic crystal hydrogel. *Journal of Materials Chemistry* **2008,** *18* (10), 1116-1122; (d) Goponenko, A. V.; Asher, S. A., Modeling of stimulated hydrogel volume changes in photonic crystal Pb^{2+} sensing materials. *Journal of the American Chemical Society* **2005,** *127* (30), 10753-10759.

188. Xu, X.; Goponenko, A. V.; Asher, S. A., Polymerized polyHEMA photonic crystals: pH and ethanol sensor materials. *Journal of the American Chemical Society* **2008,** *130* (10), 3113-3119.

189. Ge, J.; He, L.; Goebl, J.; Yin, Y., Assembly of magnetically tunable photonic crystals in nonpolar solvents. *Journal of the American Chemical Society* **2009,** *131* (10), 3484-3486.

190. Ge, J.; Yin, Y., Responsive photonic crystals. *Angewandte Chemie International Edition* **2011,** *50* (7), 1492-1522.

191. Ge, J.; Yin, Y., Magnetically responsive colloidal photonic crystals. *Journal of Materials Chemistry* **2008,** *18* (42), 5041-5045.

192. (a) Sorrell, C. D.; Carter, M. C.; Serpe, M. J., Color Tunable Poly (N-Isopropylacrylamide)-co-Acrylic Acid Microgel–Au Hybrid Assemblies. *Advanced Functional Materials* **2011,** *21* (3), 425-433; (b) Islam, M. R.; Serpe, M. J., Penetration of polyelectrolytes into charged poly (N-isopropylacrylamide) microgel layers confined between two surfaces. *Macromolecules* **2013,** *46* (4), 1599-1606; (c) Hu, L.; Serpe, M. J., Color modulation of spatially isolated regions on a single poly (N-isopropylacrylamide) microgel based etalon. *Journal of Materials Chemistry* **2012,** *22* (17), 8199-8202; (d) Gao, Y.; Xu, W.; Serpe, M. J., Free-standing poly (N-isopropylacrylamide) microgel-based etalons. *Journal of Materials Chemistry C* **2014,** *2* (29), 5878-5884; (e) Gao, Y.; Serpe, M. J., Light-Induced Color Changes of Microgel-Based Etalons. *ACS Applied Materials & Interfaces* **2014**.

193. Zeltner, M.; Schätz, A.; Hefti, M. L.; Stark, W. J., Magnetothermally responsive C/Co@ PNIPAM-nanoparticles enable preparation of self-separating phase-switching palladium catalysts. *Journal of Materials Chemistry* **2011,** *21* (9), 2991-2996.

194. (a) Kawano, T.; Niidome, Y.; Mori, T.; Katayama, Y.; Niidome, T., PNIPAM gel-coated gold nanorods for targeted delivery responding to a near-infrared laser. *Bioconjugate Chemistry* **2009,** *20* (2), 209-212; (b) Senaratne, W.; Andruzzi, L.; Ober, C. K., Self-assembled monolayers and polymer brushes in biotechnology: current applications and future perspectives. *Biomacromolecules* **2005,** *6* (5), 2427-2448.

195. Islam, M. R.; Li, X.; Smyth, K.; Serpe, M. J., Polymer-Based Muscle Expansion and Contraction. *Angewandte Chemie International Edition* **2013,** *52* (39), 10330-10333.

196. Ohya, S.; Nakayama, Y.; Matsuda, T., Thermoresponsive artificial extracellular matrix for tissue engineering: hyaluronic acid bioconjugated with poly (N-isopropylacrylamide) grafts. *Biomacromolecules* **2001,** *2* (3), 856-863.

197. (a) Debord, J. D.; Lyon, L. A., Synthesis and characterization of pH-responsive copolymer microgels with tunable volume phase transition temperatures. *Langmuir* **2003,** *19* (18), 7662-7664; (b) Pelton, R.; Chibante, P., Preparation of aqueous latices with N-isopropylacrylamide. *Colloids and Surfaces* **1986,** *20* (3), 247-256.

198. Zhao, B.; Brittain, W. J., Polymer brushes: surface-immobilized macromolecules. *Progress in Polymer Science* **2000,** *25* (5), 677-710.

199. (a) Edmondson, S.; Osborne, V. L.; Huck, W. T., Polymer brushes via surface-initiated polymerizations. *Chemical Society Reviews* **2004,** *33* (1), 14-22; (b) Yang, X.; Shen, B.; Jiang, Y.; Zhao, Z.; Wang, C.; Ma, C.; Yang, B.; Lin, Q., A novel fluorescent polymer brushes film as a device for ultrasensitive detection of TNT. *Journal of Materials Chemistry A* **2013,** *1* (4), 1201-1206.

200. (a) Milner, S., Polymer brushes. *Science* **1991,** *251* (4996), 905-914; (b) Guzonas, D.; Boils, D.; Hair, M. L., Surface force measurements of polystyrene-block-poly (ethylene oxide) adsorbed from a nonselective solvent on mica. *Macromolecules* **1991,** *24* (11), 3383-3387; (c) Field, J.; Toprakcioglu, C.; Ball, R.; Stanley, H.; Dai, L.; Barford, W.; Penfold, J.; Smith, G.; Hamilton, W., Determination of end-adsorbed polymer density profiles by neutron reflectometry. *Macromolecules* **1992,** *25* (1), 434-439.

201. Cheng, G.; Böker, A.; Zhang, M.; Krausch, G.; Müller, A. H., Amphiphilic cylindrical core-shell brushes via a "grafting from" process using ATRP. *Macromolecules* **2001,** *34* (20), 6883-6888.

202. (a) Lee, S. H.; Dreyer, D. R.; An, J.; Velamakanni, A.; Piner, R. D.; Park, S.; Zhu, Y.; Kim, S. O.; Bielawski, C. W.; Ruoff, R. S., Polymer Brushes via Controlled, Surface-Initiated Atom Transfer Radical Polymerization (ATRP) from Graphene Oxide. *Macromolecular Rapid Communications* **2010,** *31* (3), 281-288; (b) Pyun, J.; Kowalewski, T.; Matyjaszewski, K., Synthesis of polymer brushes using atom transfer radical polymerization. *Macromolecular Rapid Communications* **2003,** *24* (18), 1043-1059.

203. Husseman, M.; Malmström, E. E.; McNamara, M.; Mate, M.; Mecerreyes, D.; Benoit, D. G.; Hedrick, J. L.; Mansky, P.; Huang, E.; Russell, T. P., Controlled synthesis of polymer brushes by "living" free radical polymerization techniques. *Macromolecules* **1999,** *32* (5), 1424-1431.

204. Shah, R. R.; Merreceyes, D.; Husemann, M.; Rees, I.; Abbott, N. L.; Hawker, C. J.; Hedrick, J. L., Using atom transfer radical polymerization to amplify monolayers of initiators patterned by microcontact printing into polymer brushes for pattern transfer. *Macromolecules* **2000,** *33* (2), 597-605.

List of Publications

1. **Wei, M.**, Serpe, M.J., "Microgel assisted self-assembly of Au nanoparticles for lithographic applications", *In Prep.*

2. **Wei, M.**, Serpe, M.J., "Au@pNIPAm core-shell microgel based optical device", *In Prep.*

3. **Wei, M.**, Li, X., Serpe, M.J., "Stimuli-responsive microgel-based SPR transducer for glucose detection using a competitive assay with Concanavalin A", *In Prep.*

4. **Wei, M.**, Xu. W., Gao, Y., Serpe, M.J., "Polymer film/Au assembly enhanced surface plasmon resonance for sensing", *In Prep.*

5. Carvalho, W.S.P.,**Wei, M.**, Ikpo, N., Gao, Y., Serpe, M. J., "Polymer-based technologies for sensing applications", *Anal. Chem.*, **2018,** 90 (1), 459-419.

6. Zhang, W., **Wei, M.**, Carvalho, W.S.P., Serpe, M.J., "Enzyme-assisted polymer film degradation-enabled biomolecule sensing with poly (N-isopropylacrylamide)-based optical devices", *Anal. Chim. Acta*, **2018**, 999, 139-143.

7. Xu, W., **Wei, M.**, Serpe, M.J., "Janus microgel with tunable functionality, polarity, and optical properties", *Adv. Opt. Mater.*, **2017**, 1600614.

8. Gao, Y., **Wei, M.**, Li, X., Xu, W., Ahiabu, A., Perdiz, J., Liu, Z., Serpe, M.J., "Stimuli-responsive polymers: Fundamental considerations and applications", *Macromol. Res.*, **2017**, 25 (6), 513-527.

9. **Wei, M.**, Gao, Y., Li, X., Serpe, M. J., "Stimuli-responsive polymers and their applications", *Polym. Chem.*, **2017**, 8 (1), 127-143.

10. Guo, S., Gao, Y., **Wei, M.**, Zhang, Q.M., Serpe, M.J., "Controlled release kinetics from a surface modified microgel-based Reservoir Device", *J. Mater. Chem. B*, **2015**, 3 (12), 2516-2521.

11. **Wei, M.**, Gao, Y., Serpe, M.J., "Polymer brush-based optical device with multiple responsivities", *J. Mater. Chem. B.*, **2015**, 3(5), 744-747.

12. Zhang, Q.M., Islam, M.R., Li, X., Xu, W., Gao, Y., **Wei, M**.; Ahiabu, A., Hyson, K., Serpe, M.J., "Structured materials for sensing applications", *Encyclopedia of Analytical Chemistry*, **2015**,1-17.

13. Islam, M. R., Gao, Y., Li, X., Zhang, Q.M., **Wei, M.**, Serpe, M.J., "Stimuli responsive polymeric materials for human health applications" *Chin. Sci. Bull.*, **2014**, 59(32), 4237-4255.

14. Zhang, Q.M., Li, X., Islam, M.R., **Wei, M**., Serpe, M.J., "Light switchable optical materials from azobenzene crosslinked poly(N-isopropylacrylamide)-based microgels", *J. Mater. Chem. C*, **2014**, 2 (34), 6961-6965.